

Study of Interactions between Atoms and Coherent Light in Magnetic Field

**A Thesis Submitted
To
Sikkim University**



**In Partial Fulfillment of the Requirement for the
Degree of Doctor of Philosophy in Physics**

**By
Indra Hang Subba
Department of Physics
School of Physical Sciences
Sikkim University**

May 2023

**To
My Beloved Parents**

6 माइल, सामदुर, तादोंग - 737102
गंगटोक, सिक्किम, भारत
फोन-03592-251212, 251415, 251656
टेलीफैक्स - 251067
वेबसाइट - www.cus.ac.in



6th Mile, Samdur, Tadong-737102
Gangtok, Sikkim, India
Ph. 03592-251212, 251415, 251656
Telefax : 251067
Website : www.cus.ac.in

सिक्किम विश्वविद्यालय SIKKIM UNIVERSITY

(भारत के संसद के अधिनियम द्वारा वर्ष 2007 में स्थापित और नैक (एनएएसी) द्वारा वर्ष 2015 में प्रत्यायित केंद्रीय विश्वविद्यालय)
(A central university established by an Act of Parliament of India in 2007 and accredited by NAAC in 2015)

Certificate

This is to certify that the Ph.D. thesis entitled "**Study of interaction between atoms and coherent light in magnetic field**" submitted to **Sikkim University** in partial fulfillment of the requirement for the degree of **Doctor of Philosophy in Physics**, embodies the result of *bona fide* research work carried out by **Mr. Indra Hang Subba** under my guidance and supervision. No part of the thesis has been submitted for diploma, associate-ship, fellowship or any other degree.

All the assistance and help received during the course of the investigation have been duly acknowledged by him.

(Dr. Ajay Tripathi)
Ph. D Supervisor
Department of Physics
School of Physical Sciences
Sikkim University

Associate Professor
Department of Physics
Sikkim University

Place: Gangtok, Sikkim

Date: 24/11/22

6 माइल, सामदुर, तादोंग - 737102
गंगटोक, सिक्किम, भारत
फोन-03592-251212, 251415, 251656
टेलीफैक्स - 251067
वेबसाइट - www.cus.ac.in



सिक्किम विश्वविद्यालय SIKKIM UNIVERSITY

6th Mile, Samdur, Tadong-737102
Gangtok, Sikkim, India
Ph. 03592-251212, 251415, 251656
Telefax : 251067
Website : www.cus.ac.in

(भारत के संसद के अधिनियम द्वारा वर्ष 2007 में स्थापित और नैक (एनएएसी) द्वारा वर्ष 2015 में प्रत्यापित केंद्रीय विश्वविद्यालय)
(A central university established by an Act of Parliament of India in 2007 and accredited by NAAC in 2015)

Certificate

This is to certify that the Ph.D. thesis entitled "**Study of interaction between atoms and coherent light in magnetic field**" submitted to **Sikkim University** in partial fulfillment of the requirement for the degree of **Doctor of Philosophy in Physics**, embodies the work carried out by **Mr. Indra Hang Subba** for the award of Ph.D. Degree in Physics, Sikkim University, Gangtok, Sikkim. The results are original and have not been submitted anywhere else for any other degree or diploma.

It is recommended this Ph.D. thesis to be placed before the Examiners for evaluation.

Head of the Department
(Dr. Ajay Tripathi)
Associate Professor
Department of Physics
School of Physical Sciences
Sikkim University
Gangtok - 737102

Place: Gangtok, Sikkim

Date: 24/11/22

6 माइल, साम्दुर, तादोंग - 737102
गंगटोक, सिक्किम, भारत
फोन-03592-251212, 251415, 251656
टेलीफैक्स - 251067
वेबसाइट - www.cus.ac.in




6th Mile, Samdur, Tadong-737102
Gangtok, Sikkim, India
Ph. 03592-251212, 251415, 251656
Telefax : 251067
Website : www.cus.ac.in

सिक्किम विश्वविद्यालय SIKKIM UNIVERSITY

(भारत के संसद के अधिनियम द्वारा वर्ष 2007 में स्थापित और नैक (एनएएसी) द्वारा वर्ष 2015 में प्रत्यायित केंद्रीय विश्वविद्यालय)
(A central university established by an Act of Parliament of India in 2007 and accredited by NAAC in 2015)


Declaration

I, Indra Hang Subba, declare that the thesis entitled "**Study of interaction between atoms and coherent light in magnetic field**" submitted by me for the award of **Doctor of Philosophy in Physics** of Sikkim University is my original work. The content of this thesis is based on the experiments which I have performed myself. This thesis has not been submitted for any other degree to any other University.


(Mr. Indra Hang Subba)
Roll No.: 14PDPY02
Regn No.: 14/PHD/PHY/02

Date: 24/11/22

Recommended that the Thesis to be placed before the Examiners for evaluation.


(Dr. Ajay Tripathi)
Supervisor
Associate Professor
Department of Physics
School of Physical Sciences
Sikkim University
Gangtok - 737102


Associate Professor
Department of Physics
Sikkim University

Date: 24/11/22

6 माइल, सामदुर, तादोंग - 737102
गंगटोक, सिक्किम, भारत
फोन-03592-251212, 251415, 251656
टेलीफैक्स - 251067
वेबसाइट - www.cus.ac.in



6th Mile, Samdur, Tadong-737102
Gangtok, Sikkim, India
Ph. 03592-251212, 251415, 251656
Telefax : 251067
Website : www.cus.ac.in

सिक्किम विश्वविद्यालय SIKKIM UNIVERSITY

(भारत के संसद के अधिनियम द्वारा वर्ष 2007 में स्थापित और नैक (एनएएसी) द्वारा वर्ष 2015 में प्रत्यापित केंद्रीय विश्वविद्यालय)
(A central university established by an Act of Parliament of India in 2007 and accredited by NAAC in 2015)

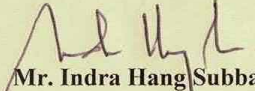
Date: 24/11/2022


PLAGIARISM CHECK CERTIFICATE

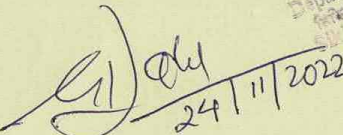
This is to certify that plagiarism check has been carried out for the following Ph.D. thesis with the help of **URKUND software** and the result is 2% which is within the permissible limit (below 10% tolerance rate) as per the norms of Sikkim University.

“Study of interaction between atoms and coherent light in magnetic field”

Submitted by **Mr. Indra Hang Subba** under the supervision of **Dr. Ajay Tripathi**, Department of Physics, School of Physical Sciences, Sikkim University, Gangtok, India.


Mr. Indra Hang Subba
(Signature of Candidate)


Dr. Ajay Tripathi
(Countersigned by Ph.D. supervisor)


Vetted by Librarian
Librarian
केन्द्रीय पुस्तकालय Central Library
सिक्किम विश्वविद्यालय
Sikkim University
24/11/2022

Associate Professor
Department of Physics
Sikkim University

Acknowledgements

My deepest and most sincere gratitude to my supervisor **Dr. Ajay Tripathi** for his continued support not just in doing physics but in my venture to join politics as well. I thank him for his patience, understanding, and willingness to help me complete this research thesis despite my uncertain daily routine. His keen interest in physics and politics alike has made the whole research journey enjoyable.

Thanks must also go to my juniors Mr. Ranjit Kumar Singh and Mr. Nayan Sharma, Ph.D research scholars in the department, for their support in the experiment as well as theoretical calculations.

Thanks to my good friends Dr. Rajesh Rawat and Dr. Nishal Rai for all their help to understand physics and its mischievous demands of both creativity and logic. I also thank all my friends who've constantly encouraged me to continue pursuing PhD despite all odds.

I thank my parents for their continued support during my research and their patience and belief in my decisions. It wouldn't have been possible to think of joining Ph.D course and ultimately completing it without encouragement and support from my dear brothers and sisters. The final stages of compiling this thesis were particularly tedious. Thanks to my loving wife for making it easier and more comfortable.

Last but not the least, thanks to all my friends who've helped me achieve this goal.

(Indra Hang Subba)

November, 2022

Abstract

Interaction between atoms and coherent monochromatic light has attracted much attention in recent decades. The coherence between atomic states has resulted in many counterintuitive but interesting observations. The rendering of opaque medium transparent under the condition of electromagnetically induced transparency (EIT) and enhanced absorption within a narrow range of frequency under the condition of electromagnetically induced absorption (EIA) has found many applications in developing quantum optical techniques. This thesis presents experimental results of laser interaction with rubidium(Rb) atomic vapour which leads to velocity selective optical pumping (VSOP), EIT and EIA. Further, EIT and EIA have been examined in presence of an external magnetic field.

First, we discuss VSOP to understand enhanced absorption caused by selective pumping of atomic population. We further discuss experimental results obtained for the probe field locked at different possible transitions. Lastly, the results for different pump intensities have been discussed.

Secondly, we discuss in detail the phenomenon of EIT. In presence of a transverse magnetic field, a single EIT peak splits into four. The separation between each peak depends on the strength of the magnetic field. For a higher magnetic field, asymmetry in the EIT spectrum is observed. The asymmetry observed is found to be caused by the presence of nearby states interacting with the system. The conversion from EIT to EIA can be controlled by a magnetic field. The longitudinal magnetic field splits the EIT peak into three. No asymmetry is observed in this configuration.

In the last chapter of this thesis, we discuss EIA in presence of the magnetic field. EIA spectrum changes in presence of a magnetic field due to the formation of multiple four-level N systems. The separation between the consecutive peaks depends linearly on magnetic field strength. The strength of the EIA peak reduces with decrease in the pump intensity.

The following publications contain the work presented in this thesis:

“Observation of electromagnetically induced absorption in 87Rb D2 line in strong transverse magnetic field”, **Indra Hang Subba** and Ajay Tripathi, *J. Phys. B: At. Mol. Opt. Phys.*, **51(15)**: 155001 (2018).

“Understanding asymmetry in electromagnetically induced transparency for 87Rb in strong transverse magnetic field”, **Indra Hang Subba**, Ranjit Kumar Singh, Nayan Sharma, Souvik Chatterjee, and Ajay Tripathi, *Eur. Phys. J. D*, **74**, 136 (2020).

“Competition between off-resonant and on-resonant processes in electromagnetically induced transparency in presence of magnetic field”, Ranjit Kumar Singh, Nayan Sharma, **Indra Hang Subba**, Souvik Chatterjee, and Ajay Tripathi, *Phys. Lett. A*, **416**: 127673 (2021).

Other publications:

“Anti-relaxation coating-induced velocity-dependent population re-distribution in electromagnetically induced transparency”, Nayan Sharma, Ranjit Kumar Singh, **Indra Hang Subba**, Souvik Chatterjee, and Ajay Tripathi, *Appl. Phys. B*, **68**, 129: (2023).

“Detuning dependent control of electromagnetically induced resonances assisted by additional velocity groups of atoms”, Ranjit Kumar Singh, Nayan Sharma, **Indra Hang Subba**, Souvik Chatterjee, and Ajay Tripathi. *Opt. Commun.*, **537**, 129466: (2023).

Presentations in National Conferences/Workshops

Indra Hang Subba, and A. Tripathi, “Observation of Electromagnetically Induced Absorption in 87Rb D₂ line in strong magnetic field”, 24th Raman Memorial Conference on Unravelling Physics of Advanced Materials, February 23-24, 2018, Department of Physics, Savitribai Phule Pune University, Pune (**POSTER presentation**).

Indra Hang Subba, and A. Tripathi, “Effects of transverse magnetic field on Electromagnetically Induced Absorption in 87Rb ”, Two-days National Conference on Trends in Science and Technology, February 27-28 February 2018, Departments of Computer Science & Applications and Mathematics, Salesian College, Siliguri, India (**ORAL presentation**).

Conference on "Recent Trends in Information Optics and Quantum Optics", 07-08, November 2014, Department of Physics, Indian Institute of Technology, Patna, India (**Participated**).

Two Days Hands-on Workshop using \LaTeX [TeX-2014], Nov. 15 - 16, 2014. Dept. of Computer Applications, Sikkim University, Gangtok, Sikkim, India (**Participated**).

Contents

Declaration	vi
Acknowledgements	vi
Abstract	vii
List of Publications	viii
List of Figures	xiii
List of Tables	xviii
Abbreviations	xx
Symbols	xxi
1 Introduction and Outline	1
1.1 Interaction of laser field with ^{87}Rb	3
1.1.1 Two-Level System	3
1.1.2 Three-Level System	9
1.1.3 Applications of EIT	17
1.2 Outline of the Thesis	18
2 Experiment	20
2.1 Laser System	20

2.1.1	Collimation of Laser Beam	21
2.1.2	Circularisation of the beam using anamorphic prism pair	21
2.1.3	Littrow Configuration	23
2.2	Atomic Vapor Cell	25
2.3	Detector	25
2.4	Acousto-Optic Modulator (AOM)	26
2.5	Magnetic System	27
2.6	Saturated Absorption Spectroscopy (SAS)	28
2.7	Locking of laser	32
3	Velocity selective optical pumping in $^{87}\text{Rb } D_2$ line	34
3.1	Introduction	34
3.2	Observation	36
3.2.1	VSOP spectrum when probe field locked at $F = 2 \rightarrow F' = 2$	36
3.2.2	VSOP spectrum for different lock positions of the probe field	40
3.2.3	Effect of pump intensity	42
4	Electromagnetically Induced Transparency	45
4.1	Introduction	45
4.2	Experimental Layout	47
4.3	EIT in three level Λ system in absence of magnetic field	49
4.4	EIT in presence of magnetic field	51
4.4.1	EIT in transverse magnetic field	51
4.5	The effect of nearby hyperfine states	58
4.5.1	Asymmetry in EIT due to strong magnetic field	58
4.5.2	The double Λ model	62
4.5.3	Controlling asymmetry in EIT	68
4.6	EIT in Longitudinal Magnetic Field	69
4.7	EIT in a degenerate two-level system	73
4.7.1	Effect of transverse magnetic field	74
4.7.2	Effect of pump intensity	75

5	Electromagnetically Induced Absorption	77
5.1	Introduction	77
5.2	Four-level N system: Theoretical Description	80
5.3	Probe response for DTLS system in presence of magnetic field	83
5.4	Experiment: Observation and Discussion	86
5.4.1	Layout of Experiment	86
5.4.2	Zero Magnetic Field	87
5.4.3	Non-zero magnetic field	89
5.4.4	Lande-g Factor	100
6	Conclusion and outlook	102
A	Appendix	106
	Bibliography	109

List of Figures

1.1	Electromagnetic field with incident frequency ω interacting with a two-level atomic system. Δ is the detuning of the field from the atomic resonance.	4
1.2	Time evolution of the probability. $\gamma = 0$ $\Omega = 1.2$ MHz. (a). $\Delta = 0$ (b). $\Delta = 0.35$ Ω	8
1.3	Time evolution of the probability. $\gamma = 0.2$ MHz $\Omega = 1.2$ MHz. (a). $\Delta = 0$ (b). $\Delta = 0.35$ Ω	9
1.4	^{87}Rb D_2 transition hyperfine structure.	10
1.5	Three Level Schemes (a) Λ Scheme, (b) V Scheme and (c) Ladder Scheme.	11
1.6	(a) Transmission as a function of pump detuning; (b) Real part of susceptibility χ versus pump detuning. Equation 1.38 is solved for $\Omega_p = 0.1\Gamma$ and $\Omega_c = 3.9\Gamma$; $\Delta_p = \Delta_c = 0$; $\gamma_2 = 0.01\Gamma$ and $\gamma_3 = \Gamma$. Γ (6 MHz) is the natural linewidth of ^{87}Rb.	17
2.1	Schematic showing positioning of lens for collimation of output laser beam	22
2.2	Schematic showing arrangement of anamorphic prism pair	23
2.3	Beam profiling; (a) Horizontal without anamorphic prism, (b) Horizontal with anamorphic prism, (c) Vertical without anamorphic prism and (d) Vertical with anamorphic prism.	24
2.4	Schematic of Littrow Configuration	25
2.5	Observed spectrum of SAS for ^{87}Rb D_2 line.	31
2.6	Level diagram illustrating transmission peaks corresponding to resonant and crossover transitions in SAS.	31
2.7	Schematic of LockIn module used for locking of laser frequency.	32
2.8	Illustrative plot for input signal from the SAS and its corresponding error signal.	33

3.1	Level diagram to illustrate positioning of each VSOP peaks when pump field is locked at $F = 2 \rightarrow F' = 2$ and probe is sweeping from $F = 1 \rightarrow F' = (0, 1, 2)$	37
3.2	Numerically obtained VSOP peaks for the probe locked at transition $F = 2 \rightarrow F' = 2$.	40
3.3	VSOP peaks for probe locked at different transitions	41
3.4	VSOP peaks for the pump locked at $F = 2 \rightarrow F' = 2$ and the probe is scanning from $F = 1 \rightarrow F' = (0, 1, 2)$	43
3.5	VSOP peaks for the pump locked at $F = 2 \rightarrow F' = 2$ and the probe is scanning from $F = 1 \rightarrow F' = (0, 1, 2)$	44
4.1	Schematic of the experimental setup. PD - Photodiode, M - 99.9% reflective mirror, PBS - Polarising beam splitter, HWP - Half-wave plate.	47
4.2	Energy level diagram for the three-level system in absence of magnetic field.	49
4.3	EIT for different pump intensity in absence of magnetic field. The probe power is fixed at 1.0 mW and the pump is varied from 3.0 to 4.5 mW.	50
4.4	E_{pu} and E_{pr} represent electric polarization of pump and probe field respectively, k represents propagation direction of laser and B is magnetic field direction. In (a) E_{pu} and B are perpendicular to each other and in (b) parallel. E_{pr} is perpendicular to E_{pu} .	52
4.5	Level diagram for illustration of possible Λ configurations. The solid lines in the level diagram show transition corresponding to π -polarised pump field and the dashed line corresponds to σ -polarised probe field.	52
4.6	The splitting of EIT resonance due to the externally applied transverse magnetic field. For case (a), the magnetic field is varied from 0 G to 13 G; for case (b) from 18 G to 32 G; and for case (c) from 32 G to 50 G.	54
4.7	Level diagram for illustration of possible Λ configurations. The solid lines in the level diagram show transition corresponding to the σ -polarised pump field and the dashed line corresponds to the π -polarised probe field.	56
4.8	Splitting of EIT resonance with probe π polarised and pump σ polarised. The applied magnetic field is 22 G.	57

4.9	Λ configurations in ^{87}Rb D_2 line for probe transition locked at $F = 1 \rightarrow F' = 2$ and $F = 2 \rightarrow F' = 2$. The blue solid line indicates Pump transition and the red dashed line indicates probe transition.	59
4.10	Experimental results for Λ_1 configuration, (a). for different values of magnetic field at $P_{pu} = 3.5\text{mW}$ and $P_{pr} = 0.3\text{mW}$, (b) for increasing pump power at $B = 40$ G.	59
4.11	All possible Λ configurations for probe transition locked at $F = 1 \rightarrow F' = 2$. The blue solid line indicates Pump transition and the red dashed line indicates σ^+ and the red dotted line indicates σ^- probe transition.	60
4.12	All possible Λ configurations for probe transition locked at $F = 2 \rightarrow F' = 2$. The blue solid line indicates pump transition, the red dashed line indicates σ^+ and the red dotted line indicates σ^- probe transition.	61
4.13	Experimental results for Λ_2 configuration, (a). for different values of magnetic field at $P_{pu} = 2.4\text{mW}$ and $P_{pr} = 0.3\text{mW}$, (b) for increasing pump power at $B = 40$ G.	62
4.14	Four-level double Λ system with common ground states.	63
4.15	Theoretical curves. (a). $c_{ij} = 1$ for all $i \rightarrow j$, $\Omega_{pu} = 2 \times \gamma$, $\Omega_{pr} = \gamma$, (b). $c_{ij} = 1$ for all $i \rightarrow j$, $\Omega_{pu} = 4 \times \gamma$, $\Omega_{pr} = \gamma$. $\gamma = 2\pi \times 6\text{MHz}$	67
4.16	Experimental (solid) and Numerical (dashed) spectra corresponding to the peak A_3 of Λ_1 configuration. (a). $P_{pr} = 0.3$ mW and $P_{pu} = 2.4$ mW. (b). $P_{pr} = 0.3$ mW and $P_{pu} = 5.6$ mW.	67
4.17	Level diagram for illustration of possible Λ configurations. The solid lines in the level diagram signify the pump field and the dashed line probe field, both are σ polarised.	69
4.18	Splitting of EIT resonance due to the presence of a longitudinal magnetic field.	71
4.19	EIT linewidth for different values of the magnetic field.	71
4.20	EIT linewidth for different values of pump power. The plot shows how EIT linewidth increases with pump power magnetic field zero and 22 G.	72
4.21	Dependence of separation between two consecutive EIT peaks on the magnetic field.	73
4.22	Level diagram illustrating degenerate two-level system (DTLS).	74

4.23 (a) Response of EIT spectrum to the applied magnetic field. (b) Linear dependence of separation between EIT peaks.	75
4.24 Effect of pump intensity EIT for a fixed value of the magnetic field.	76
5.1 Energy level diagram of one of the four level N system formed by π polarised pump and σ^- polarised beam	81
5.2 Theoretically obtained EIA curve with following parameters; $\Delta_{C1} = \Delta_{C2}$, $\frac{\Omega_C}{\Omega_P} = 10$, $\Gamma \equiv 6$ MHz, Clebsch-Gordan coefficients: $C_{12}=C_{21}=\sqrt{\frac{4}{15}}$, $C_{34}=C_{43}=\sqrt{\frac{3}{10}}$, $C_{23}=C_{32}=\sqrt{\frac{1}{6}}$	82
5.3 Four types of resonance: I-shaped two level (a), V-shaped three level (b) , Λ -shaped three level (c) and N-shaped four level (d). Series of V-shaped three level resonances for π -polarized pump and σ -polarized probe (e). Series of Λ and V-shaped three level resonances for π -polarized pump and σ -polarized probe (f). Thick line indicates the pump transition , thin line for probe transition and dotted line indicates the spontaneous decay	84
5.4 Theoretical probe transmission spectra with following parameters: $\frac{\Omega_C}{\Omega_P} = 10$, Overall detuning factor $\delta \leq 10$ MHz, Spontaneous decay rate $\Gamma \equiv 6$ MHz. First Column: π -polarized pump with magnetic field 20 G, 30 G and 40 G. Second Column: σ -polarized pump with magnetic field 20 G, 30 G and 40 G.	86
5.5 Experimental setup for observation of EIA and the effect of magnetic field. PBS-Polarizing beam splitter; HWP-Half wave plate; PD-photodiode; VC-vapor cell; SAS-Saturated Absorption Spectroscopy setup.	87
5.6 EIA for different lock points. Applied magnetic field $B = 0$ G. For each of the spectra recorded, the pump detuning axis is calibrated with respect to the lock point.	88
5.7 EIA properties for zero magnetic field.(a) Percentage absorption. (b) EIA linewidth vs pump power.	89
5.8 Level diagram illustrating all possible Zeeman transitions in presence of the transverse magnetic field. A_1 , A_2 and A_3 represent Zeeman transitions corresponding to $ F = 2\rangle \rightarrow F' = 3\rangle$, $ F = 2\rangle \rightarrow F' = 2\rangle$ and $ F = 2\rangle \rightarrow F' = 1\rangle$ respectively for π polarised pump field and B_1 , B_2 and B_3 corresponding to σ polarised pump.	90

5.9	(a)Transition strength and (b) branching ratio - between different Zeeman sub-levels corresponding hyperfine transition $F=2 \rightarrow F'=3$ to illustrate dynamics of the population distribution process.	91
5.10	Experimentally observed probe transmission for different values of the magnetic field with π -polarized pump beam; (a) weak magnetic field, (b) strong magnetic field. The spectrum recorded for the fixed pump and probe intensity of 20 mW/cm^2 and 0.9 mW/cm^2 respectively.	92
5.11	Energy level diagram showing all the possible Zeeman transitions with corresponding transition strength for π (solid red) and σ^\pm (dashed green) polarised beam.	94
5.12	EIA shift from transmission as a function of applied magnetic field.In inset non-degenerate N-type system formed by π -polarized pump and σ^- -polarized probe. Δ_{C1} and Δ_{C2} are pump detuning and Δ_P is the probe detuning.	94
5.13	Experimentally observed probe transmission for different values of the magnetic field with π -polarized pump beam; (a) weak magnetic field, (b) strong magnetic field. The spectrum recorded for the fixed pump and probe intensity of 20 mW/cm^2 and 0.9 mW/cm^2 respectively.	96
5.14	Transmission spectra were recorded for different values of pump intensity at a fixed transverse magnetic field of 40 G as a function of pump detuning. The spectrum recorded is for σ^\pm -polarized pump and π -polarized probe.	98
5.15	Measured EIA linewidth as a function for magnetic field for π -polarized pump (dash line) and for σ -polarized (solid line).	99
5.16	Theoretical (dashed) and experimental (solid) probe transmission spectra with EIA dip as a function of pump detuning for applied magnetic field of 20 G (a) , 30 G (b) and 40 G(c)	100
5.17	Measured EIA separation as a function of the magnetic field. The Lande-g factor for hyperfine ground states belonging to $5^2S_{1/2}$ (b).The Lande-g factor for hyperfine excited states belonging to $5^2P_{3/2}$ (c). In (b) and (c) solid line indicates theoretical g_F and $g_{F'}$ respectively	101

List of Tables

2.1	Arrangement of anamorphic prism pair	23
2.2	Calculation of Responsivity of the photodiode detector at 780 nm	26
2.3	Tuning Voltage (V) vs Frequency (MHz)	27
2.4	Magnetic field calibraion	27
3.1	Relative position of VSOP peak's when the probe laser is locked from F=2 to F'=2 transition	38
3.2	The relative position of VSOP peak's when the probe laser is locked from F=2 to F'=1 transition	41
3.3	The relative position of VSOP peak's when the probe laser is locked from F=2 to F'=3 transition	41
3.4	The relative position of VSOP peak's when the probe laser is locked from F=1 to F'=0 transition	42
3.5	The relative position of VSOP peak's when the probe laser is locked from F=1 to F'=1 transition	42
3.6	The relative position of VSOP peak's when the probe laser is locked from F=1 to F'=2 transition	42
4.1	EIT position corresponding to each Λ in the presence of transverse magnetic field corresponding to figure 4.5	54
4.2	EIT position corresponding to each Λ in presence of transverse magnetic field corresponding to figure 4.7	57
4.3	EIT positions corresponding to each Λ system for Λ_1 configuration.	60
4.4	EIT positions corresponding to each Λ system for Λ_1 configuration.	61
4.5	I_D values for different double Λ system.	65

4.6	EIT position corresponding to each Λ in the presence of longitudinal magnetic field corresponding to figure 4.17	70
4.7	EIT position corresponding to each Λ in DTLS	74
A.1	Physical properties	107
A.2	Optical Properties	107
A.3	Relative hyperfine transition strength factors for D_2 line	107
A.4	Hyperfine Dipole Matrix element for σ^+ transition ($F = 2, m_F \rightarrow F', m_{F'} = m_F + 1$)	107
A.5	Hyperfine Dipole Matrix element for π transition ($F = 2, m_F \rightarrow F', m_{F'} = m_F$)	107
A.6	Hyperfine Dipole Matrix element for σ^- transition ($F = 2, m_F \rightarrow F', m_{F'} = m_F - 1$)	108
A.7	Hyperfine Dipole Matrix element for σ^+ transition ($F = 1, m_F \rightarrow F', m_{F'} = m_F + 1$)	108
A.8	Hyperfine Dipole Matrix element for π transition ($F = 1, m_F \rightarrow F', m_{F'} = m_F$)	108
A.9	Hyperfine Dipole Matrix element for σ^- transition ($F = 1, m_F \rightarrow F', m_{F'} = m_F - 1$)	108

Abbreviations

CPT	Coherent Populatiom Trapping
LWI	Lasing Without Inversion
FWM	Four Wave Mixing
EIT	Electromagnetically Induced Transparency
EIA	Electromagnetically Induced Absorption
VSOP	Velocity Selective Optical Pumping
ECDL	External Cavity Diode Laser
SAS	Saturated Absorption Spectroscopy
EIT	Electromagnetically Induced Transparency
FWHM	Full Width Half Maxima
AOM	Acousto-Optic Modulator
PID	Proportional Integral Derivative
HWP	HalfWave Plate
DTLS	Degenerate Two Level System
TOC	Transfer Of Coherence
TOP	Transfer Of Population

Symbols

E	Electric field
T	Temperature
Δ	Detuning
π	Pi-transition
ρ	Density matrix element
α	Absorption Coefficient
γ	Decay rate
Γ	Natural Linewidth
δ	Two photon detuning
Ω	Rabi Frequency
ω	Laser frequency
c_{ij}	Transition strength coefficient
I_D	Impurity in the dark state
m_F	Magnetic quantum number
μ	micro
m	milli
λ	Wavelength
H	Hamiltonian
Rb	Rubidium
G	Gauss
σ	Sigma transition
χ	Susceptibility
B	Magnetic Field
F	Hyperfine quantum number

Hz Hertz

Chapter 1

Introduction and Outline

The term "light-matter interaction"[1] refers to the interactions between matter and light. Classically, it refers to the study of the interaction between an oscillating light field and charged particles. Classical theory is enough to understand the linear absorption, dispersion, and scattering processes. On the other hand, if the matter is treated as quantum particles, the light can be viewed as a perturbation to the associated quantum states, which can explain various non-linear optical processes (semi-classical theory) [2]. The studies in the field of light-atom interaction propelled significantly after the invention of the laser (a coherent source of light) [3, 4]. It has opened many aspects of understanding the nature of atoms at the subatomic level [5]. In particular, the precision of spectroscopy has increased exponentially. For example, alkali atoms like Rb with non-zero nuclear spin exhibit hyperfine splitting of energy levels, which is masked under the Doppler width [6, 7]. With the invention of low-cost diode lasers in the infrared regime, a number of techniques like saturated absorption spectroscopy and polarization spectroscopy have been developed to unmask the Doppler broadening [8–10]. Alkali atoms like sodium [11], cesium [12], rubidium[13] till date have remained system of interest to study atom-light interaction. This is because their single valence electron simplifies the atomic structure, and the presence of a strong transition at an available low-cost diode laser wavelength makes them interesting both experimentally and theoretically [14]. Because of this, progress in atomic

physics experiments involving alkali atoms has evolved from hot vapor[15] to ultra-cold atoms [16]. The simplicity of atomic vapor experiments has again attracted the interest of experimentalists in the area of atomic physics. The development of quantum technologies involving atomic vapor[17] in the fields of quantum computation [18], metrology [19], magnetometry[20], quantum sensors[21] e.t.c., has increased many fold in the last few decades.

The alkali atoms have been thoroughly investigated in two-level systems [22]. The results obtained have been utilized to model complex atomic models in a two-level configuration [23, 24]. The studies in this field have progressed past studying two-level systems as the theory and experiments have advanced with time. When a field interacts with a quantum system with more than two atomic energy levels, the coherence between two adjacent states leads to counter-intuitive observations. In a simple three-level Λ system, under the condition that adjacent transitions have an equal light-wave frequency detuning from the frequency of the corresponding transition, dark states are formed[25]. In this situation, the excited state is devoid of any population. All the population of the system is trapped in the coherence formed by the lower states. This particular phenomenon is termed CPT[26]. When a coherent electromagnetic field interacts with an atomic system, a distinct phase relationship between them exists [27]. Unless disturbed by incoherent processes like spontaneous decay and collisional dephasing, their phase is retained, which is known as the stationary state of the system. The system in a stationary state can be well described within the framework of quantum mechanics. In this situation, superposition and interference play an important role. The interplay of superposition and interference has been utilised to understand the various experimentally observed phenomena in atomic vapour, such as coherent population trapping (CPT) [26, 28, 29], lasing without inversion (LWI)[30–32], four-wave mixing(FWM) [33–35], electromagnetically induced transparency (EIT)[36–38] and electromagnetically induced absorption (EIA)[39–42]. Out of these various phenomena, EIT and EIA are studied widely since these processes can be realized with very low laser powers at room temperature, these two processes remain an interesting topic of research for their high tunability and dependence on various controllable external parameters, especially the

magnetic field, which is the main objective of this thesis. These studies have potential applications in optical switching [43] and quantum magnetometry[20]. The basics of light-atom interactions in two level systems and three level systems have been elaborately discussed in detail in the following subsection 1.1.1 of section 1.1 and subsection 1.1.2 of section 1.1.

1.1 Interaction of laser field with ^{87}Rb

The simplest configuration for atomic interaction with the electromagnetic field is a two-level system. Even other atomic configurations with multiple states involved can be considered to consist of more than one two-level systems interfering with each other. Three level system consists of two two-level systems with one of the states common to both. Therefore, it is the basic unit of multi-level configurations. We consider the semi-classical theory to explain the observation. The atomic medium is considered a quantum system and the electromagnetic light is assumed to be classical. In subsections 1.1.1 and 1.1.2 we have discussed theoretically how electromagnetic field interacts with the two-level and three-level atomic system respectively.

1.1.1 Two-Level System

To investigate theoretically, how electromagnetic field interacts with two-level system, we consider a monochromatic electromagnetic field propagating in the z-direction interacting with **an ensemble of two-level atoms** as shown in figure 1.1.

The electric field vector is given by,

$$\vec{E} = \vec{E}_0 \cos(\omega t - kz) \quad (1.1)$$

where, $k = \frac{2\pi}{\lambda}$ is the wave vector.

For all practical purposes, the effective radius of an atom can be taken to be very small as compared to the wavelength of the electromagnetic field i.e., $\lambda \gg z$. This is the dipole

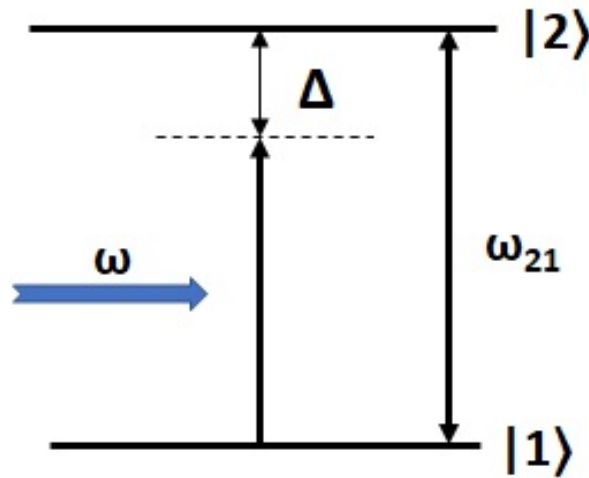


FIGURE 1.1: Electromagnetic field with incident frequency ω interacting with a two-level atomic system. Δ is the detuning of the field from the atomic resonance.

approximation in which the spatial variation of the field can be neglected ($kz \ll 1$). Therefore,

$$\vec{E} = \vec{E}_0 \cos(\omega t) \quad (1.2)$$

where, ω is the frequency of the laser light.

The total Hamiltonian for the system is given by,

$$H_T = H_0 + H_I \quad (1.3)$$

where, H_0 is the bare atom Hamiltonian and H_I is the interaction Hamiltonian.

We have,

$$H_0 = \begin{pmatrix} \hbar\omega_1 & 0 \\ 0 & \hbar\omega_2 \end{pmatrix}$$

and,

$$H_I = -q\vec{E} \cdot \hat{r} \quad (1.4)$$

This form is classically equivalent to the interaction energy of an electric dipole kept in an

external electric field. Under the assumption that dipole is aligned with the field, H_I can be written as,

$$H_I = -pE \quad (1.5)$$

In semi-classical theory the electric dipole moment needs to be treated as an operator. Hence, \mathbf{p} ($= q\hat{r}$) in the above expression is the electric dipole moment operator having matrix elements $p_{mn} = \langle n|p|m\rangle$.

The interaction Hamiltonian in the matrix form is given by,

$$H_I = -E \begin{pmatrix} 0 & p_{12} \\ p_{21} & 0 \end{pmatrix}$$

To understand in detail the interaction of the field with the electric dipole, transformation to the interaction picture is needed which is achieved by using a unitary matrix given by,

$$U(t) = e^{\frac{iH_0 t}{\hbar}} = \begin{pmatrix} e^{i\omega_1 t} & 0 \\ 0 & e^{i\omega_2 t} \end{pmatrix}$$

In the interaction picture H_I transforms to UH_IU^\dagger i.e.,

$$-E \begin{pmatrix} 0 & p_{12} \\ p_{21} & 0 \end{pmatrix} \rightarrow -E \begin{pmatrix} 0 & p_{12}e^{-i(\omega_2-\omega_1)t} \\ p_{21}e^{i(\omega_2-\omega_1)t} & 0 \end{pmatrix}$$

also, the electric field can be written as,

$$E = \frac{E_0}{2}(e^{i\omega t} + e^{-i\omega t}) \quad (1.6)$$

which gives,

$$UH_IU^\dagger = -E_0 \begin{pmatrix} 0 & \frac{p_{12}}{2}(e^{-i(\omega_{21}-\omega)t} + e^{-i(\omega_{21}+\omega)t}) \\ \frac{p_{21}}{2}(e^{i(\omega_{21}-\omega)t} + e^{i(\omega_{21}+\omega)t}) & 0 \end{pmatrix}$$

Two different frequencies of the system $\omega_{21} - \omega$ and $\omega_{21} + \omega$ appears in the interaction Hamiltonian. At this point an important approximation known as rotating wave approximation (RWA) is used where the quickly varying phase term $(\omega_{21} + \omega)t$ can be dropped. As per RWA, since the frequency term $\omega_{21} + \omega$ is much larger than the relevant energy scales of the system it is often neglected in equations of motion. After applying the RWA and transforming back ($U^\dagger(UH_IU^\dagger)U$) to the Schrodinger's picture, the Hamiltonian is given by,

$$H_T = \hbar \begin{pmatrix} \omega_1 & -\frac{\Omega}{2}e^{i(\omega t + \phi)} \\ -\frac{\Omega}{2}e^{-i(\omega t + \phi)} & \omega_2 \end{pmatrix}$$

where, ϕ is the phase of the dipole which is defined as, $p_{12} = p_{21}^* = |p_{12}|e^{i\phi}$ and $\Omega = \frac{|p_{12}|E_0}{\hbar}$ is the the Rabi frequency. Further simplification of the Hamiltonian can be done by identifying a time and phase independent basis (co-rotating frame). It is achieved by using the unitary matrix,

$$U_t = \begin{pmatrix} e^{-i(\omega t + \phi)} & 0 \\ 0 & 1 \end{pmatrix}$$

and as a result, the Hamiltonian in a time and phase independent basis is given by[44]

$$\bar{H} = i\hbar \frac{\partial U_t}{\partial t} U_t^\dagger + U_t H_T U_t^\dagger \quad (1.7)$$

which in the matrix form can be written as,

$$\bar{H} = \begin{pmatrix} \omega_1 + \omega & -\frac{\Omega}{2} \\ -\frac{\Omega}{2} & \omega_2 \end{pmatrix}$$

Finally, by re-scaling the energy by subtracting $(\omega_1 + \omega) \mathbb{I}$ we have,

$$H = \begin{pmatrix} 0 & -\frac{\Omega}{2} \\ -\frac{\Omega}{2} & \Delta \end{pmatrix}$$

where, $\Delta = \omega_{21} - \omega$ is defined as the detuning of the laser from the resonant transition $|1\rangle \rightarrow |2\rangle$.

For the dynamics of an ensemble of two level atoms in density matrix formulation[25] the following master equation is used,

$$\dot{\rho} = -\frac{i}{\hbar}[H, \rho] + \Lambda\rho \quad (1.8)$$

where,

$$\Lambda\rho = \begin{pmatrix} \gamma\rho_{22} & -\frac{\gamma}{2}\rho_{12} \\ -\frac{\gamma}{2}\rho_{21} & -\gamma\rho_{22} \end{pmatrix}$$

is the matrix introducing the effect of phenomenological decay terms such as spontaneous decay (γ). The equations of motion for the density matrix elements are,

$$\dot{\rho}_{11} = -i\frac{\Omega}{2}(\rho_{12} - \rho_{21}) + \gamma\rho_{22} \quad (1.9)$$

$$\dot{\rho}_{22} = -i\frac{\Omega}{2}(\rho_{21} - \rho_{12}) - \gamma\rho_{22} \quad (1.10)$$

$$\dot{\rho}_{12} = -i\frac{\Omega}{2}(\rho_{22} - \rho_{11}) - \left(\frac{\gamma}{2} - i\Delta\right)\rho_{12} \quad (1.11)$$

$$\dot{\rho}_{21} = i\frac{\Omega}{2}(\rho_{22} - \rho_{11}) - \left(\frac{\gamma}{2} + i\Delta\right)\rho_{21} \quad (1.12)$$

The solution of the equations (ρ_{11} and ρ_{22}) gives the time evolution of the probability of the atom being in state $|1\rangle$ and $|2\rangle$ respectively. Figure 1.2 (a) shows the numerical result for the case when there is no decay ($\gamma=0$). As seen from the figure the occupancy probability undergoes continuous oscillation with a frequency of Ω (Rabi oscillations) for $\Delta = 0$. The presence of finite detuning ($\Delta = 0.35\Omega$) results in the decrease of the amplitude of the occupancy probability as seen from figure 1.2 (b).

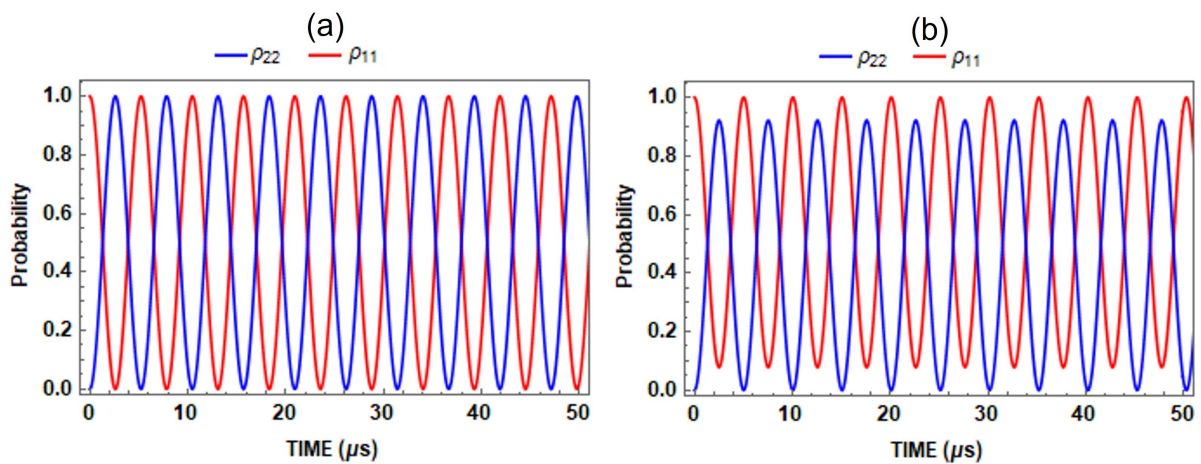


FIGURE 1.2: Time evolution of the probability. $\gamma = 0$ $\Omega = 1.2$ MHz. (a). $\Delta = 0$ (b). $\Delta = 0.35$ Ω .

The time evolution of the occupancy probability incorporating the effect of the spontaneous decay is shown in figure 1.3. Figure 1.3 (a) is for the case when the laser is at the resonance ($\Delta = 0$), unlike the case of no decay (figure 1.2), here the occupancy probability reaches a stationary value of 0.5. **This suggests that the population will be equally distributed among the ground and excited state. In presence of finite detuning ($\Delta = 0.35\Omega$), the occupancy probability of both states becomes unequal as shown in figure 1.3(b). In general, as the value of the detuning is increased the probability of finding the atoms in excited state becomes smaller and hence more number of atoms settles in the ground state.**

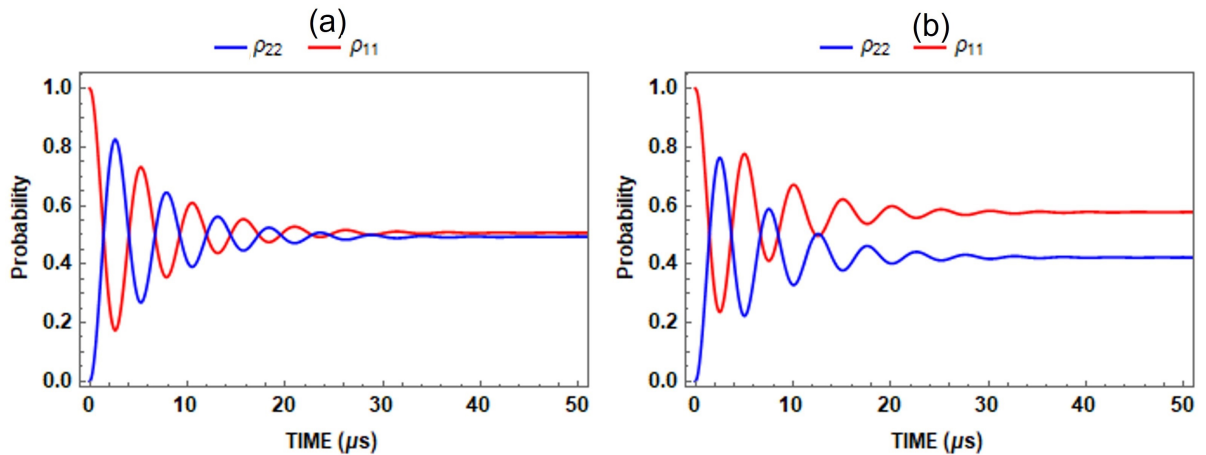


FIGURE 1.3: Time evolution of the probability. $\gamma = 0.2\text{MHz}$ $\Omega = 1.2\text{MHz}$. (a). $\Delta = 0$ (b). $\Delta = 0.35\Omega$.

1.1.2 Three-Level System

The three-level system has a special reputation in studies related to light-matter interaction. This is because under certain circumstances it has the ability to exhibit counter-intuitive results. One such phenomenon is the inability of the atomic ensemble to interact with the electromagnetic field at a specific frequency. This happens because of the trapping of the population in the superposition states called the dark state. **The dark state leads to the transmission of a weak field on resonance in presence of a strong one [38]. The reason for such altered optical behavior of an atomic medium is due to the induced coherence of atomic states. This coherence results in a quantum interference between the various excitation pathways of an electron between the energy states. Each of these paths can interfere with each other, leading to changes in the probability of the field either being absorbed or transmitted. Orthogonal to the dark state, one can define a bright state which is related to the absorption of the field [45]. The presence of such sub-Doppler phenomena effects the propagation of light in atomic medium (by inducing sudden change in the refractive index) as discussed further in this chapter (see equation 1.38 and 1.39). As a result, the group velocity of propagating electromagnetic field changes resulting into subluminal (slow) and superluminal (fast) propagation of light in an atomic medium [46–48]. The propagation of light can be slowed down to an extent that it**

can be completely stopped [49, 50]. The complete stoppage of light in EIT medium has been utilized to realize optical quantum memory where photon is a source of qubit [51].

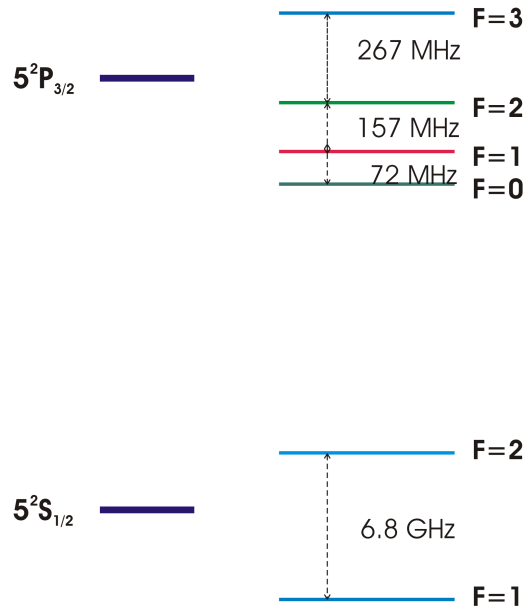


FIGURE 1.4: ^{87}Rb D_2 transition hyperfine structure.

To obtain a pure dark state in three level system, the frequency detuning between adjacent transitions is equal i.e. the two-photon detuning is zero. In this condition, the probability of finding an atom in the upper state is ideally zero. The first reported phenomenon of this type is CPT. Subsequently, EIT was predicted and reported [37, 52]. Since then extensive study has been carried out on the applications and optimization of EIT. The possible three-level configurations are shown in figure 1.5. The first ever EIT was reported by SE Harris *et al.* in the strontium vapor using a three-level Λ configuration. This configuration consists of two dipole forbidden ground states $|1\rangle$ and $|2\rangle$ coupled to an excited state $|3\rangle$. The excited state $|3\rangle$ is coupled to ground state $|1\rangle$ by probe field with Rabi frequency Ω_p and $|2\rangle$ by pump field Ω_c . The pump field is higher in intensity than the probe. Later on, when the study on EIT was extended, it was also observed in V (Vee) and Ladder system. V configuration consists of two dipole-forbidden excited states and a ground state coupled by pump and probe field shown in figure 1.5(b). Ladder configuration consists of a ground state coupled to an excited state through an intermediate state as shown

in figure 1.5(c). In the Ladder system, the ground state $|1\rangle$ and the excited state $|3\rangle$ are dipole forbidden.

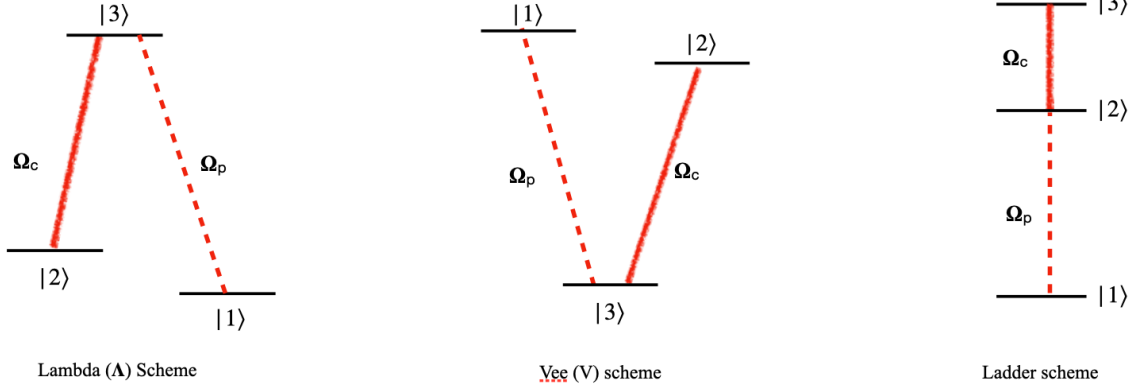


FIGURE 1.5: Three Level Schemes (a) Λ Scheme, (b) V Scheme and (c) Ladder Scheme.

Results discussed in the subsequent chapters of this thesis are observed using a three-level Λ configuration consisting of ground and excited hyperfine states of ^{87}Rb D_2 line as shown in figure 1.4. In presence of a magnetic field, however, multiple Λ configurations come into play involving Zeeman sublevels. Our study is entirely based on the findings in presence of a magnetic field. In the following subsections, we discuss the basic theory of how a coherent light source interacts with the three-level Λ system.

Hamiltonian of the three-level Λ system

Similar to the two-level system, the interaction between atoms and laser field in an atomic medium is described by total Hamiltonian,

$$H_T = H_0 + H_I \quad (1.13)$$

where, H_0 is the bare state and H_I represents interaction Hamiltonian. Using the aforementioned Dipole approximation, the the total field is represented by,

$$\vec{E} = \frac{\vec{E}_p}{2}(e^{-i\omega_p t} + e^{i\omega_p t}) + \frac{\vec{E}_c}{2}(e^{-i\omega_c t} + e^{i\omega_c t}) \quad (1.14)$$

where, $\{|\vec{E}_p\rangle, |\vec{E}_c\rangle\}$ are the amplitude and $\{\omega_p, \omega_c\}$ are the frequency of the probe and pump beam respectively. The interaction Hamiltonian is given by,

$$H_I = -\hat{d}E(t) \quad (1.15)$$

where, \hat{d} is the dipole operator whose matrix elements are defined as,

$$d_{ij} = \langle i|\hat{d}|j\rangle \quad i, j \in \{1, 2, 3\}$$

Since for the Λ system the dipole transition between the ground states is forbidden we have,

$$d_{12} = d_{21} = 0.$$

With the application of RWA and defining the Rabi frequencies Ω_p and Ω_c as,

$$\Omega_p = \frac{E_0|d_{13}|}{\hbar}, \quad \Omega_c = \frac{E_0|d_{23}|}{\hbar} \quad (1.16)$$

the total Hamiltonian of the system can be rewritten in the matrix form as,

$$H_T = \begin{pmatrix} \hbar\omega_1 & 0 & -\frac{\hbar\Omega_p}{2} e^{i(\omega_p t + \phi_p)} \\ 0 & \hbar\omega_2 & -\frac{\hbar\Omega_c}{2} e^{i(\omega_c t + \phi_c)} \\ -\frac{\hbar\Omega_p}{2} e^{-i(\omega_p t + \phi_p)} & -\frac{\hbar\Omega_c}{2} e^{-i(\omega_c t + \phi_c)} & \hbar\omega_3 \end{pmatrix} \quad (1.17)$$

ϕ_p and ϕ_c are the phases of the dipoles defined as,

$$d_{13} = d_{31}^* = |d_{13}|e^{i\phi_p}$$

$$d_{23} = d_{32}^* = |d_{23}|e^{i\phi_c}$$

To eliminate the time and phase dependence, unitary matrix of the following form can be used,

$$U_t = \begin{pmatrix} e^{-i(\omega_p t + \phi_p)} & 0 & 0 \\ 0 & e^{-i(\omega_c t + \phi_c)} & 0 \\ 0 & 0 & 1 \end{pmatrix} \quad (1.18)$$

Therefore, the final transformed Hamiltonian in the co-rotating frame (equation 1.7) is given by,

$$H = \hbar \begin{pmatrix} 0 & 0 & -\frac{\Omega_p}{2} \\ 0 & \Delta_p - \Delta_c & -\frac{\Omega_c}{2} \\ -\frac{\Omega_p}{2} & -\frac{\Omega_c}{2} & \Delta_p \end{pmatrix} \quad (1.19)$$

where, $\Delta_p = \omega_{13} - \omega_p$ and $\Delta_c = \omega_{23} - \omega_c$ are the probe and the pump detuning respectively.

EIT dynamics

Interaction of an atomic ensemble with the laser field leads to distribution of population, absorption of laser field, and dispersion. These phenomena can be described well by density matrix formalism involving density matrix in the interaction picture which is given by the following equation,

$$\dot{\rho} = -\frac{i}{\hbar}[H, \rho] - \frac{1}{2}\{\Gamma, \rho\} \quad (1.20)$$

where, Γ in terms of decay rate γ is defined by

$$\langle n|\Gamma|m\rangle = \gamma_n \delta_{nm}$$

For Λ system γ_1 can be taken zero assuming that the ground state $|1\rangle$ is decay free. γ_3 incorporates the spontaneous decay out of the excited state $|3\rangle$ and γ_2 is used to add the effects of collisional decay in the system. From equations 1.19 and 1.20, we obtain coupled

differential equations also known as Optical Bloch equations:

$$\dot{\rho}_{11} = -i\frac{\Omega_p}{2}(\rho_{13} - \rho_{31}) \quad (1.21)$$

$$\dot{\rho}_{22} = -i\frac{\Omega_c}{2}(\rho_{23} - \rho_{32}) - \gamma_2\rho_{22} \quad (1.22)$$

$$\dot{\rho}_{33} = i\frac{\Omega_p}{2}(\rho_{13} - \rho_{31}) - i\frac{\Omega_c}{2}\rho_{32} - \gamma_3\rho_{33} \quad (1.23)$$

$$\dot{\rho}_{31}^* = \dot{\rho}_{13} = -i\frac{\Omega_p}{2}(\rho_{11} - \rho_{33}) - i\frac{\Omega_c}{2}\rho_{12} - (\gamma_{13} - i\Delta_p)\rho_{13} \quad (1.24)$$

$$\dot{\rho}_{32}^* = \dot{\rho}_{23} = -i\frac{\Omega_c}{2}(\rho_{22} - \rho_{33}) - i\frac{\Omega_p}{2}\rho_{21} - (\gamma_{23} - i\Delta_c)\rho_{23} \quad (1.25)$$

$$\dot{\rho}_{21}^* = \dot{\rho}_{12} = i\frac{\Omega_p}{2}\rho_{32} - i\frac{\Omega_c}{2}\rho_{13} - (\gamma_{12} - i(\Delta_p - \Delta_c))\rho_{12} \quad (1.26)$$

where, $\gamma_{ij} = \frac{\gamma_i + \gamma_j}{2}$ is the decay rate for the off-diagonal terms and the *'s denote the complex conjugates. ρ_{11} , ρ_{22} and ρ_{33} are the diagonal matrix elements which gives the population of states $|1\rangle$, $|2\rangle$ and $|3\rangle$ respectively. The off-diagonal elements ρ_{13} , ρ_{23} and ρ_{12} are related to the coherence among the states. In the regime where the probe beam is weak ($\Omega_p \ll \Omega_c$), following assumptions can be made to further simplify the equations

$$\rho_{11} \approx 1 \quad (1.27)$$

$$\rho_{22} = \rho_{33} \approx 0$$

Finally, neglecting the terms which are proportional to Ω_p^2 (weak probe) the equations can be reduced to,

$$\dot{\rho}_{31}^* = \dot{\rho}_{13} = -i\frac{\Omega_p}{2} - i\frac{\Omega_c}{2}\rho_{12} - (\gamma_{13} - i\Delta_p)\rho_{13} \quad (1.28)$$

$$\dot{\rho}_{21}^* = \dot{\rho}_{12} = -i\frac{\Omega_c}{2}\rho_{13} - (\gamma_{12} - i(\Delta_p - \Delta_c))\rho_{12} \quad (1.29)$$

By solving these equations for ρ_{13} in the steady state case ($\dot{\rho}_{12} = 0 = \dot{\rho}_{13}$) we have,

$$\rho_{13} = \frac{2\Omega_p(\Delta_p - \Delta_c - i\gamma_{12})}{[\Omega_c^2 - 4(\gamma_{13} - i\Delta_p)(\gamma_{12} - i(\Delta_p - \Delta_c))]} \quad (1.30)$$

This off-diagonal element ρ_{13} is used to calculate the susceptibility of the medium as discussed in next section.

Absorption and Dispersion

Comparison between the polarization $'P'$ and the susceptibility $'\chi'$ of the medium leads to relation between absorption and dispersion of the medium with the density matrix element. Maxwell defined displacement vector as,

$$D = \epsilon_o E + P \quad (1.31)$$

But for a linear medium of permittivity ϵ ,

$$D = \epsilon E \quad (1.32)$$

Comparison of equation 1.31 and 1.32 gives,

$$P = (\epsilon - \epsilon_o)E \quad (1.33)$$

Susceptibility of the medium is defined as,

$$\chi = \frac{\epsilon}{\epsilon_o} - 1 \quad (1.34)$$

From equations 1.33 and 1.34,

$$P = \epsilon_o \chi E = \frac{\epsilon_o E_p}{2} \chi(\omega_p)(e^{-i\omega_p t} + e^{i\omega_p t}) + \frac{\epsilon_o E_c}{2} \chi(\omega_c)(e^{-i\omega_c t} + e^{i\omega_c t}) \quad (1.35)$$

Also the polarization of the atomic ensemble with number density $'N'$ is the net dipole moment per unit volume which is given by,

$$P = N \langle \hat{d} \rangle = N \text{Tr}(\rho' \hat{d})$$

$$P = N(d_{31}\rho_{13}e^{i(\omega_p t + \phi_p)} + d_{32}\rho_{23}e^{i(\omega_c t + \phi_c)} + d_{13}\rho_{31}e^{-i(\omega_p t + \phi_p)} + d_{23}\rho_{32}e^{-i(\omega_c t + \phi_c)}) \quad (1.36)$$

The trace is taken over $\rho' \rightarrow U_t^\dagger \rho U_t$ where the system is transformed back from the co-rotating frame. Comparing equations 1.35 and 1.36 expression for susceptibility in terms of density matrix element ρ_{13} is given by,

$$\chi(\omega_p) = \frac{2N|d_{13}|^2}{\epsilon_0\Omega_p\hbar}\rho_{13} \quad (1.37)$$

The final expression for the complex susceptibility using equation 1.30 is,

$$\chi(\omega_p) = \frac{2N|d_{13}|^2}{\epsilon_0\Omega_p\hbar} \frac{2\Omega_p(\Delta_p - \Delta_c - i\gamma_{12})}{[\Omega_c^2 - 4(\gamma_{13} - i\Delta_p)(\gamma_{12} - i(\Delta_p - \Delta_c))]} \quad (1.38)$$

The imaginary part of χ gives absorption and the real part is associated with the dispersion of the probe field. In presence of a pump, we observe a transmission of weak probe at two photon resonance condition ($\delta = \Delta_p - \Delta_c = 0$) as shown in figure 1.6(a). This transmission peak is called EIT. At that particular frequency, we observe a positive gradient of the dispersion spectrum. Because of the positive linear dispersion of the refractive index, as mentioned before EIT is associated with slowing down of the group velocity according to the equation[38],

$$v_g \equiv \left. \frac{d\omega_p}{dk_p} \right|_{\delta=0} = \frac{c}{n + \omega \frac{\partial n}{\partial \omega_p}} \quad (1.39)$$

where, $n = \sqrt{1 + Re(\chi)}$ is the refractive index of the material and k_p is the wave vector of the probe beam. This important relation leads to the application of EIT in slow light. The greater the positive gradient slower is the group velocity. EIT facilitates the slowing of light at the transition frequency where otherwise the probe beam gets absorbed.

In this thesis we have experimentally studied EIT and EIA in $^{87}\text{Rb } D_2$ line in presence of an external magnetic field. EIT and EIA are observed depending on the number of states interacting with the field in a given system. In presence of the magnetic field, the degeneracy of the hyperfine state is lifted resulting in multiple subsystems. The interaction of the probe field depends upon

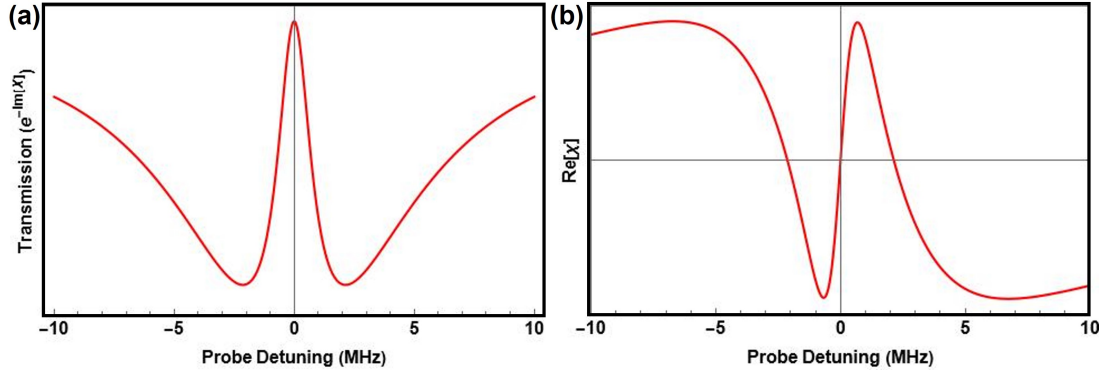


FIGURE 1.6: (a) Transmission as a function of pump detuning; (b) Real part of susceptibility χ versus pump detuning. Equation 1.38 is solved for $\Omega_p = 0.1\Gamma$ and $\Omega_c = 3.9\Gamma$; $\Delta_p = \Delta_c = 0$; $\gamma_2 = 0.01\Gamma$ and $\gamma_3 = \Gamma$. Γ (6 MHz) is the natural linewidth of ^{87}Rb .

the available subsystems formed by Zeeman sublevels. The presence of an additional state leads to the transformation of EIT to EIA and vice versa due to the transfer of coherence [53]. We have investigated the basic characteristics of both EIT and EIA in presence of the magnetic field.

1.1.3 Applications of EIT

With an EIT medium, it has been demonstrated that the slowing of light is possible. Manipulation of group velocity, v_g , has been demonstrated in various mediums including ^{87}Rb . $\frac{\partial \eta}{\partial \omega}$ in equation 1.39 gives the gradient in dispersion. Around EIT resonance, the gradient is positive and very large as shown in figure 1.6 (b) which results in reduced velocity. The observation of small group velocities of 17 ms^{-1} was first demonstrated in a Bose-Einstein condensate of sodium atoms in [54]. The medium was maintained at the temperature of the order of nK. The slowing of group velocity in hot Rb atomic vapor was also demonstrated by Kash *et al.* [55] in 1999. They observed reduced velocity of the order 90 ms^{-1} .

EIT also finds an important application in scalar as well as vector magnetometry. It has been well established that the relative amplitude of each EIT peak contains information regarding the magnitude and direction of the magnetic field [56]. Therefore, sharp EIT resonance is an ideal candidate for the development of a magnetometer. There are many advantages of EIT scalar magnetometry, such as insensitivity to quadratic Zeeman and AC stark effects, atom-buffer,

and atom-atom collision. As far as vector magnetometry based on EIT is concerned, compass sensitivity of 10^{-3} degree / $\text{Hz}^{1/2}$ has been achieved [57].

The phenomena of EIT find its applications in optical switching [58], especially for developing a high-speed and more practical optical switch for next-generation communication network [59]. The laser-induced coherence can also find its application for subluminal to superluminal light propagation [48] by either controlling the phase of the laser [60] or by using an additional beam [61]. Beside using continuous lasers, this application is also well pronounced for pulsed lasers [62] or for Laguerre laser beams [63]. The main benefit of this all-optical switch is that the optical signals can be transferred between multiple sources without converting to an electric signal. An additional conditional for having the application of EIT in optical switches is the high-fidelity transmission which means transferring the information with minimum loss or distortion. It is where controlling the birefringence in an atomic medium also plays an important role. This birefringence produces rotation in the atomic medium. It is therefore along with EIT and the optical rotation, that high-fidelity transmission can be achieved [64]. The two closely related phenomena can also find its application for generating ultranarrow-bandwidth filter [65], all-optical drop filters [66], plasmonic filters [67] or FADOF [68].

1.2 Outline of the Thesis

In the thesis, we have experimentally observed EIT and EIA in presence of magnetic field. Sections 1.1.1 and 1.1.2 of this chapter discuss in detail the theoretical aspects of interaction of laser field with ^{87}Rb atomic vapor. In chapter 2, we discuss all the components and procedures used during the experiment. In chapter 3, we study velocity selective optical pumping (VSOP) in ^{87}Rb D_2 line. We also discuss the effects of pump and probe power, the occurrence and the conditions required for EIT. In chapter 4, we discuss in detail the effects of the magnetic field on EIT. The discussion is further extended to understand the effects of nearby hyperfine states and the asymmetry observed at higher magnetic field using double Λ model. At the end of the chapter we have discussed in brief the effects of magnetic field and pump power of EIT observed in degenerate

two level system(DTLS). In chapter 5, we discuss in detail the EIA phenomenon and the effects of magnetic field. The EIA cannot be explained by three-level system. Therefore, four-level N configuration is theoretically described.

Chapter 2

Experiment

2.1 Laser System

The basic laser system consists of three components viz. diode laser, collimating lens, and diffraction grating. The diode serves as an active material for light emission with a broad gain spectrum. The lens is mounted in front of the diode laser ensuring proper collimation. Strong wavelength selective feedback from the grating forces the laser diode to operate in a single longitudinal mode. The linewidth of the laser after feedback is significantly reduced. An extended cavity diode laser is one where the cavity of the diode laser is extended because of the grating setup. Generally, the linewidth of the extended cavity diode laser ranges from 100 kHz to a few MHz. On the other hand, the external cavity diode laser is one where the grating setup is kept in a separate cavity external to the diode laser cavity. With this setup, the linewidth of the laser can further be reduced to a few kHz. A diffraction grating in the external cavity is mounted in Littrow configuration such that the light diffracted in the first order is reflected to the laser.

With any laser, a change in the length of the cavity leads to a frequency change in the laser output. To avoid frequency fluctuation of the laser output any change in thermal as well as mechanical state should be avoided. To avoid mechanical vibration laser diode is attached to a fixed holder and cushioned with soft rubber. To avoid thermal changes the base plate to which the extended

cavity is mounted is temperature controlled using a thermistor. However, the temperature of the diode is independently controlled. To fine-tune laser frequency piezoelectric transducer is used. With this, it is possible to control the length of the cavity accurately using input voltage.

In the experiment, we use two independent sources of laser. Both the lasers used in the experiment are 780 nm single mode external cavity diode lasers (ECDL) with an output capacity of 70 mW. Their linewidth is specified to be 1 MHz. One laser is used as a pump and the other one is used as a probe. Our experiment requires that one of them is locked at a specified transition frequency, which can be achieved using the Saturated Absorption Spectroscopy (SAS) technique discussed in section 2.6, and the other laser is kept scanning.

2.1.1 Collimation of Laser Beam

The output of the laser is typically elliptical. Edge-emitting laser diodes emit elliptical beams because their active region of emission is typically rectangular. The emitted beam is highly divergent. The smaller the dimension of the aperture greater the divergence. Since the emitting aperture is rectangular the divergence is greater along the shorter side than that along the longer side. The divergence ranges from 8° on the longer side to 25° along the shorter side of the rectangular aperture. To minimize the divergence of the emergent beam collimation technique is required. It is usually done by using a spherical lens of a particular dimension at an appropriate position as shown in figure 2.1. The relationship between the half height of the collimated beam r , the focal length of the lens f , and divergent angle θ is

$$f = \frac{r}{\tan \frac{\theta}{2}}$$

2.1.2 Circularisation of the beam using anamorphic prism pair

We use a pair of anamorphic prisms to reshape an elliptical laser beam to a circular one. In an anamorphic prism, the beam intersects the external front and back surfaces at different angles due

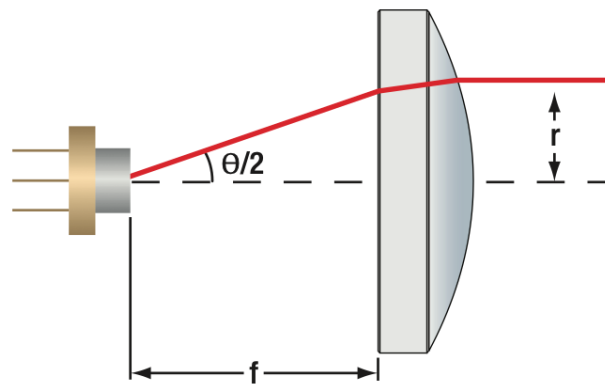


FIGURE 2.1: Schematic showing positioning of lens for collimation of output laser beam

to the asymmetric alignment of the surfaces. This leads to a change in the resultant dimension of the laser output ($h_1 \neq h_2$) as shown in figure 2.2. A single anamorphic prism is enough to expand or contract the beam dimension, however, the direction of the beam also changes. Therefore, we use an additional anamorphic prism to realign the direction of the beam parallel to the original direction. Thus, a pair of anamorphic prisms leads to a change in the laser beam dimension with a small lateral shift of the beam.

The laser is operating in a single mode and has a Gaussian beam profile. The original beam profile is elliptical. We estimate the width of the beam using the **slit** method where we measure power at different points across the beam. Then, we plot these points as shown in figure 2.3. We repeat this for four different situations;

1. Along horizontal plane (parallel to the surface of the table) without anamorphic prism pair - figure 2.3(a)
2. Along horizontal plane with anamorphic prism pair - figure 2.3(b)
3. Along vertical plane (perpendicular to the surface of the table) without anamorphic prism pair - figure 2.3(c)
4. Along vertical plane with anamorphic prism pair - figure 2.3(d)

TABLE 2.1: Arrangement of anamorphic prism pair

Magnification	α_1 (deg)	α_2 (deg)
4.2	35.9	2.8

Full-width Half Maxima (FWHM) in the plot obtained by points observed without an anamorphic prism gives an idea of how much magnification of the beam on the thinner side is required. In our case, the magnification required is 4.2. With this we calculate all the required parameters for the placement of an anamorphic prism to form a pair, the value of which is tabulated in table 2.1. The emergent beam is now circular. The FWHM observed of the beam on either side is 0.56 mm and 0.57 mm. The diameter of the beam is measured at $\frac{1}{e^2}$ times the maximum. The measured value of beam diameter is found to be 0.2 cm. We have used this value for the entire experiment without disturbing the position of the anamorphic prism pair.

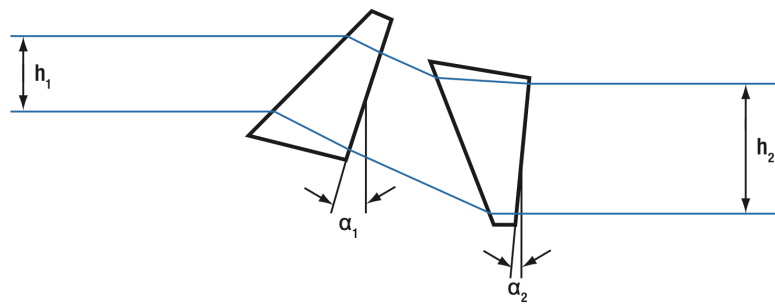


FIGURE 2.2: Schematic showing arrangement of anamorphic prism pair

2.1.3 Littrow Configuration

Diffraction grating is positioned in Littrow configuration the schematic of which is shown in figure 2.4. The grating equation with incident angle α and diffracted angle β is given by

$$d(\sin\alpha \pm \sin\beta) = m\lambda$$

where d is the line spacing between the gratings, λ is the wavelength of the incident beam and m is the diffraction order.

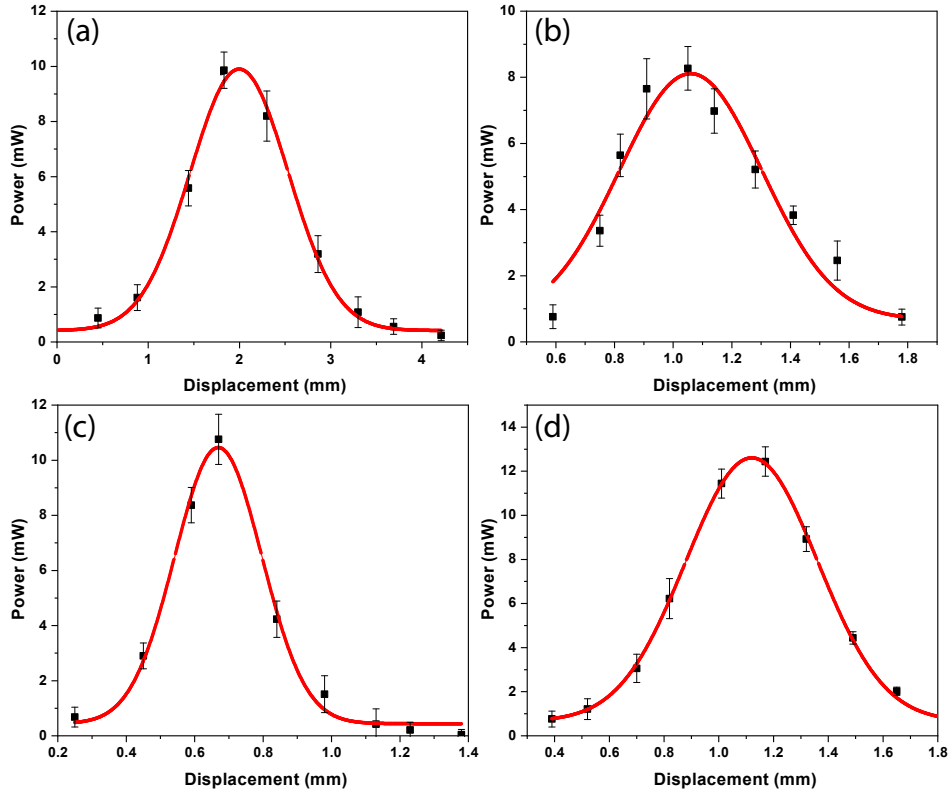


FIGURE 2.3: Beam profiling; (a) Horizontal without anamorphic prism, (b) Horizontal with anamorphic prism, (c) Vertical without anamorphic prism and (d) Vertical with anamorphic prism.

In Littrow configuration, the incident angle is equal to the diffracted angle of the first order i.e $\alpha = \beta = \beta_L$. Therefore, Littrow angle in terms of incident wavelength is defined as,

$$\beta_L = \sin^{-1}\left(\frac{\lambda}{2d}\right)$$

$$\frac{d\lambda}{d\beta} = 2d\cos\beta$$

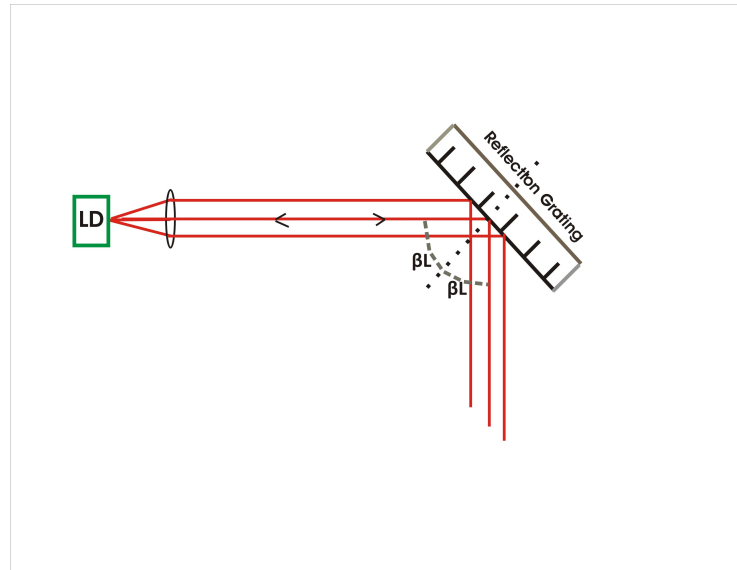


FIGURE 2.4: Schematic of Littrow Configuration

2.2 Atomic Vapor Cell

Atomic vapor is contained in a cylindrical glass cell of diameter 2 cm and length 3 cm placed at center of the Helmholtz coil. Sample contained in the glass cell is Rubidium vapor - a mixture of isotopes ^{85}Rb (72%) and ^{87}Rb (28%). Throughout experiment, vapor cell is maintained at a constant temperature of 40°C.

2.3 Detector

In the experiment, we used a photodiode detector for the detection of the probe and measurement of its power. The specified responsivity of the photodiode is 0.6 V/A at 800 nm with variable gain which can be changed from 10 M Ω to 333 Ω in ten steps. Response of the photodiode is specified to be linear from 0 to -11 V. Responsivity of a photodetector is wavelength depended and is different for lasers with different wavelengths. The laser in the experiment is 780 nm. Therefore, to measure probe power we recalculate the responsivity of the photodiode. The relation between the input power P of the laser, photocurrent I_p , and responsivity R is

TABLE 2.2: Calculation of Responsivity of the photodiode detector at 780 nm

I_{in} (mA)	V_{out} (V)	Power (mW)	R (A/W)
50	368	2.76	0.40
60	1340	8.54	0.47
70	1603	11.86	0.42
80	1629	12.00	0.40

$$P = \frac{I_p}{R}$$

Responsivity of the photodetector for 780 nm laser is found to be 0.4225 A/W as shown in table 2.2.

2.4 Acousto-Optic Modulator (AOM)

Deflection angle introduced in the original path of the laser field with wavelength Λ due to change in radio frequency ΔF is given by,

$$\Delta\theta = \frac{\Lambda\Delta F}{V}$$

where, V is acoustic velocity of the medium.

Change in frequency of the applied laser field with wavelength 780 nm due to AOM is tabulated in the table 2.3.

TABLE 2.3: Tuning Voltage (V) vs Frequency (MHz)

Sl. No.	Tuning Voltage (V)	Frequency (MHz)
1	0	71
2	0.1	86
3	0.2	90
4	0.3	100
5	0.4	106
6	0.5	111
7	0.6	119
8	0.7	125
10	0.8	131
11	0.9	147
12	1.0	156

TABLE 2.4: Magnetic field calibration

Sl. No.	Voltage (V)	Magnetic field B (Gauss)
1	0	0
2	2	9
3	4	18
4	6	27
5	8	36
6	10	45
7	12	54
8	14	63
10	16	72
11	18	81
12	20	90

2.5 Magnetic System

Magnetic field is generated using Helmholtz coil with diameter 16 cm and resistance 10 Ω . Magnetic field is controlled using power supply which can provide DC voltage upto 20 V. Calibration of magnetic field output from Helmholtz coil with the input voltage is done using Gauss meter, data of which is shown in table 2.4.

2.6 Saturated Absorption Spectroscopy (SAS)

The energy states involved in the D_2 line transition are the components of the fine-structure doublet. The splitting of fine structure is due to coupling between orbital angular momentum ' L ' of the outer electron and its spin angular momentum ' S '. The fine structure angular momentum is given by

$$J = L + S \quad (2.1)$$

and the corresponding quantum number J lies in the range

$$|L - S| \leq J \leq |L + S| \quad (2.2)$$

Coupling of J with total nuclear angular momentum I leads to further splitting of fine structure into hyperfine, the total angular momentum of which is given by

$$F = J + I \quad (2.3)$$

The magnitude of F ranges between

$$|J - I| \leq F \leq |J + I| \quad (2.4)$$

The D_2 line transition is from $5^2 S_{1/2} \rightarrow 5^2 P_{3/2}$ where fine structure energy levels P and S split into two and four hyperfine states respectively as shown in figure 1.4. The hyperfine energy states can be resolved by SAS technique.

The atomic sample used is a ^{87}Rb gas enclosed in cell with diameter 2 cm and length 3 cm. The atoms enclosed go random thermal motion. The laser frequency in atomic reference is decided by the velocity and direction of the atom's motion. If the laser is propagating in the z -direction, than the frequency of the radiation absorbed by an atom is ,

$$\nu_L = \nu_0 \left(1 + \frac{v_z}{c}\right) \quad (2.5)$$

where, ν_0 is the resonant absorption frequency at rest v_z is the z-component of the atom's velocity.

Thermal motion of atoms in the rubidium cell the wide range of velocity distribution leads to absorption of wide range of laser frequency. This effect leads to masking of features of the absorption spectra corresponding to hyperfine structure. This broad spectrum due to velocity distribution is termed as doppler broadening. The velocity distribution of atoms in the cell can be best represented by Maxwell distribution. The probability of atoms with velocity between v and $v+dv$ is given by,

$$P(v_z)dv_z = \sqrt{\frac{M}{2\pi k_B T}} \exp\left(\frac{-Mv^2}{2k_B T}\right) dv \quad (2.6)$$

From equation 2.5,

$$dv_z = \frac{c}{\nu_0} d\nu_L \quad (2.7)$$

Using equation 2.7 we rewrite equation 2.6 in terms of frequency,

$$P(\nu_L)d\nu_L = \frac{2}{\delta\sqrt{\pi}} \exp\left[\frac{-4(\nu_L - \nu_0)^2}{\delta^2}\right] d\nu_L \quad (2.8)$$

where,

$$\delta = \frac{2\nu_0}{c} \sqrt{\frac{2k_B T}{M}}$$

Full width half maximum of the given doppler distribution is given by,

$$\Delta\nu_{\frac{1}{2}} = \delta\sqrt{\ln(2)} \quad (2.9)$$

We use SAS technique to eliminate this doppler broadening. In this technique, two laser fields of the same frequency interact with the atomic resonance in a counter-propagating configuration. This configuration produces an absorption signal that contains features ordinarily unresolved due to the doppler spectrum. The absorption of the probe beam is proportional to the difference in population between the ground and the excited states. The steady-state population difference is given by[69],

$$\Delta N(\nu_L, v_z) = \Delta^0(v_z) \left[1 - \frac{\frac{I}{I_{SAT}}}{1 + \frac{I}{I_{SAT}} \left(\frac{2\Delta}{\Gamma} \right)^2} \right] \quad (2.10)$$

The detailed derivation of this expression can also be found in ref. [70]. When the intensity of the pump beam is greater than saturation intensity ' I_{SAT} ' and the population difference tends to zero, we see a sharp decrease in the absorption of the probe field at resonance. Figure 2.5 represents transmission peaks at resonances and crossover interacting with transitions $F = 2 \rightarrow F' = (1, 2, 3)$. This is obtained by subtracting the doppler broadened absorption spectrum from the original SAS spectrum obtained from the same vapor cell. We observe six transmission peaks. Three peaks corresponding to resonant transitions $F = 2 \rightarrow F' = 1$, $F = 2 \rightarrow F' = 2$ and $F = 2 \rightarrow F' = 3$ and three for crossover resonances.

When the pump and probe laser fields interact with the $v_z = 0$ class of atoms we observe sharp transmission peaks at perfect resonance. However, there exists one class of velocity that sees pump and probe fields resonant with upper and lower neighboring hyperfine states respectively. This leads to crossover transmission peaks exactly at the mid-frequency of adjacent hyperfine states. Crossover resonances are often more prominent because of the higher probability of atoms with non-zero velocity. We use this spectrum to lock the frequency of the laser at desired resonance.

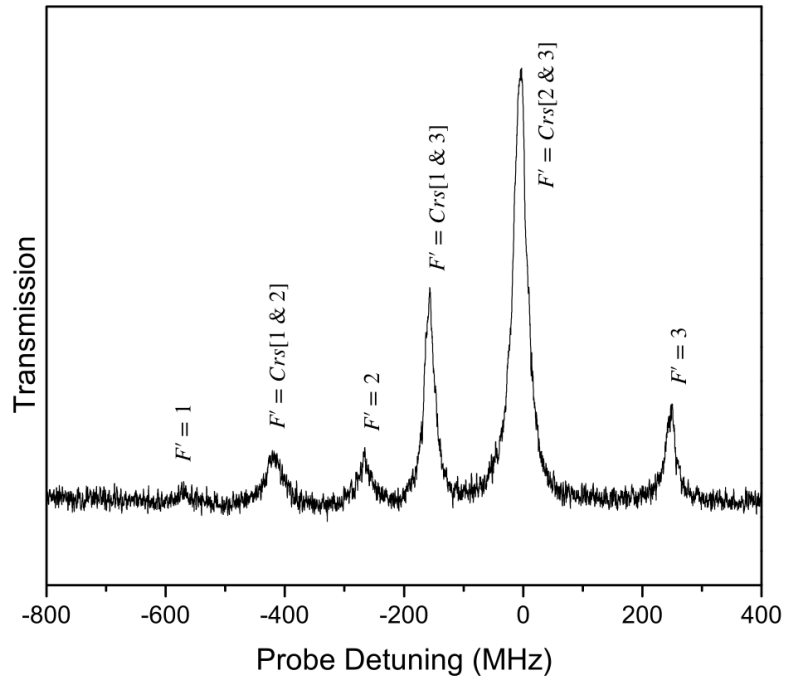


FIGURE 2.5: Observed spectrum of SAS for ^{87}Rb D_2 line.

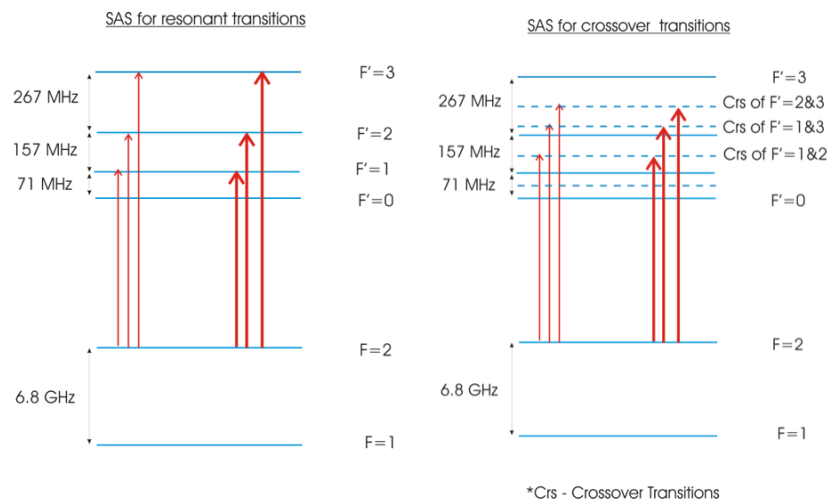


FIGURE 2.6: Level diagram illustrating transmission peaks corresponding to resonant and crossover transitions in SAS.

2.7 Locking of laser

Signal obtained from SAS is fed to the Lock-In module where an error signal is generated by applying frequency modulation to the original signal. The error signal is then fed to the system through PID (Proportional-Integral-Derivative) controller. PID controller takes the error signal and optimizes the feedback for the system to reach its setpoint as fast as possible and stabilizes the laser at a fixed frequency. The block schematics for how the error signal is fed back to the system is shown in figure 2.7.

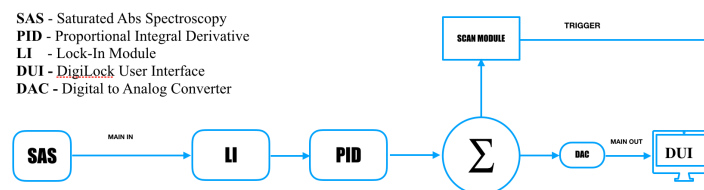


FIGURE 2.7: Schematic of LockIn module used for locking of laser frequency.

We use the top of the fringe locking using the Lock-In technique. The error signal produced is the derivative of the input signal. It shows a continuous slope and a zero crossing at the resonance frequency as shown in figure 2.8 and is well suited for locking. Once the feedback for the system is optimized, laser frequency can be locked using DigiLock User Interface.

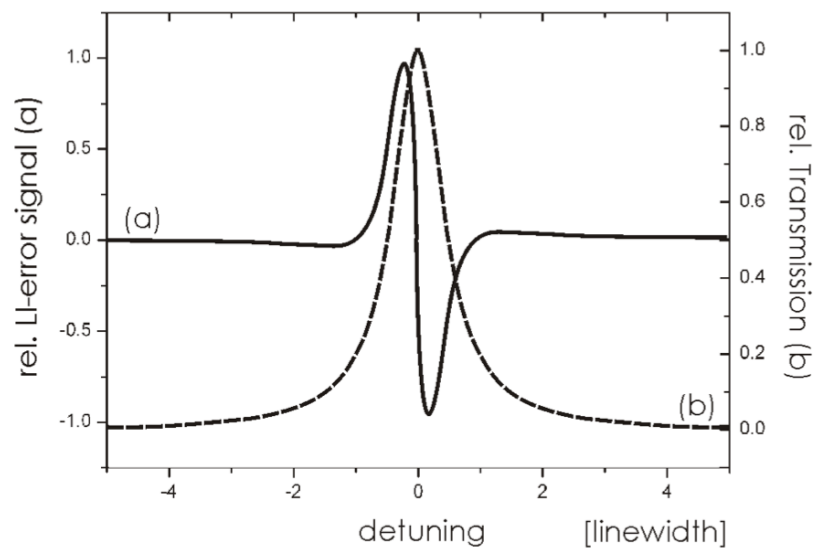


FIGURE 2.8: Illustrative plot for input signal from the SAS and its corresponding error signal.

Chapter 3

Velocity selective optical pumping in ^{87}Rb

D_2 line

3.1 Introduction

Absorption spectroscopy has its importance from the very beginning of modern physics as it is an important tool for understanding light-matter interaction. This spectroscopy is limited because of various effects which broaden the linewidth of the spectral lines. A well-known factor responsible for broadening is the Doppler effect which is because of the velocity distribution of atoms. This generates a broad absorption profile known as the Doppler profile which encapsulates spectral lines caused by individual energy states. However, with the invention of a single-mode laser, it has become possible to probe individual energy states. One well-known spectroscopic technique for generating a Doppler-free profile is SAS [9] which helps in resolving the hyperfine transitions. And the other is velocity selective optical pumping (VSOP)[71, 72] which provides tools to probe the various relaxation process in an atomic system. Mainly, the relaxation process induced by collisions [73] can be probed and controlled using this technique. In addition, it provides information about the resonant velocity groups of atoms in an atomic ensemble which can find application in various fields such as generation of optical filters[74] or controlling the lineshape

of various spectroscopic features[75]. However, the frequent collision of atoms, such as in the case of a buffer cell, can destroy the VSOP peaks due to the velocity mixing[76].

It is usually performed using two co-propagating laser fields with different frequencies. For observing this phenomena experimentally, one of the lasers is locked to a particular frequency and the other is kept in scanning mode. For a pure three-level system, one broad peak is observed. In this case, the velocity selective transitions of a group of atoms having non-zero velocities satisfying the resonance will occur. This will in turn will enhance the absorption of the probe for a particular resonant velocity class [77]. However, in a system with more than one excited state and one of the laser fields scanning across all the states, multiple VSOP are observed. By using a laser with narrow bandwidth, the correlation between the velocity of atoms and the internal variables (hyperfine population differences, orientation, alignment, etc.) of the atomic system becomes strong [71]. So, by having both the lasers strong, the population re-alignment of the atomic system will overshadow the information of velocity. Therefore, probe intensity is usually kept negligible as compared to the pump intensity to get the information of all the resonant velocity classes.

Unlike saturation spectroscopy, this method provides a Doppler-free resonance absorption line, without saturating the atomic population. Therefore, the pump intensity doesn't need to be greater than saturation intensity for observing this phenomena. The absorption lines in this method are usually without power broadening of the excited state depending on pump intensity [71]. It only requires that one of the states be long-lived, preferably ground or a meta-stable state. Also, the characteristic relaxation time of the observable is much larger than in saturation spectroscopy[72].

One important aspect of light-atom interaction is associated with optical coherence between the states. This coherence is generally created by near-resonant or multi-near-resonant fields with intermediate states. However, optical coherence between the two ground levels can be neglected for extremely low and equal laser intensity of lasers. But, by having unequal laser intensity, the coherence between the two ground states can be established. As mentioned before, this coherence under the particular condition leads to phenomena like

EIT, CPT, or EIA. Therefore, VSOP peak with this condition will carry a transmission or an absorption peak having a sub-natural linewidth[78] commonly referred to as EIT or EIA.

By having co-propagating laser beams, both the principal resonance and Doppler-shifted resonance lines can be obtained. In this configuration, the cross-over resonance lines are absent. This spectroscopy also depends on the polarization of the lasers [79]. The intensity of velocity selective resonance peak changes with different combination of polarisation of pump and probe. Ref. [79] have attributed this change as the redistribution of atomic population among non-degenerate magnetic sublevels embedded in the hyperfine states. The study further noted that transition strength plays a vital role in defining the strength and profile of the velocity selective resonance peaks. These peaks can be characterized and understood using the rate equations [80] and also by solving the density matrix equations [81] as discussed later in this chapter.

In this work, we have studied this phenomena in ^{87}Rb D_2 line where the locked laser can interact with three possible velocities due to the Doppler effect. These velocity class with which pump laser interacts depends upon the frequency separation between the adjacent hyperfine states. Further, we also solved the rate equations to reproduce the experimental observations.

3.2 Observation

3.2.1 VSOP spectrum when probe field locked at $F = 2 \rightarrow F' = 2$

^{87}Rb D_2 line consists of six hyperfine states with six possible resonant transitions. However, in a vapor cell, a laser field locked to one particular resonance interacts with three velocity classes v_1 , v_2 , and v_3 due to the presence of three nearby hyperfine states. In figure 3.1(a), we have designated ground states as 1 and 2 and the excited state as 3, 4, 5, and 6 respectively. To illustrate how velocity selective interaction affects the resultant spectrum we consider the case where the probe field is locked at $F = 2 \rightarrow F' = 2$ detuned from the resonance by kv_2 . For the same

lock point, the probe field may be considered to have detuned from $F' = 1$ and $F' = 3$ by kv_1 and kv_3 respectively. This leads to nine sets (three sets for each detuning) of Raman resonance conditions between the probe and the pump field. The entire spectrum of VSOP is a result of the fulfillment of these nine sets of Raman resonance conditions. For convenience we have indicated all the possible pump transitions by alphabets a to i in figure 3.1(a). The probe field is indicated in the figure by a solid line whereas the possible transition for the pump is indicated by a dashed line.

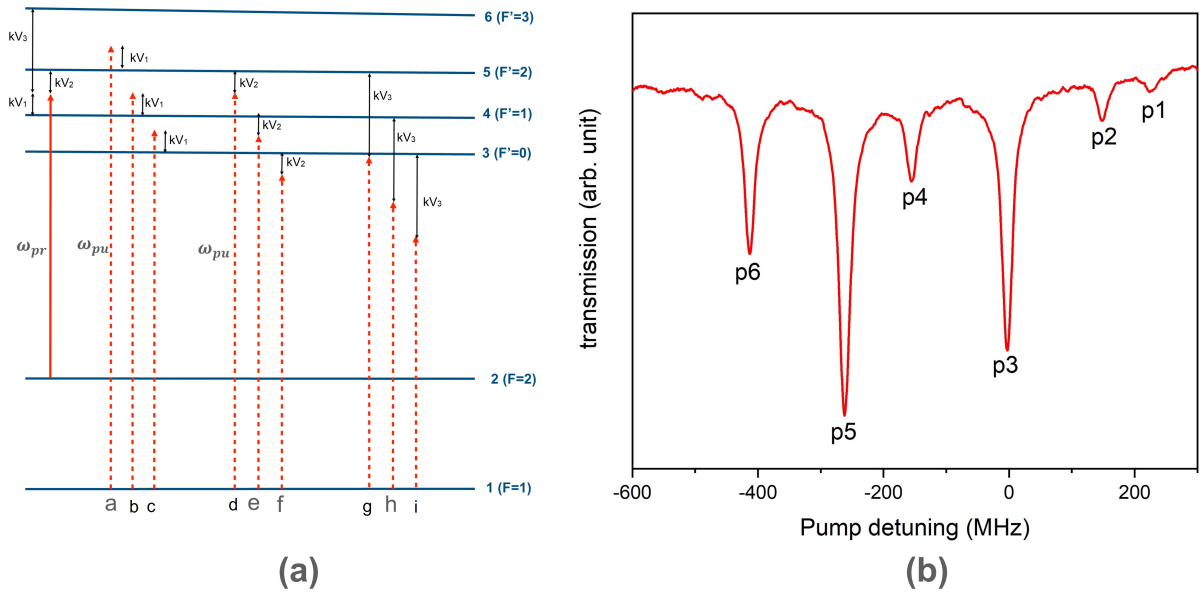


FIGURE 3.1: Level diagram to illustrate positioning of each VSOP peaks when pump field is locked at $F = 2 \rightarrow F' = 2$ and probe is sweeping from $F = 1 \rightarrow F' = (0, 1, 2)$

To ascertain the positioning of the peaks as observed in the experimental result shown in figure 3.1(b) we have calculated all the possible resonance conditions. The Raman resonance conditions for probe transition corresponding to velocity class v_1 are given by equation 3.1 to 3.3, for v_2 by equation 3.4 to 3.6 and for v_3 by equation 3.7 to 3.9. The experimental results for a fixed pump and probe power of 0.03 mW each are shown in figure 3.1(b).

TABLE 3.1: Relative position of VSOP peak's when the probe laser is locked from $F=2$ to $F'=2$ transition

Peak label	Calculated value (MHz)	Measured value (MHz)
p1	-	226
p2	$\Delta_2=157$	153
p3	0	0
p4	$-\Delta_2=-157$	-154
p5	$-\Delta_3=267$	-262
p6	$-(\Delta_2+\Delta_3)=-424$	-420

$$\omega_{pr} = \omega_{pu} + \Delta_{12} + \Delta_2 \quad (3.1)$$

$$\omega_{pr} = \omega_{pu} + \Delta_{12} \quad (3.2)$$

$$\omega_{pr} = \omega_{pu} + \Delta_{12} - \Delta_1 \quad (3.3)$$

$$\omega_{pr} = \omega_{pu} + \Delta_{12} \quad (3.4)$$

$$\omega_{pr} = \omega_{pu} + \Delta_{12} - \Delta_2 \quad (3.5)$$

$$\omega_{pr} = \omega_{pu} + \Delta_{12} - (\Delta_1 + \Delta_2) \quad (3.6)$$

$$\omega_{pr} = \omega_{pu} - \Delta_3 \quad (3.7)$$

$$\omega_{pr} = \omega_{pu} - (\Delta_2 + \Delta_3) \quad (3.8)$$

$$\omega_{pr} = \omega_{pu} - (\Delta_1 + \Delta_2 + \Delta_3) \quad (3.9)$$

Using these conditions for all the possible transition, we were able to calculate the position of peaks which are in good agreement with the experimental observation as shown in table 3.1. The VSOP peak at $\Delta_{pu} = 0$ is due to overlapping of resonance conditions 3.1 and 3.4.

Since the frequency separation of all excited levels fall well within the Doppler regime of about 500 MHz for ^{87}Rb atoms at room temperature, there is a possibility of having additional peaks not resembling VSOP. This is a consequence of optical pumping via all the unresolved hyperfine levels. The frequency separation of those peaks is equivalent to that of the excited hyperfine states. Corresponding to that, we have observed a peak (labeled as p1 in figure 3.1(b) [82].

The observed results can be best understood by solving the density matrix equations for the six-level system. However, since we are only interested in the qualitative discussion for the observed VSOP peaks, solving the entire matrix equations incorporating all the hyperfine levels is not required. Instead, we can use the rate equations to understand it, as this approach requires solving less number of equations. These equations can be used when various types of coherence that can be possibly generated between the hyperfine levels of the ground state and the excited state can be neglected. One such is the Raman resonance condition, resulting in various sub-Doppler features. However, the experimental regime that we have worked on doesn't allow such resonance conditions to be fulfilled. For our case, both the laser powers are sufficiently low and equal. The populations of the ground state (N) and the excited state (N') can be written as [80]

$$\frac{dn_m}{dt} = -\Gamma n_m - \sum_{\mu=1,k}^N |C_{m\mu}^\epsilon|^2 S_k^\epsilon (n_m - n_\mu) - (\gamma + \Lambda) n_m + \sum_{m'=1, m' \neq m}^{N'} \Lambda_{mm'} n'_m \quad (3.10)$$

$$\frac{dn_\mu}{dt} = \sum_{\mu=1,\epsilon}^{N'} |C_{m\mu}^\epsilon|^2 n_m - \sum_{\mu=1,k}^{N'} |C_{m\mu}^\epsilon|^2 S_k^\epsilon (n_\mu - n_m) - \gamma (n_\mu - n_{\mu,0}) - \Lambda n_\mu + \sum_{\mu'=1, \mu' \neq \mu}^N \Lambda_{\mu'\mu} n'_{\mu'} \quad (3.11)$$

where if the ground and excited level populations add up, they add up to unity. In the equations n_m and n_μ are the populations of the excited state ' m ' and excited state μ , ' C ' terms correspond to the Clebsh-Gordon coefficients and ' s ' terms correspond to the laser intensity. The collision loss rate and the re-pumping rate of the atoms are incorporated by Λ and Γ terms respectively. Solving those equations, the relative magnitude for the absorption peaks can be given by,

$$I_i(\omega) = \sum_{\mu,m}^N |C_{m\mu}^\epsilon|^2 (n_\mu - n_m) \frac{\exp[-Mv_i^2/2k_Bt] 0.5\Gamma}{(\omega - \omega_{m,\mu} - kv_i)^2 + (0.5\Gamma)^2} \quad (3.12)$$

where ϵ denotes the polarization of the laser beam, M denotes the mass and $\omega_{m,\mu}$ is angular resonance frequency. The difference in the amplitude of the VSOP peaks will be determined by this term. The absorption magnitude for each absorption peak is the difference in the absorption seen by the laser beam in the absence and presence of the other beam. In our case, this is the difference in the absorption seen by the locked probe laser beam in the absence or presence of a pump beam. The solution using equation 3.12 for the case when probe laser is locked from

$F = 2 \rightarrow F' = 2$ transition is shown in figure 3.2. The obtained spectrum is in good agreement with the experimentally recorded data.

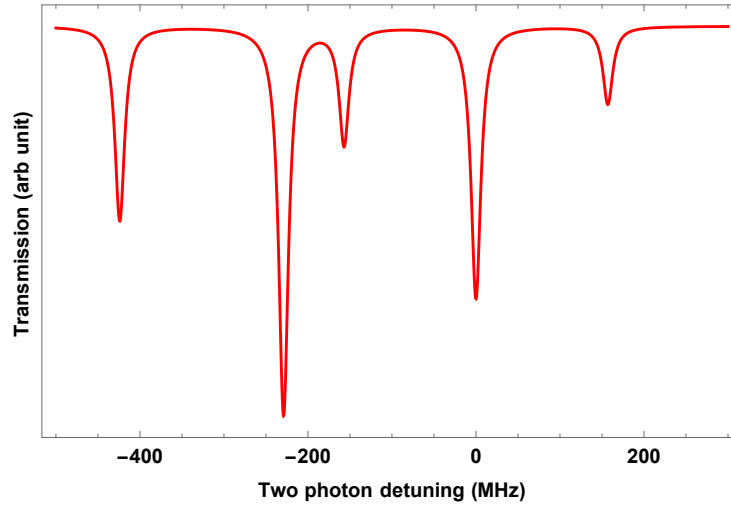


FIGURE 3.2: Numerically obtained VSOP peaks for the probe locked at transition $F = 2 \rightarrow F' = 2$.

3.2.2 VSOP spectrum for different lock positions of the probe field

In the previous section, we illustrated the VSOP spectrum for the probe field locked at $F = 2 \rightarrow F' = 2$. In this section, we look into the changes in the spectra for the probe field locked at different allowed transitions. In the figure 3.3, a_1 , a_2 and a_3 represent VSOP spectrum for probe field locked at $F = 1 \rightarrow F' = 2$, $F = 1 \rightarrow F' = 1$ and $F = 1 \rightarrow F' = 0$ respectively. The power of the pump and probe beams were fixed at 0.02 mW. Similarly, b_1 , b_2 and b_3 represent $F = 2 \rightarrow F' = 3$, $F = 2 \rightarrow F' = 2$ and $F = 2 \rightarrow F' = 1$ respectively. In all the spectrum except for b_1 and b_2 , we observe five VSOP peaks with varying amplitude and position. If we consider the case of a pure three-level system, only one broad VSOP peak will be observed. By changing the lock position from $F' = 2(a_1) \rightarrow F' = 1(a_2)$, the whole spectrum shifts by 157 MHz. As expected, this shift corresponds to the energy difference between $F' = 2$ and $F' = 1$. Similarly, (a_3) is shifted by 72 MHz as compared to (a_2). The same is also observed for the case of $F' = 2 \rightarrow F' = 1, 2, 3$. We have observed that at all lock points, the spectrum characteristics are unaltered.

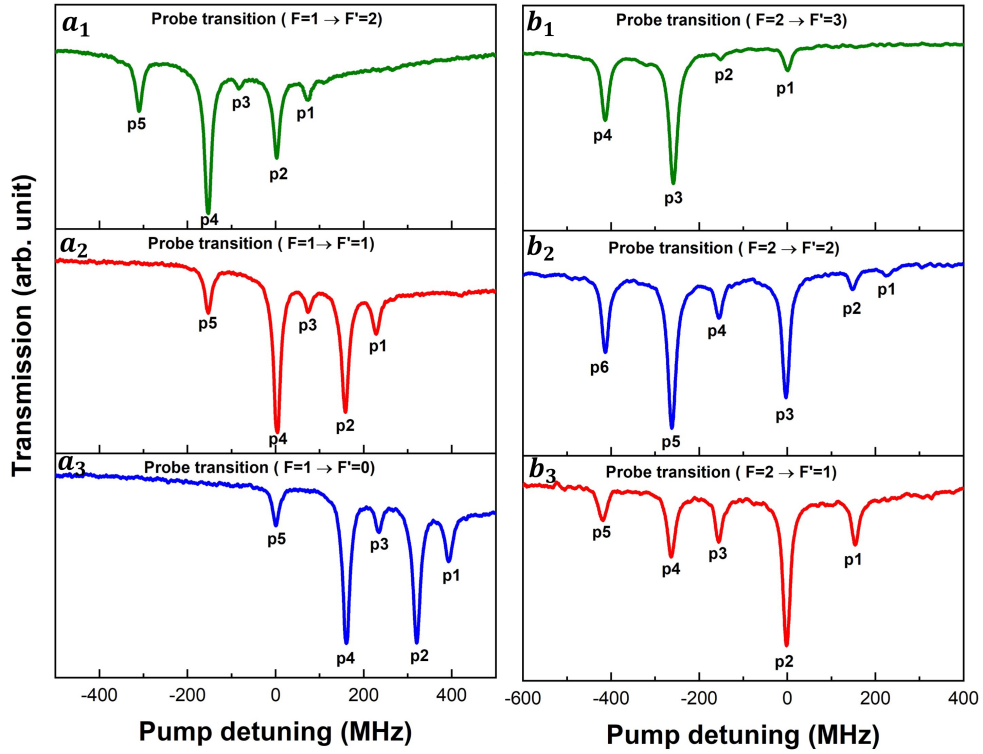


FIGURE 3.3: VSOP peaks for probe locked at different transitions

TABLE 3.2: The relative position of VSOP peak's when the probe laser is locked from $F=2$ to $F'=1$ transition

Peak label	Calculated value(MHz)	Measured value (MHz)
p1	$\Delta_2=157$	154
p2	0	0
p3	$-\Delta_2=-157$	-155
p4	$-\Delta_3=-267$	-263
p5	$-(\Delta_2+\Delta_2)=-424$	-421

TABLE 3.3: The relative position of VSOP peak's when the probe laser is locked from $F=2$ to $F'=3$ transition

Peak label	Calculated value (MHz)	Measured value (MHz)
p1	0	0
p2	$-\Delta_2=-157$	-154
p3	$-\Delta_3=-267$	-262
p4	$-(\Delta_1+\Delta_3)=-339$	-327
p5	$-(\Delta_2+\Delta_2)=-424$	-417

TABLE 3.4: The relative position of VSOP peak's when the probe laser is locked from F=1 to F'=0 transition

Peak label	Calculated value (MHz)	Measured value (MHz)
p1	$(\Delta_1+2\Delta_2)=386$	394
p2	$(\Delta_1+2\Delta_3)=339$	325
p3	$(\Delta_1+2\Delta_2)=229$	-228
p4	$\Delta_2=157$	160
p5	0	0

TABLE 3.5: The relative position of VSOP peak's when the probe laser is locked from F=1 to F'=1 transition

Peak label	Calculated value (MHz)	Measured value (MHz)
p1	$(\Delta_1+\Delta_2)=229$	227
p2	$\Delta_2=157$	159
p3	$\Delta_1=72$	74
p4	0	0
p5	$-\Delta_2=157$	-154

TABLE 3.6: The relative position of VSOP peak's when the probe laser is locked from F=1 to F'=2 transition

Peak label	Calculated value (MHz)	Measured value (MHz)
p1	$\Delta_1=72$	73
p2	0	0
p3	$-\Delta_1=72$	79
p4	$-\Delta_2=157$	-155
p5	$-2\Delta_2=314$	-311

3.2.3 Effect of pump intensity

The probe and pump power used for experimental measurement of the VSOP peaks as shown in the previous section is 0.02 mW. Both the lasers are kept at equal power selected in such a way that the strength of the VSOP peaks is maximum. We have observed multiple VSOP peaks (depending upon the number of available states for the formation of VSOP) with unequal amplitudes for the case when the probe laser is locked either F=1 to F'=2 or F=2 to F'=2 transition. We have kept the power low to minimize the power-broadening effects. In figure 3.4 we have varied the pump power from 0.03 mW to 1.0 mW with a fixed probe power of 0.02 mW. For case (a), the probe laser is locked from F=1 ground state and for case (b), it is locked from F=2 ground state. In either case, we see that with the increase in the pump power, the amplitude of

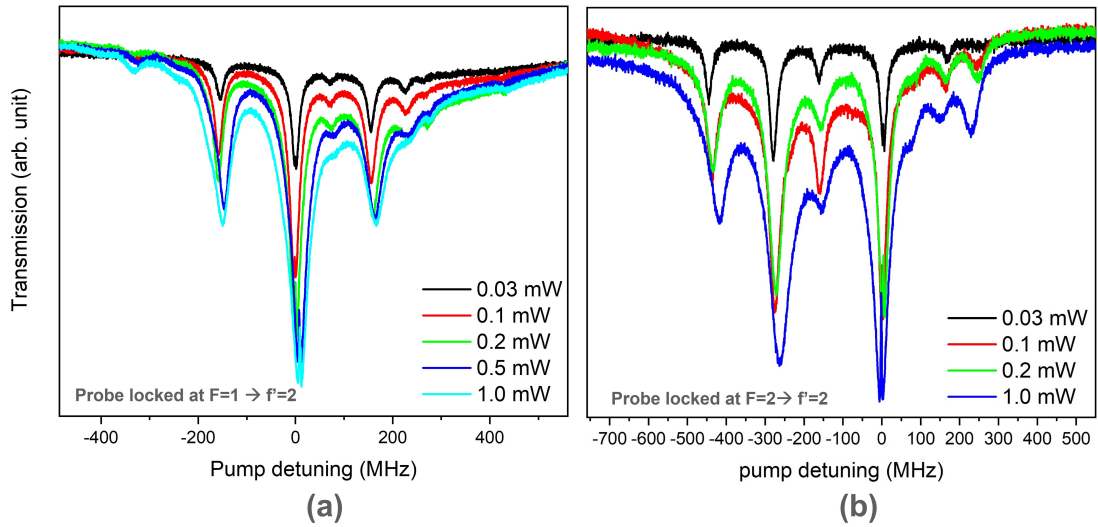


FIGURE 3.4: VSOP peaks for the pump locked at $F = 2 \rightarrow F' = 2$ and the probe is scanning from $F = 1 \rightarrow F' = (0, 1, 2)$

the VSOP peak increases, and the peaks are strengthened due to the increased optical pump rate. The amplitude of the VSOP peak is strongest for the case where the probe laser is locked, this is because more atoms are available for that particular lock point and hence the higher optical pumping rate. Likewise, the weakest peaks are seen for the case where the number of velocity selective classes of atoms is least. In addition to that, we have also observed a significant increase in the linewidth of the VSOP peaks with the increase in the laser power. This is attributed to the power broadening. **In addition we also observe the shift in the position of the peaks. This shift is attributed to the light shift induced by the strong pump[83–85]. A narrow transmission window is also observed within the broad VSOP peak for the lock transition frequency in both cases (a and b). This enhanced transmission is appearing within the VSOP peak because of the formation of Λ system which give rise to the EIT. With the increase in pump power the amplitude of this peak increases as the system reaches a regime where a strong and narrow EIT is expected.** Figure 3.5 is the case when the pump power is 3.5 mW, we observe a narrow transparency peak within one of the VSOP peaks, along with that we observe two other VSOP peaks at +157 and -157 MHz from the locked transition frequency. For this pump power, the other peaks either have very small amplitudes or vanish completely. This is because of saturation effects[86, 87] which occurs when the laser power is above saturation intensity which

is 2.57 mW/cm^2 for the ^{87}Rb D_2 line. **The ultra narrow width of EIT peak reveals the sub-Doppler feature of it [88]. The reduction in width of the EIT peak is due to the contribution of different velocity classes of atoms in the system at room temperature [89].**

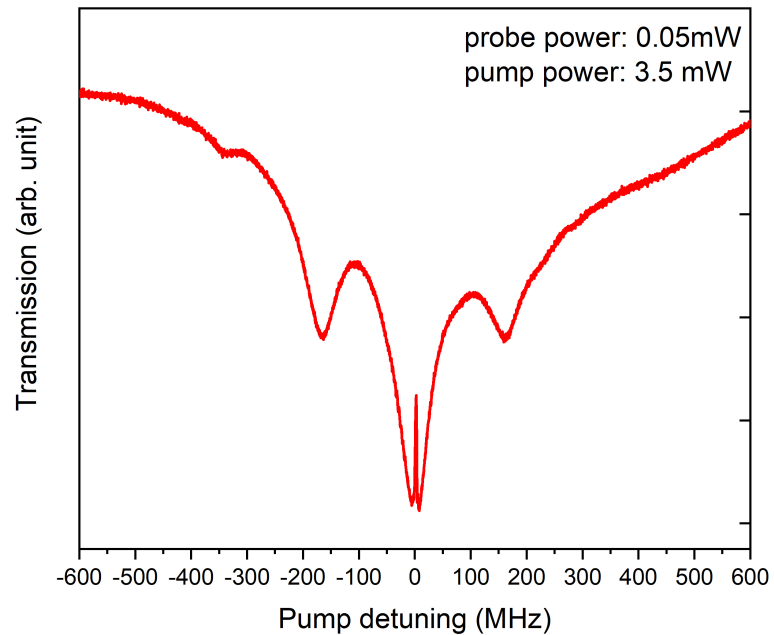


FIGURE 3.5: VSOP peaks for the pump locked at $F = 2 \rightarrow F' = 2$ and the probe is scanning from $F = 1 \rightarrow F' = (0, 1, 2)$

Chapter 4

Electromagnetically Induced Transparency

4.1 Introduction

Various electromagnetically induced phenomena are possible in atomic systems where two laser beams connect the two different ground levels to common excited levels. As discussed in chapter 3, keeping one laser locked (detuned from resonance transition), VSOPs are possible for the group of atoms which are having non-zero velocities. For the condition, when the frequency difference between the lasers exactly matches the energy difference between the two involved ground levels a two-photon resonance is achieved. The VSOP absorption observed at this condition contains a transmission dip. Harris *et al.* in [90] first predicted this process which they later termed it as EIT in [37]. It is a process where a weak probe laser at resonance passing through an atomic medium in presence of the strong laser sees narrow transmission instead of absorption [38, 91]. It is a coherent phenomenon rather than a saturation or a hole burning. The population manipulation of the ground states due to the presence of a strong pump field and a weak probe field leads to destructive interference. The population that is trapped in one of the ground states results in the formation of a dark state which results in transparency. For the first time Boller *et al.* in [52] experimentally demonstrated the presence of EIT in strontium vapor. Kasapi *et al.* in [92] studied temporal and spatial dynamics of the pulses propagating in an EIT medium. They reported a slowing of pulse velocity. For weak probe and strong pump, they observed the group

velocity of the pulse to be as slow as $c/165$. The energy transmission was observed to be 55% of the incident pulse energy. Ideal transparency is attained only if the frequency precisely matches the two-photon resonance condition. However, it is not always possible to create an ideal situation like this. To compensate for the slight mismatch of the frequency difference stronger pump field can be used so that the interference becomes robust [93]. **Therefore, as discussed previously EIT plays an important role specially in the slow light experiments [88, 94].** It has been studied in three basic configurations viz. Λ , V and Ladder [53, 87, 95, 96]. Our experimental results and discussions shall remain limited to Λ configuration only since this doesn't require two lasers of different frequencies as for the case of the Ladder system. Secondly, the linewidth of the EIT peak would be much narrower compared to that produced in the V system. The linewidth, lineshape and amplitude of EIT can be controlled by various parameters such as the laser intensity [86, 97], angle between the two lasers [98], atomic density in vapor cell [76, 99, 100] and polarization of laser [101]. The polarization of the laser beam in the vapor frame can be manipulated by exposing it to an external magnetic field [102–104]. The study of EIT in presence of the magnetic field has attracted a lot of interest in the field of quantum optics since it opens the possibility for generating multiple EIT sub-windows. The number of possible EIT sub-windows depends on the number of states that are available for the formation of various Λ sub-systems after degeneracy is uplifted. In addition, it also depends upon the polarization of light which is determined by the orientation of the applied magnetic field in the direction of the electric field of the two lasers. For $^{87}\text{Rb D}_2$, we can obtain three or four EIT peaks depending on the orientation of the magnetic field which is discussed in detail in the next section of this chapter. The three-level model [105] (three energy states and two lasers) which is designed to explain the EIT phenomena may not be sufficient [106] for the process in presence of the magnetic field. This is mainly because of the two factors. Firstly, in the presence of multiple Zeeman sublevels, the isolated three-level system is not possible. Secondly, for $^{87}\text{Rb D}_2$ line the Zeeman sublevels belonging to the nearby hyperfine states (lying within the Doppler regime) cannot be ignored. The effect of other sublevels belonging to neighboring states manifests in their participation in the population dynamics. This is investigated in detail by Sargsyan et.al. [107]. Because of this, a strong asymmetry in the EIT profile is observed [108–110]. The asymmetry [111] can be explained by including all hyperfine

states, or more precisely by including those excited states that can simultaneously couple both ground states. To some extent, it is incorporated in double Λ systems, which have two ground states and two excited states, as described in [112, 113]. Additionally, the role of the off-resonant velocity class on the EIT profile becomes important.

In this chapter, we have discussed the results obtained by exposing the atomic vapor to the external magnetic field. We have investigated in detail the effects of closeby states for two different sets of polarisations of lasers. And, have discussed in detail the origin of asymmetry in the EIT profile. In this process, we have been able to identify the condition for which the asymmetry in the lineshape would be absent. To explain our observation, we have used a double Λ system model.

4.2 Experimental Layout

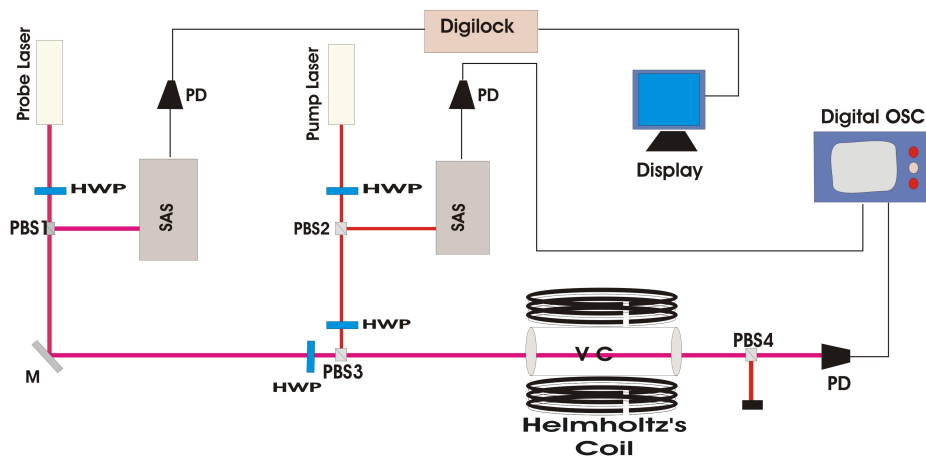


FIGURE 4.1: Schematic of the experimental setup. PD - Photodiode, M - 99.9% reflective mirror, PBS - Polarising beam splitter, HWP - Half-wave plate.

The schematic of the experimental setup is shown in figure 4.1. Both the lasers, the probe and the pump, are derived from two different sources and are tuned to ^{87}Rb D_2 line using the SAS technique. **In an atomic vapor system, for a Λ system the collisional dephasing rate of the ground**

state coherence is always present which is of the order of few KHz[114]. It is well known that any fluctuations in the phase of two lasers also leads to the dephasing of the ground state coherence. However, this dephasing rate due to phase mismatch between lasers is very small ($< \text{Hz}$) [115] as compared to the collisional dephasing term and can be neglected. Also in our case, experiment is performed using continuous wave (CW) lasers and the steady state behavior of the system is being observed. In this scenario the formation of a dark state (and hence the existence of EIT) is independent of the phases of lasers unless the system is a closed loop type [116]. This allows us to use two independent lasers without drastically modifying the performance of EIT. Systems that are investigated in thesis are not closed loop type and the only necessary condition for the formation of EIT is two photon resonance. This is achieved by matching the frequency difference between the lasers with the frequency gap between the ground states.

For all the experimental measurements, the probe laser is kept in locked mode and the pump is scanned across all the states. Performing the experiments with locked probe laser limits the interaction of the beam with zero velocity atoms because of which the Doppler broadening in the obtained spectra is reduced [61, 117]. Both the lasers are in co-propagating geometry and therefore the two-photon resonance condition is independent of velocity classes. The spot size ($\frac{1}{e^2}$) of both the lasers are nearly equal and is approximately 0.2 cm which is measured using the conventional knife-edge technique. The orthogonality of both the lasers is maintained throughout the experiment which is ensured using PBS (Polarizing beam splitter). Both the lasers are overlapped using PBS and then passed through the Rb vapor cell. The cell is 5 cm long with a diameter of 3 cm having an anti-reflective coated window that minimizes the back reflection. The crossing angle of both lasers is kept minimum to maximize the interaction zone of both the lasers with the atoms inside the vapor cell. The cell is filled with both the isotopes of Rb atoms and is maintained throughout the experiments at room temperature. The output power of both the lasers is controlled using a pair of HWP (Half wave plate) and PBS. Throughout the experiment, the probe power is kept fixed at 1 mW and the pump at 4.5 mW, unless stated otherwise. The power is measured with a power meter(coherent-109813) with the least count error of $0.01 \mu\text{W}$. The magnetic field is generated using pair of Helmholtz coils having a diameter of 16 cm and

a resistance of 10Ω . The magnetic field is varied by using an external DC power supply. In experiment, the magnetic field is varied upto 50 G, beyond which the level crossing will effect the measurements [118, 119]. For obtaining a longitudinal magnetic field, the orientation of the two coils is changed. Another PBS is used after the vapor cell, which separates both beams. The probe laser is then passed through a photodiode which has a variable gain with a responsivity of 0.6 V/A at 800 nm having linear variation from 0 to -11 V. The time scale of the data recorded in an oscilloscope is calibrated and transformed to frequency scale by using the corresponding SAS signal.

4.3 EIT in three level Λ system in absence of magnetic field

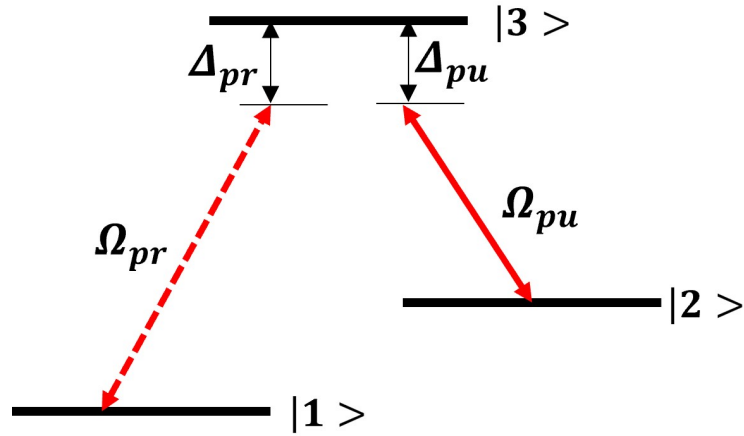


FIGURE 4.2: Energy level diagram for the three-level system in absence of magnetic field.

In this section, we discuss the results observed in absence of a magnetic field with the experimental setup as described in the above section. In our experiment, we have locked the probe laser at $|F = 2\rangle \rightarrow |F' = 2\rangle$ transition; the pump laser is kept scanning from ground state $|F = 2\rangle$. With this configuration, a Λ system is formed comprising of $|F = 1\rangle$, $|F = 2\rangle$ and $|F' = 2\rangle$. The energy level diagram is shown in figure 4.2. The EIT peak is expected at a frequency where Raman resonance condition is fulfilled i.e. $\Delta_{pu} - \Delta_{pr} = 0$, where Δ_{pu} is the detuning of the pump laser from the resonant frequency and Δ_{pr} is for the probe laser.

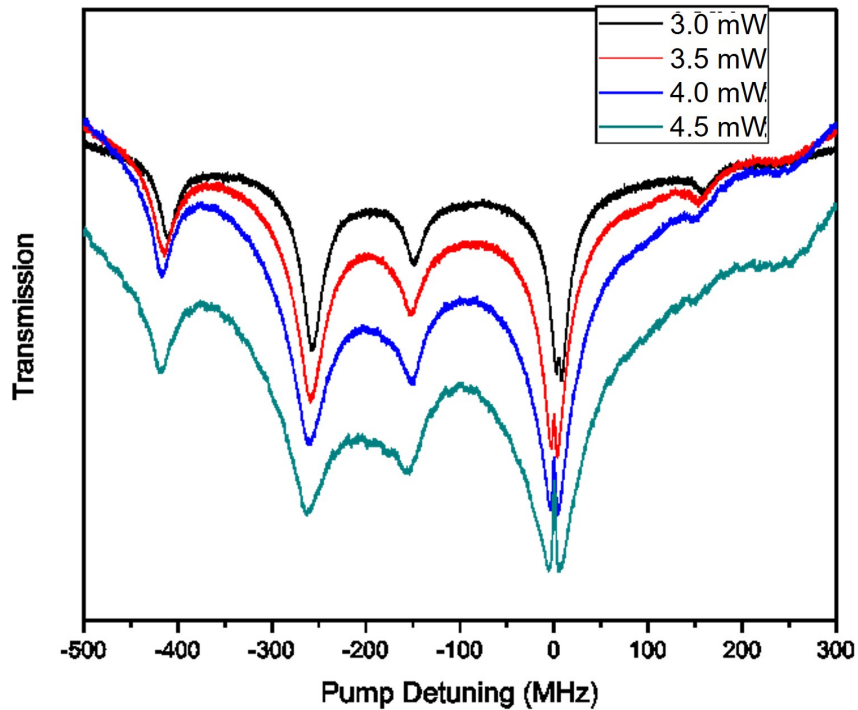


FIGURE 4.3: EIT for different pump intensity in absence of magnetic field. The probe power is fixed at 1.0 mW and the pump is varied from 3.0 to 4.5 mW.

figure 4.3 shows the spectra recorded by varying the pump power. Spectra contains various VSOP peaks appearing because of the thermal velocity of atoms as discussed in the previous section. The VSOP at a pump detuning of $\Delta_{pu}=0$ MHz contains an EIT peak. Though the narrowest recorded linewidth of EIT resonance in the atomic vapor is ~ 30 Hz, in our experimental condition, the linewidth of the EIT observed is 4.5 MHz. This can be attributed to the power and linewidth of the pump laser which are 4.5 mW and 1 MHz respectively. As we increase the power, the linewidth increases although minimal reflecting the effect of power broadening. The amplitude has also seen a substantial modification. In [38], more information on the linewidth and amplitude of EIT resonances in the absence of a magnetic field can be found. Our experiment has been performed in the $^{87}\text{Rb } D_2$ line in which the separation between the hyperfine excited states lies well within the Doppler width at room temperature. As a result, the presence of hyperfine states can cause some asymmetry in the EIT lineshape, as detailed in [120]. But the influence would be negligible and the system can be considered a pure three-level Λ system. However, in the presence of a magnetic field, the population redistributes within the Zeeman sublevels and multiple peaks can be seen. The overall dynamics, however, are unchanged, but the impact of

other hyperfine levels on particular laser configurations becomes more pronounced, which will be discussed in the following sections.

4.4 EIT in presence of magnetic field

In the absence of the magnetic field, $B = 0$, Λ scheme formed by hyperfine states results in a single EIT, the amplitude and linewidth of which depend on various factors such as the ground state coherence, population density, Rabi frequency of both the lasers and decay rate of the excited state. With the magnetic field, some of these parameters can be controlled and EIT lineshape can be modulated. This would be of many applications in the field of quantum optics. When an external magnetic field is applied, the hyperfine level with quantum number F is split into $2F+1$ magnetic sub-levels denoted by magnetic quantum number m_F . As a result, the single Λ configuration formed by three hyperfine states is split into multiple Λ configurations. The number of possible Λ configurations depends on the polarization of lasers and the number of available magnetic sub-levels. The presence of the external magnetic field redefines the polarization state of both the laser fields. When the direction of the applied magnetic field is perpendicular to the electric field vector of the laser field, it is viewed as circularly polarized, otherwise linearly polarized. The direction vector is shown in figure 4.4. We have carried out our experiment in two cases of magnetic field orientation i.e transverse and longitudinal.

4.4.1 EIT in transverse magnetic field

In this experiment, the orientation of the applied magnetic field is kept perpendicular to the propagation of the laser. Being orthogonal to each other, the electric field of the pump beam is parallel and the probe beam is perpendicular to the applied magnetic field. As a result, in the atomic frame of reference, the pump field is π polarised and the probe field is σ polarised. The probe is locked from $|F = 1\rangle \rightarrow |F' = 2\rangle$ transition and the pump is scanned from $|F = 2\rangle$ ground state. Throughout the experiment, the pump power is kept fixed at 4.5 mW and the probe

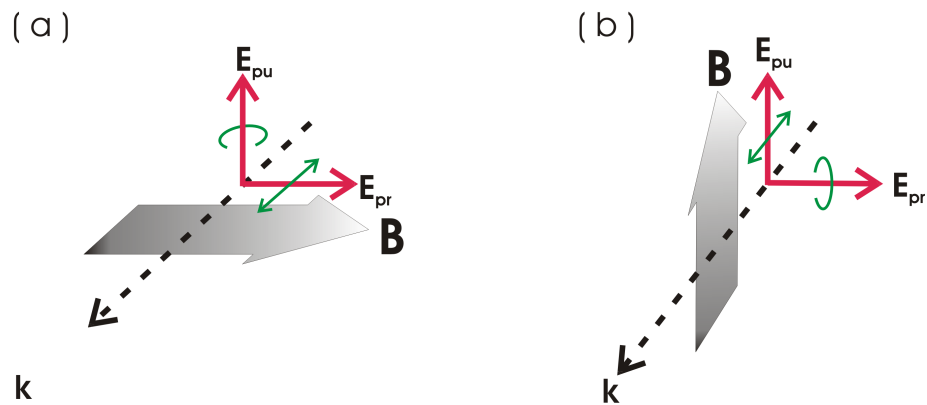


FIGURE 4.4: E_{pu} and E_{pr} represent electric polarization of pump and probe field respectively, k represents propagation direction of laser and B is magnetic field direction. In (a) E_{pu} and B are perpendicular to each other and in (b) parallel. E_{pr} is perpendicular to E_{pu} .

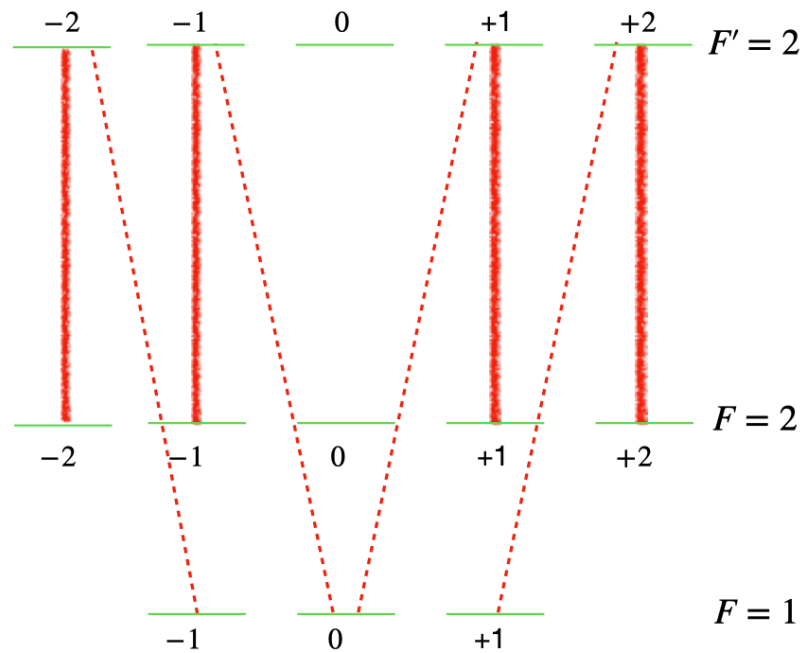


FIGURE 4.5: Level diagram for illustration of possible Λ configurations. The solid lines in the level diagram show transition corresponding to π -polarised pump field and the dashed line corresponds to σ -polarised probe field.

at 1 mW. The experiment has been carried out at a different value of applied magnetic field varied from 0 to 50 G. The results recorded are shown in figure 4.6 (a), (b), and (c). In this configuration, there are four possible Λ configurations formed by the allowed transition between Zeeman sublevels as shown in figure 4.5. As a result we have observed four peaks labelled as A ($\Delta_{pu} = -3\Delta_B$), B ($\Delta_{pu} = -\Delta_B$), C ($\Delta_{pu} = +\Delta_B$) and D ($\Delta_{pu} = +3\Delta_B$), where Δ_B is given by

$$\Delta_B = \frac{\mu_B g_F m_F B}{\hbar}$$

where μ_B is Bohr's magneton, g_f is Lande's g-factor, m_f is the quantum number of the Zeeman sublevel and B is the applied magnetic field. In the presence of the magnetic field, the peak appearing at $\Delta_{pu} = 0$ MHz completely diminishes and is replaced by all the above four peaks. The sub-systems formed by involving the Zeeman sublevels and responsible for EIT are as follows:

(A). EIT resonance at $\Delta_{pu} = -3\Delta_B$ due to;

$$1. |F = 1; m_F = -1\rangle \longleftrightarrow |F' = 2; m_{F'} = -2\rangle \longleftrightarrow |F = 2; m_F = -2\rangle$$

(B). EIT resonance at $\Delta_{pu} = -\Delta_B$ due to;

$$1. |F = 1; m_F = 0\rangle \longleftrightarrow |F' = 2; m_{F'} = +1\rangle \longleftrightarrow |F = 2; m_F = +1\rangle$$

(C). EIT resonance at $\Delta_{pu} = +\Delta_B$ due to;

$$1. |F = 1; m_F = 0\rangle \longleftrightarrow |F' = 2; m_{F'} = -1\rangle \longleftrightarrow |F = 2; m_F = -1\rangle$$

(D). EIT resonance at $\Delta_{pu} = +3\Delta_B$ is due to;

$$1. |F = 1; m_F = +1\rangle \longleftrightarrow |F' = 2; m_{F'} = +2\rangle \longleftrightarrow |F = 2; m_F = +2\rangle$$

All the peak positions with the levels involved in it are summarized in table 4.1.

As shown in figure 4.6 (d), the separation between two consecutive peaks varies linearly with the increase in the magnetic field. And the separation between two adjacent EIT resonances is found

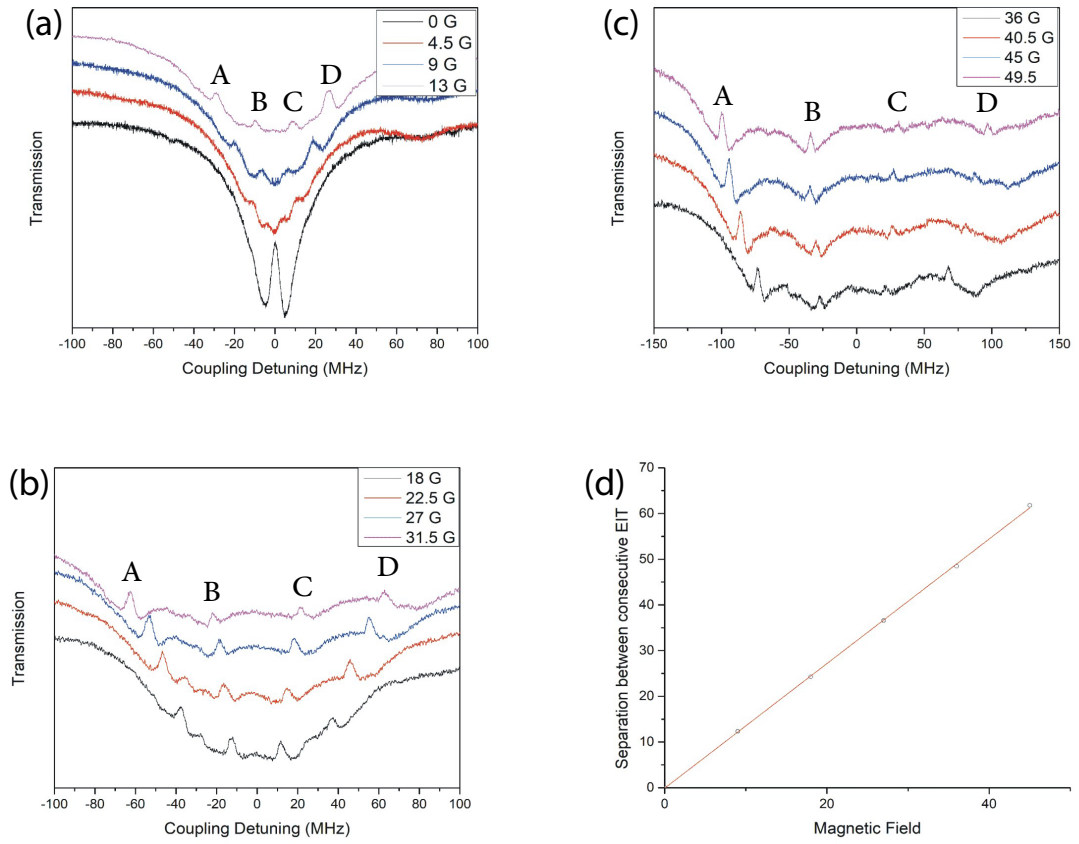


FIGURE 4.6: The splitting of EIT resonance due to the externally applied transverse magnetic field. For case (a), the magnetic field is varied from 0 G to 13 G; for case (b) from 18 G to 32 G; and for case (c) from 32 G to 50 G.

TABLE 4.1: EIT position corresponding to each Λ in the presence of transverse magnetic field corresponding to figure 4.5

Sl. No.	Zeeman sublevels involved in Λ system			EIT Positions
	$F=1; m_F$	$F=2; m_{F'}$	$F'=2; m_F$	
i	-1	-2	-2	$-3\Delta_B$
ii	0	-1	-1	$-\Delta_B$
iii	0	+1	+1	$+\Delta_B$
vi	+1	+2	+2	$+3\Delta_B$

to be $2\Delta_B$. As shown in figure 4.6 (a), with increase in the magnetic field the single peak splits into four equal peaks in terms of amplitude. Although, the amplitude of peaks formed is smaller as compared to the peak formed for 0 G. For the magnetic field till 18G the relative variation in the amplitude of peaks is negligible. Beyond 18 G (figure 4.6 (c)), the amplitude of peaks A and B starts dominating over C and D. As we reach 30 G the amplitude of peak A becomes the highest of all. This is because in the presence of the magnetic field the population redistributes over all the Zeeman sublevels. The redistribution of population depends on the constants (c_{ij})s, which is defined as [121],

$$c(F', m_{F'}; F, m_F; q) = (-1)^{1+I+J'+F'+F-m_{F'}} \times \sqrt{2J'+1} \sqrt{2F'+1} \sqrt{2F+1} \times \begin{pmatrix} F' & 1 & F \\ -m_{F'} & q & m_F \end{pmatrix} \begin{Bmatrix} F' & 1 & F \\ J & I & J' \end{Bmatrix} \quad (4.1)$$

expressed in terms of Wigner-3j (parenthesis) and Wigner-6j (curly brackets) symbol, the square of this terms defines the transition strength. The components of this dipole matrix also indicates the strength of the interaction between atoms and nearly-resonant optical light [122]. This transition strength along with the detuning (varies with magnetic field) plays a decisive role in redistribution of population within the Zeeman sublevels.

Further, we investigate the same system by interchanging the polarisation of pump and probe. The polarisation of the probe laser is changed from σ to π and pump laser is changed from π to σ in atomic frame of reference. The energy level diagram involving all the magnetic sublevels are shown in figure 4.7. The sub-systems formed by involving the Zeeman sublevels and responsible for EIT are as follows:

Resonance at $\Delta_{pu} = -3\Delta_B$ is due to

$$1. |F = 1; m_F = -1\rangle \longleftrightarrow |F' = 2; m_{F'} = -1\rangle \longleftrightarrow |F = 2; m_F = -2\rangle$$

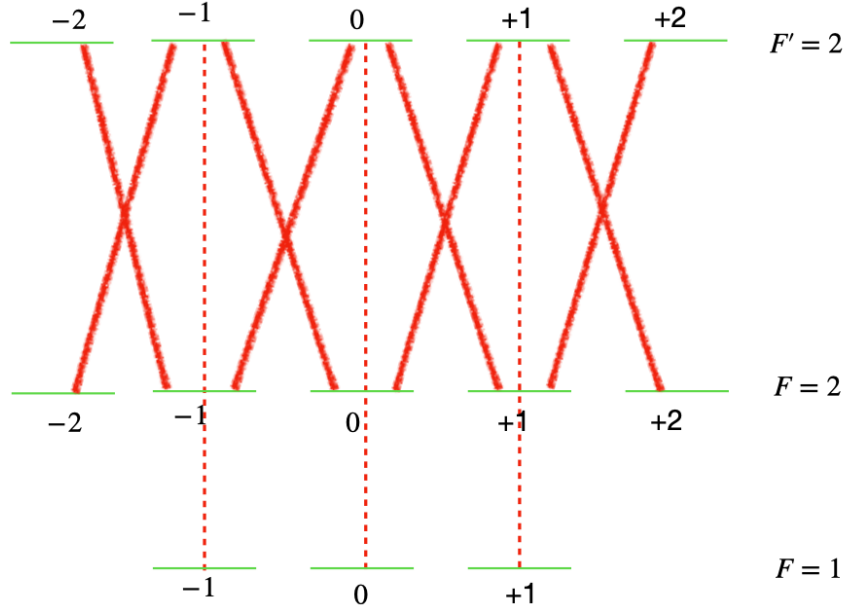


FIGURE 4.7: Level diagram for illustration of possible Λ configurations. The solid lines in the level diagram show transition corresponding to the σ -polarised pump field and the dashed line corresponds to the π -polarised probe field.

Resonance at $+3\Delta_B$ is due to

1. $|F = 1; m_F = +1\rangle \longleftrightarrow |F' = 2; m_{F'} = +1\rangle \longleftrightarrow |F = 2; m_F = +2\rangle$

EIT resonance at $\Delta_{pu} = +\Delta_B$ is as a result of the following Λ configurations having congruent two photon detuning condition;

1. $|F = 1; m_F = +1\rangle \longleftrightarrow |F' = 2; m_{F'} = +1\rangle \longleftrightarrow |F = 2; m_F = 0\rangle$

2. $|F = 1; m_F = 0\rangle \longleftrightarrow |F' = 2; m_{F'} = 0\rangle \longleftrightarrow |F = 2; m_F = +1\rangle$

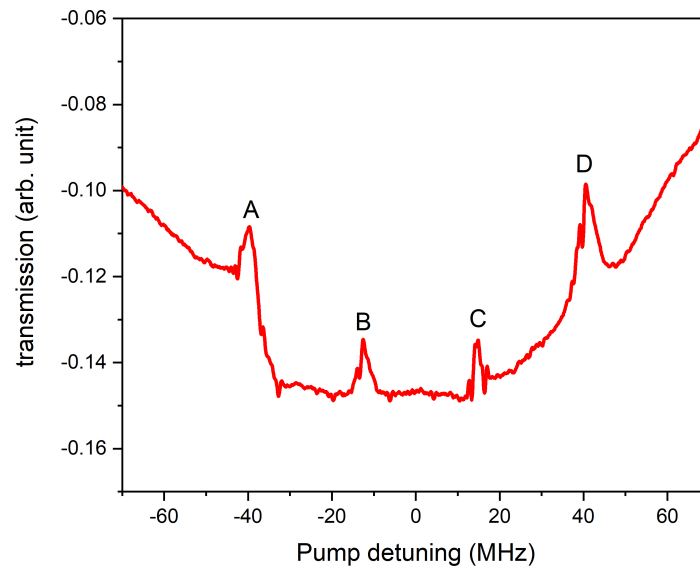
Similarly, EIT resonance at $\Delta_{pu} = -\Delta_B$ is as a result of two Λ configurations having congruent two photon detuning condition;

1. $|F = 1; m_F = -1\rangle \longleftrightarrow |F' = 2; m_{F'} = -1\rangle \longleftrightarrow |F = 2; m_F = 0\rangle$

2. $|F = 1; m_F = 0\rangle \longleftrightarrow |F' = 2; m_{F'} = 0\rangle \longleftrightarrow |F = 2; m_F = -1\rangle$

TABLE 4.2: EIT position corresponding to each Λ in presence of transverse magnetic field corresponding to figure 4.7

Sl. No.	Zeeman sublevels involved in Λ system			EIT Positions
	$F=1; m_F$	$F'=1; m_{F'}$	$F=1; m_F$	
i	+1	+1	+2	$-3\Delta_B$
ii	+1	+1	0	$-\Delta_B$
iii	0	0	+1	$-\Delta_B$
iv	0	0	-1	$+\Delta_B$
v	-1	-1	0	$+\Delta_B$
vi	-1	-1	-2	$+3\Delta_B$

FIGURE 4.8: Splitting of EIT resonance with probe π polarised and pump σ polarised. The applied magnetic field is 22 G.

All the peak positions along with the levels involved in it are itemized in table 4.2

The probe transmission for this configuration is shown in figure 4.8. We have observed four EIT peaks at four different positions. The positions of the peaks match the expected value. It can also be seen that the amplitude of B and C is less compared to C and D. This is because multiple Λ systems are involved in the formation of peaks B and C. The imperfect overlapping of these systems can reduce the amplitude of EIT peaks which we will discuss in detail in the next section.

4.5 The effect of nearby hyperfine states

As we discussed in the previous section that in the presence of an external magnetic field one can have multiple closeby spaced EIT peaks. While discussing the results in the previous section, the effects of closeby state were not taken into account. But at a higher magnetic field and low probe and pump laser power of 0.3 mW and 3.5 mW, the Zeeman sublevels of closeby hyperfine states will start participating and cannot be ignored. The participation becomes evident by the appearance of asymmetry in the EIT profile recorded at a high magnetic field. In this section, we systematically investigate the occurrence of asymmetry and formulate the conditions under which the effect of closeby states manifests

4.5.1 Asymmetry in EIT due to strong magnetic field

To understand and study the asymmetry in EIT lineshape with a strong magnetic field we consider Λ system involving hyperfine states $F=1$, $F'=2$, and $F=2$. Depending on which transition probe is locked the given Λ system results in two different configurations as shown in figure 4.9. The two configurations are labeled as Λ_1 in which the probe laser is locked from $F=1$ to $F'=2$ transitions and for Λ_2 the probe is locked from $F=2$ to $F'=2$ transition. For the measurement, we have only considered the case of the transverse magnetic field. Throughout the experiment, the pump power is kept fixed at 3.5 mW and the probe power at 0.3 mW unless it is stated otherwise.

The probe transmission recorded for this configuration for different values of the magnetic field is shown in figure 4.10 (a). At a magnetic field of 0 G, we observe a single peak as seen in the earlier section. On increasing the magnetic field to 9 G we observed four well-resolved peaks labeled as A_1 , A_2 , A_3 , and A_4 . For this configuration, we have already discussed the peak position in the previous configuration. For completeness, the position of peak A_1 is at $-3\Delta_B$, A_2 at $-\Delta_B$, A_3 at $+\Delta_B$ and A_4 at $+3\Delta_B$. On increasing the magnetic field further to 25 G, we observed the signature of asymmetry on peak A_2 and A_3 . As we increase the magnetic field further, the peak A_3 converts completely into absorption. To resolve this further, we recorded the spectra

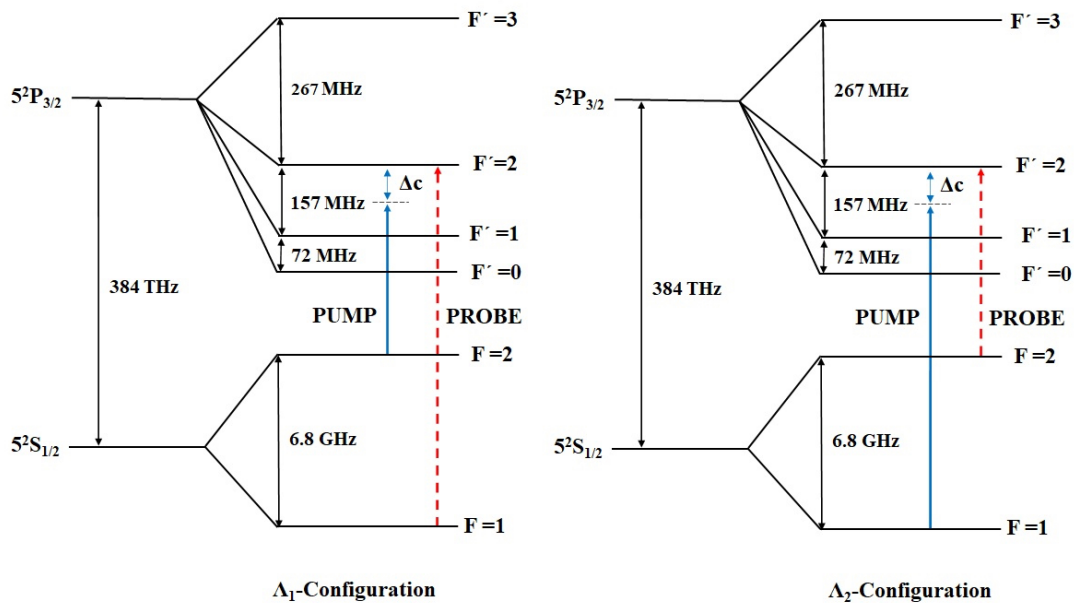


FIGURE 4.9: Λ configurations in ^{87}Rb D_2 line for probe transition locked at $F' = 1 \rightarrow F' = 2$ and $F = 2 \rightarrow F' = 2$. The blue solid line indicates Pump transition and the red dashed line indicates probe transition.

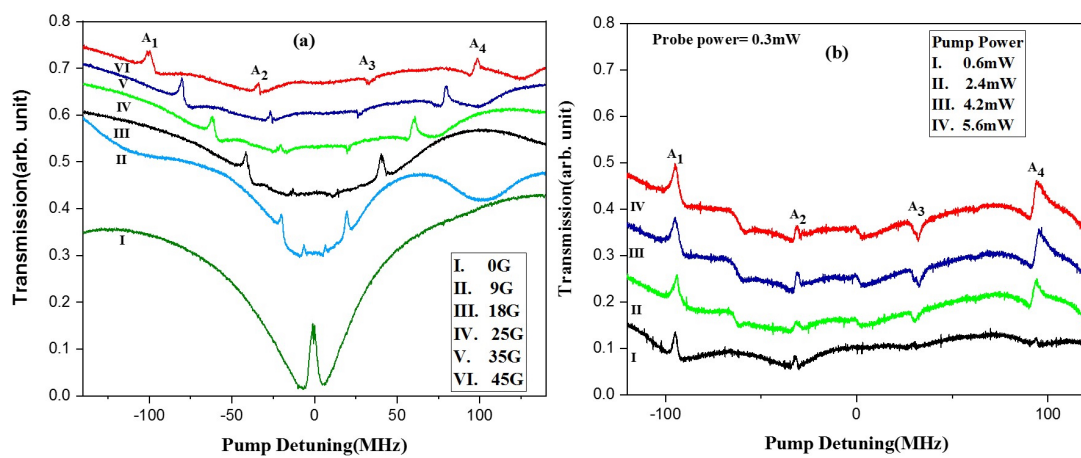


FIGURE 4.10: Experimental results for Λ_1 configuration, (a). for different values of magnetic field at $P_{pu} = 3.5\text{mW}$ and $P_{pr} = 0.3\text{mW}$, (b) for increasing pump power at $B = 40\text{G}$.

TABLE 4.3: EIT positions corresponding to each Λ system for Λ_1 configuration.

Sl. No.	Zeeman sublevels involved in Λ system				EIT Positions
	$F=1; m_F$	$F=2; m_F$	$F'=1; m_F$	$F'=2; m_F$	
i	+1	+2	-	+2	$+3\Delta_B$
ii	0	+1	-	+1	$+\Delta_B$
iii	0	-1	-	-1	$-\Delta_B$
iv	-1	-2	-	-2	$-3\Delta_B$
v	+1	0	0	-	$+\Delta_B$
vi	-1	0	0	-	$-\Delta_B$
vii	0	+1	+1	-	$+\Delta_B$
viii	0	-1	-1	-	$-\Delta_B$

by increasing the pump power at a fixed value of the magnetic field of 40 G as shown in figure 4.10 (b). The presence of asymmetry becomes prominent for a higher value of pump power. The reason behind the asymmetry can be attributed to the presence of neighboring state $F'=1$. Other neighboring states can be ignored as they don't fulfill the selection rule. The energy level by including the $F'=1$ level is shown in figure 4.11

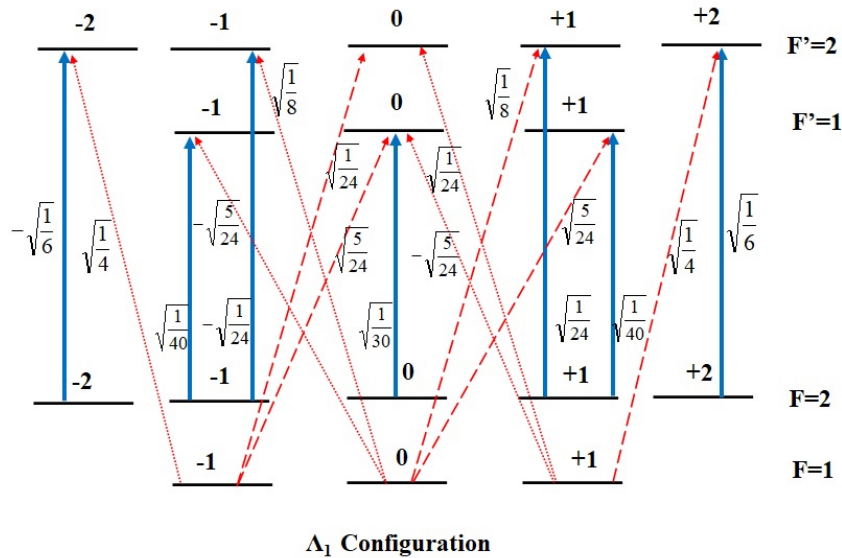


FIGURE 4.11: All possible Λ configurations for probe transition locked at $F = 1 \rightarrow F' = 2$. The blue solid line indicates Pump transition and the red dashed line indicates σ^+ and the red dotted line indicates σ^- probe transition.

By involving the sublevels of $F'=1$, $F=1$ and $F'=2$ four Λ systems are possible. Interestingly, the position of the two photon resonance for this system matches with the peak position of A_2 and A_3 as listed in table 4.3. This further confirms that asymmetry observed is because of the

TABLE 4.4: EIT positions corresponding to each Λ system for Λ_1 configuration.

Sl. No.	Zeeman sublevels involved in Λ system				EIT Positions
	$F=1; m_F$	$F=2; m_F$	$F'=1; m_F$	$F'=2; m_F$	
i	-1	-2	-	-1	$+3\Delta_B$
ii	-1	0	-	-1	$+\Delta_B$
iii	0	-1	-	0	$+\Delta_B$
iv	0	+1	-	0	$-\Delta_B$
v	+1	0	-	+1	$+\Delta_B$
vi	+1	+2	-	+1	$-3\Delta_B$
vii	-1	-2	-1	-	$+3\Delta_B$
viii	-1	0	-1	-	$+\Delta_B$
ix	+1	+2	+1	-	$-3\Delta_B$
x	+1	0	+1	-	$-\Delta_B$

involvement of $F'=1$. Further we repeat the experiment in Λ_2 configuration. In this configuration, probe beam is locked from $F=2$ to $F'=2$ transition and the pump is scanned from the $F=1$ ground level. By involving $F'=1$ there will be multiple Λ system as shown in the energy level diagram (figure 4.12) The calculated two photon resonance position of all the Λ system is listed in table

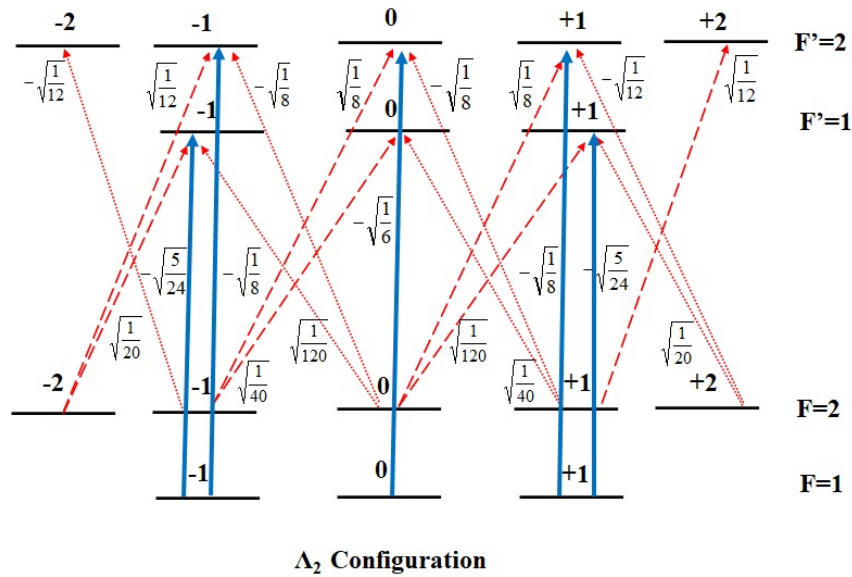


FIGURE 4.12: All possible Λ configurations for probe transition locked at $F = 2 \rightarrow F' = 2$. The blue solid line indicates pump transition, the red dashed line indicates σ^+ and the red dotted line indicates σ^- probe transition.

4.4 As evident from the positions that altogether, four EIT peaks will be observed (because of the overlapping). The probe transmission for this configuration recorded at several different values of the magnetic field is shown in figure 4.13 (a). Similar to Λ_1 configuration, here also we observed

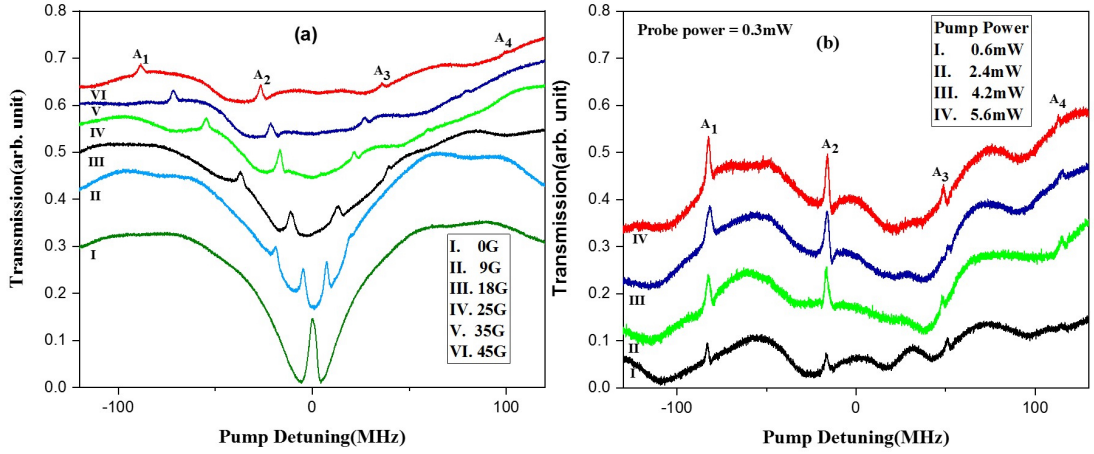


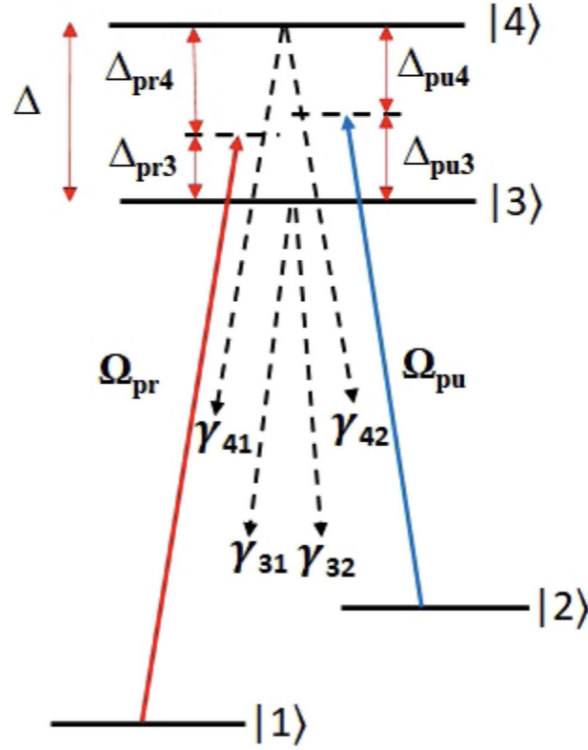
FIGURE 4.13: Experimental results for Λ_2 configuration, (a). for different values of magnetic field at $P_{pu} = 2.4mW$ and $P_{pr} = 0.3mW$, (b) for increasing pump power at $B = 40$ G.

the four well resolved peaks labeled as A_1 , A_2 , A_3 and A_4 . For better resolution, we recorded the spectra by varying the pump power at fixed value of $B=40$ G. The spectra is shown in figure 4.13 (b). In this configuration, no asymmetry was observed. But as mentioned in previous section enhancement of peak A_4 in comparison to other peaks indicates the possibility of population realignment.

4.5.2 The double Λ model

To explain the various observation we model a double Λ system. The energy level diagram is shown in figure 4.14.

We assign the ground states involving magnetic sublevels belonging to $|F = 1\rangle$ and $|F = 2\rangle$ as $|1\rangle$ and $|2\rangle$. Similarly, we designate excited states involving magnetic sublevels $|F' = 1\rangle$ and $|F' = 2\rangle$ as $|3\rangle$ and $|4\rangle$. It is termed as double Λ system because of the presence of two individual Λ system: $|1\rangle \rightarrow |3\rangle \leftarrow |2\rangle$ and $|1\rangle \rightarrow |4\rangle \leftarrow |2\rangle$. By using this configuration we try to understand the case of peak A_3 in the Λ_1 configuration. As it can be seen from table 4.3 there are three Λ systems (sl. no. (ii), (v) and (vii)) which satisfy the two-photon resonance condition at $+\Delta_B$. Out of this two (sl. no. (ii) and (vii)) share the same ground state fulfilling in criteria for form double Λ system. The interaction between these two coupled systems can be understood in terms of the dark and the bright state formalism. For a three level Λ system (say

FIGURE 4.14: Four-level double Λ system with common ground states.

$|1\rangle \rightarrow |3\rangle \leftarrow |2\rangle$) the dark and bright states are defined as [123]

$$|D\rangle = \frac{\Omega_{pu}}{\sqrt{(\Omega_{pu})^2 + (\Omega_{pr})^2}} |1\rangle - \frac{\Omega_{pr}}{\sqrt{(\Omega_{pu})^2 + (\Omega_{pr})^2}} |2\rangle \quad (4.2)$$

$$|B\rangle = \frac{\Omega_{pr}}{\sqrt{(\Omega_{pu})^2 + (\Omega_{pr})^2}} |1\rangle + \frac{\Omega_{pu}}{\sqrt{(\Omega_{pu})^2 + (\Omega_{pr})^2}} |2\rangle \quad (4.3)$$

Since there are two such systems, there will be pairs of dark and bright states. The Rabi frequencies will be scaled by a factor provided by the c_{ij} 's of the relevant transitions. For $|2\rangle \rightarrow |3\rangle$ and $|2\rangle \rightarrow |4\rangle$ the scaled Rabi frequency is $c_{23}\Omega_{pu}$ and $c_{24}\Omega_{pu}$ respectively, similarly it is $c_{13}\Omega_{pr}$ and $c_{14}\Omega_{pr}$ for the transitions $|1\rangle \rightarrow |3\rangle$ and $|1\rangle \rightarrow |4\rangle$.

On inclusion of the above modification, the dark and the bright states involving the states $|1\rangle, |2\rangle$ and $|3\rangle$ is given by,

$$|D3\rangle = \frac{c_{23}\Omega_{pu}}{\sqrt{(c_{23}\Omega_{pu})^2 + (c_{13}\Omega_{pr})^2}} |1\rangle - \frac{c_{13}\Omega_{pr}}{\sqrt{(c_{23}\Omega_{pu})^2 + (c_{13}\Omega_{pr})^2}} |2\rangle \quad (4.4)$$

$$|B3\rangle = \frac{c_{13}\Omega_{pr}}{\sqrt{(c_{23}\Omega_{pu})^2 + (c_{13}\Omega_{pr})^2}}|1\rangle + \frac{c_{23}\Omega_{pu}}{\sqrt{(c_{23}\Omega_{pu})^2 + (c_{13}\Omega_{pr})^2}}|2\rangle \quad (4.5)$$

Similarly, for the Λ system involving $|1\rangle, |2\rangle$ and $|4\rangle$ is given by,

$$|D4\rangle = \frac{c_{24}\Omega_{pu}}{\sqrt{(c_{24}\Omega_{pu})^2 + (c_{14}\Omega_{pr})^2}}|1\rangle - \frac{c_{14}\Omega_{pr}}{\sqrt{(c_{24}\Omega_{pu})^2 + (c_{14}\Omega_{pr})^2}}|2\rangle \quad (4.6)$$

$$|B4\rangle = \frac{c_{24}\Omega_{pu}}{\sqrt{(c_{24}\Omega_{pu})^2 + (c_{14}\Omega_{pr})^2}}|1\rangle + \frac{c_{14}\Omega_{pr}}{\sqrt{(c_{24}\Omega_{pu})^2 + (c_{14}\Omega_{pr})^2}}|2\rangle \quad (4.7)$$

The evolution of the system can be understood on a dark and bright state basis. The dark bright basis that can be constructed from these states are

$\{|D3\rangle, |B3\rangle, |3\rangle, |4\rangle\}$ and $\{|D4\rangle, |B4\rangle, |3\rangle, |4\rangle\}$. The vectors of one basis set can be expanded in the other basis set because they make up the same Hilbert space's basis set. Normally, for a perfect system they are orthogonal to each other i.e. $\langle D3 | B3 \rangle = \langle D4 | B4 \rangle = 0$ and $\langle D3 | B4 \rangle = \langle D4 | B3 \rangle = 0$. The non-orthogonality of this term indicates the influence of one system on the other. The presence of impurity can be evaluated as $|\langle D3 | B4 \rangle|^2$ (or equivalently $|\langle D4 | B3 \rangle|^2$) which is given by,

$$|I_D\rangle = \frac{|c_{24}c_{13} - c_{14}c_{23}|^2(\Omega_{pr}\Omega_{pu})^2}{[(c_{23}\Omega_{pu})^2 + (c_{13}\Omega_{pr})^2][(c_{24}\Omega_{pu})^2 + (c_{14}\Omega_{pr})^2]} \quad (4.8)$$

In other words, this represents the competition between Λ systems $|1\rangle \rightarrow |3\rangle \leftarrow |2\rangle$ and $|1\rangle \rightarrow |4\rangle \leftarrow |2\rangle$ in maintaining dark and bright states. The calculated I_D values for different systems are tabulated in table 4.5.

As it is evident from the table, the I_D value corresponding to A_2 and A_3 is non-zero. And we should expect asymmetry in the profile as observed in the experiment. Although the value of I_D is the same for both configurations but contrary to A_3 , the peak A_2 does not show the

TABLE 4.5: I_D values for different double Λ system.

Sl. No.	Configuration	Zeeman sublevels involved in double Λ system				I_D values
		F=1; m_F	F=2; m_F	F'=1; m_F	F'=2; m_F	
i	Λ_1	0	+1	+1	+1	0.016
ii	Λ_1	0	-1	-1	-1	0.016
iii	Λ_2	+1	+2	+1	+1	0.052
iv	Λ_2	+1	0	+1	+1	0.161
v	Λ_2	-1	0	-1	-1	0.644
vi	Λ_2	-1	-2	-1	-1	0.053

complete conversion to absorption. This is because the transition involved in A_2 is most probable as compared to A_3 . As a result, the asymmetry in peak A_2 is not prominent, although present. In comparison to Λ_1 , as mentioned before no asymmetry was observed for the Λ_2 configuration. In this case, we observed the dominance of A_1 over all the other peaks as shown in figure 4.13. Contrary to Λ_1 , at all the resonance positions (EIT positions) double Λ systems are formed. As per the previous section, in this configuration, we should observe the asymmetry in all the peaks. As per table 4.5, for all four cases, we have a non-zero value. The I_D value of outer peaks A_1 and A_4 are the same and lowest. Whereas, the I_D value of A_2 and A_3 are very high. And the I_D value of A_3 is six times more. Although asymmetry is present in all the cases, we haven't seen any conversion to absorption. In this, detuning of the locked probe plays a very vital role. As we know the scattering rate is given by,

$$R_s = \frac{\Gamma}{2} \frac{I/I_S}{1 + 4\left(\frac{\Delta_{pr}}{\Gamma}\right)^2 + \left(\frac{I}{I_S}\right)^2} \quad (4.9)$$

We can see from equation 4.9 that the scattering rate decreases with increase in the Δ_{pr} , the scattering through the transitions $|F = 2, m_F = 0\rangle \rightarrow |F' = 2, m_F = +1\rangle$ and $|F = 2, m_F = 0\rangle \rightarrow |F' = 1, m_F = +1\rangle$ will be more active than the transitions $|F = 2, m_F = 0\rangle \rightarrow |F' = 2, m_F = -1\rangle$ and $|F = 2, m_F = 0\rangle \rightarrow |F' = 1, m_F = -1\rangle$. This leads to a stronger population alignment towards the $|F = 2, m_F = +1, +2\rangle$ states. Due to this strong population re alignment, the asymmetry as observed for the Λ_1 configuration is not observed in this case in spite of having a non-zero I_D value.

Density matrix solutions

The observed result can also be validated by solving the density matrix equations. This can be done by solving the master equation which is given by [124],

$$\frac{d\rho}{dt} = -\frac{i}{\hbar}[H, \rho] + \mathcal{L}\rho \quad (4.10)$$

where, $\mathcal{L}\rho$ (\mathcal{L} is the Lindblad super-operator) is the phenomenological decay terms which incorporates various decoherence effects and H is the interaction Hamiltonian. In the rotating wave approximation, the Hamiltonian H for the considered four level model (figure 4.14) is given by,

$$\begin{pmatrix} 0 & 0 & -\frac{c_{13}\Omega_{pr}}{2} & -\frac{c_{14}\Omega_{pr}}{2} \\ 0 & \Delta_{pr3} - \Delta_{pu3} & -\frac{c_{23}\Omega_{pu}}{2} & -\frac{c_{24}\Omega_{pu}}{2} \\ -\frac{c_{31}\Omega_{pr}}{2} & -\frac{c_{32}\Omega_{pu}}{2} & (\Delta_{pr3} - kv) - \Delta & 0 \\ -\frac{c_{14}\Omega_{pr}}{2} & -\frac{c_{24}\Omega_{pu}}{2} & 0 & \Delta_{pr3} - kv \end{pmatrix}$$

The Doppler effect is introduced by the term kv in the Hamiltonian where k is the wave vector and v is the atomic velocity.

The imaginary parts of the coherence's ρ_{13} and ρ_{13} were averaged across all velocity classes using the Boltzmann velocity distribution function given by,

$$W(v) = \sqrt{\frac{m}{2\pi K_B T}} \exp\left(-\frac{mv^2}{2K_B T}\right) \quad (4.11)$$

The averaged coherences can therefore be written as,

$$Im(\rho'_{1j}) = \int Im(\rho_{1j})W(v)dv; (j = 3, 4) \quad (4.12)$$

Finally, the transmission

$$T \propto \exp[-c_3 \text{Im}(\rho'_{13}) + c_4 \text{Im}(\rho'_{14})] \quad (4.13)$$

is obtained. Here, $\text{Im}(\rho'_{13})$ and $\text{Im}(\rho'_{14})$ are the averaged coherences. $c_i = \frac{2\pi n |\mu_{1i}|^2 kl}{\epsilon_0 h c_{1i} \Omega_{pr}}$ ($i = 3, 4$), where n , μ_{1i} , ϵ_0 , k and l are number density, dipole moment, permittivity of free space, wave-vector and length of the vapour cell respectively.

The numerical calculation results are shown in figure 4.15 and 4.16. figure 4.15 (a) and (b)

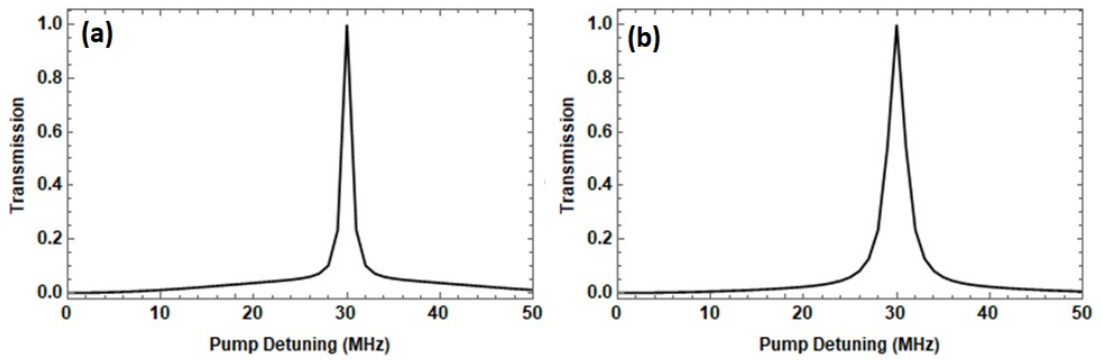


FIGURE 4.15: Theoretical curves. (a). $c_{ij} = 1$ for all $i \rightarrow j$, $\Omega_{pu} = 2 \times \gamma$, $\Omega_{pr} = \gamma$, (b). $c_{ij} = 1$ for all $i \rightarrow j$, $\Omega_{pu} = 4 \times \gamma$, $\Omega_{pr} = \gamma$. $\gamma = 2\pi \times 6\text{MHz}$.

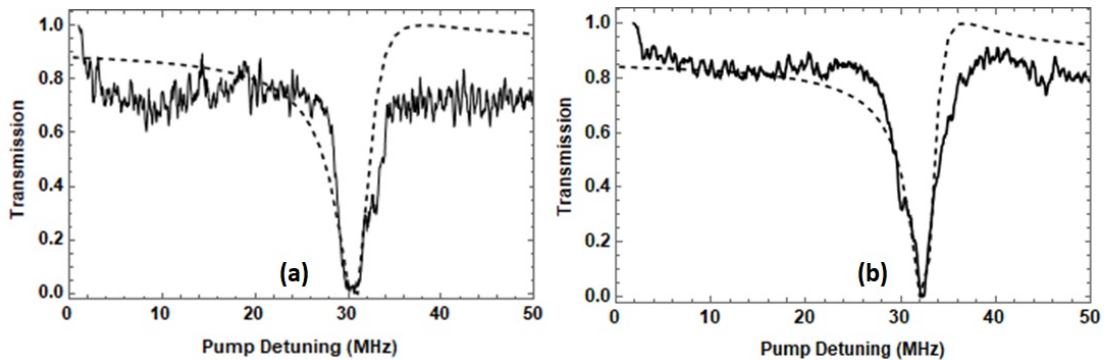


FIGURE 4.16: Experimental (solid) and Numerical (dashed) spectra corresponding to the peak A_3 of Λ_1 configuration. (a). $P_{pr} = 0.3 \text{ mW}$ and $P_{pu} = 2.4 \text{ mW}$. (b). $P_{pr} = 0.3 \text{ mW}$ and $P_{pu} = 5.6 \text{ mW}$.

shows the situation when all $c_{ij} = 1$. Under these conditions, asymmetry is absent, and the usual probe transmission spectra can be obtained. Apart from broadening, no change is observed when Ω_{pu} is increased (figure 4.15 (b)). By choosing $c_{ij} \neq 1$ such that $|c_{24}c_{13} - c_{14}c_{23}| \neq 0$ and hence $I_D \neq 0$ the resulting spectra from the numerical calculations are displayed in figure

4.16(a) and (b) for two different values of Ω_{pu} (P_{pu}). The spectra have been compared to those of experiments. The numerical solution is found in good agreement with experimental results. The c_{ij} are selected as exact values for the double Λ system responsible for the peak A_3 as seen in the experimental results for the Λ_1 configuration.

4.5.3 Controlling asymmetry in EIT

The origin of asymmetry as discussed in the previous section for a particular polarization combination of the lasers is essential because of the involvement of the nearby hyperfine state. This asymmetry is sometimes desirable, as in the case of subluminal to superluminal switching. However, for certain applications, this effect must be negligible. One way is to obtain EIT for some other polarization combination as seen in the previous section. In general, both the phenomena i.e. EIT and absorption can be distinguished in terms of off-resonant and on-resonant processes based on the different velocity classes participating in the two-photon resonance. The off-resonant process gives absorption and the on-resonant process produces transmission, for a very low value of the probe power, absorption i.e. off-resonant process dominates. However, by tuning the probe power, the number of atoms participating in the off and on-resonant process can be controlled and desired transmission peak can be obtained [125]. Another way of controlling the asymmetry or the off-resonant process induced absorption is by the use of an anti-relaxation coated cell where the number of atoms participating in the off-resonant process can be heavily reduced which is the ongoing research from our group. It is also expected that the asymmetry would disappear with the high magnetic field. However, while working with ^{87}Rb this is not possible since, with the increase in the magnetic field, the level crossing absorption [126] starts to dominate. Asymmetry disappearing with the magnetic field can however be experimentally realized for some other atoms for which level crossing effects are minimal even for the high magnetic field.

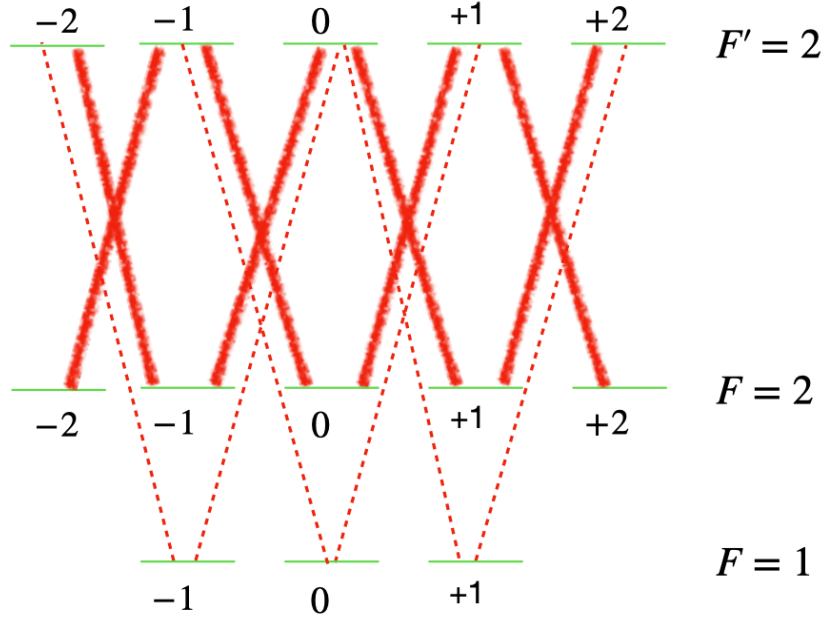


FIGURE 4.17: Level diagram for illustration of possible Λ configurations. The solid lines in the level diagram signify the pump field and the dashed line probe field, both are σ polarised.

4.6 EIT in Longitudinal Magnetic Field

For completeness, we also investigate the response of atoms in presence of the longitudinal magnetic field (LMF). For this experiment probe is locked at $|F = 1\rangle$ to $|F' = 2\rangle$ transition. The power of the pump and probe laser is kept fixed at 4.5 mW and 1 mW respectively. In this configuration, the magnetic field is oriented parallel to the propagation direction of the laser. The polarization of the pump and probe are linear and orthogonal to each other. As a result, in the lab frame, both lasers are σ polarised. Following the selection rule, the energy level diagram is shown in figure 4.17. As evident from the energy level diagram, there are ten possible Λ configurations as listed in table 4.6. The resonance at $\Delta_{pu} = -2\Delta_B$ is as a result of the following Λ configurations having common two photon detuning condition;

1. $|F = 1; m_F = +1\rangle \longleftrightarrow |F' = 2; m_{F'} = +2\rangle \longleftrightarrow |F = 2; m_F = +1\rangle$
2. $|F = 1; m_F = +1\rangle \longleftrightarrow |F' = 2; m_{F'} = 0\rangle \longleftrightarrow |F = 2; m_F = +1\rangle$
3. $|F = 1; m_F = 0\rangle \longleftrightarrow |F' = 2; m_{F'} = +1\rangle \longleftrightarrow |F = 2; m_F = +2\rangle$

TABLE 4.6: EIT position corresponding to each Λ in the presence of longitudinal magnetic field corresponding to figure 4.17

Sl. No.	Zeeman sublevels involved in Λ system			EIT Positions
	$F=1; m_F$	$F'=1; m_{F'}$	$F=1; m_F$	
i	+1	+2	+1	$-2\Delta_B$
ii	+1	0	+1	$-2\Delta_B$
iii	0	+1	+2	$-2\Delta_B$
iv	0	+1	0	0
v	0	-1	0	0
vi	-1	0	+1	0
vii	+1	0	-1	0
viii	-1	0	-1	$+2\Delta_B$
ix	-1	-2	-1	$+2\Delta_B$
x	0	-1	-2	$+2\Delta_B$

Resonance at $\Delta_{pu} = 0$ is as a result of the following Λ configurations having common two photon detuning condition;

1. $|F = 1; m_F = 0\rangle \longleftrightarrow |F' = 2; m_{F'} = +1\rangle \longleftrightarrow |F = 2; m_F = 0\rangle$
2. $|F = 1; m_F = 0\rangle \longleftrightarrow |F' = 2; m_{F'} = -1\rangle \longleftrightarrow |F = 2; m_F = 0\rangle$
3. $|F = 1; m_F = -1\rangle \longleftrightarrow |F' = 2; m_{F'} = 0\rangle \longleftrightarrow |F = 2; m_F = +1\rangle$
4. $|F = 1; m_F = +1\rangle \longleftrightarrow |F' = 2; m_{F'} = 0\rangle \longleftrightarrow |F = 2; m_F = -1\rangle$

Resonance at $\Delta_{pu} = +2\Delta_B$ is as a result of the following Λ configurations having common two photon detuning condition;

1. $|F = 1; m_F = -1\rangle \longleftrightarrow |F' = 2; m_{F'} = 0\rangle \longleftrightarrow |F = 2; m_F = -1\rangle$
2. $|F = 1; m_F = -1\rangle \longleftrightarrow |F' = 2; m_{F'} = -2\rangle \longleftrightarrow |F = 2; m_F = -1\rangle$
3. $|F = 1; m_F = 0\rangle \longleftrightarrow |F' = 2; m_{F'} = -1\rangle \longleftrightarrow |F = 2; m_F = -2\rangle$

The probe transmission recorded for this configuration at different value of magnetic field is shown in figure 4.18. At 0 G, similar to previous cases here also we observe single EIT. As we increase the magnetic field, single EIT splits into symmetrical three peaks. The peak positions

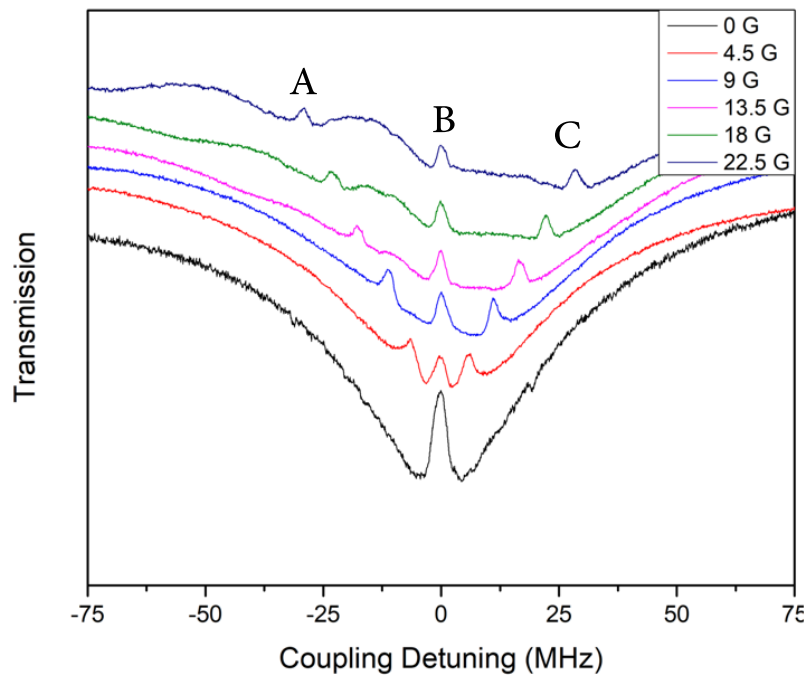


FIGURE 4.18: Splitting of EIT resonance due to the presence of a longitudinal magnetic field.

were found to be in conformity with the calculated position (see table 4.6.) Contrary to transverse magnetic field, in this configuration the EIT at 0 MHz does not disappear. As we increase the magnetic field, the reduction in the linewidth of EIT peaks is observed as seen in figure 4.19.

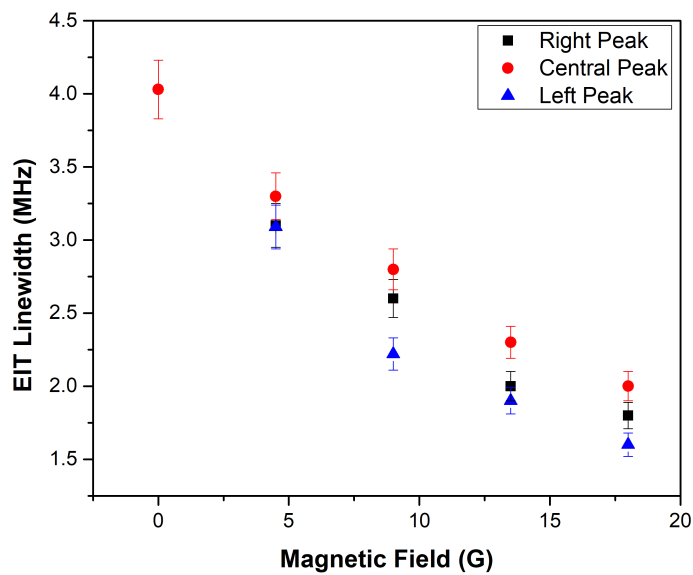


FIGURE 4.19: EIT linewidth for different values of the magnetic field.

By varying the magnetic field from 0 G to 20 G, the linewidth reduces approximately by a factor of 2. The reason for reduction is same as it happens in thermal averaging. In thermal averaging, the moving atoms fill in the transparency windows [102]. The narrowing of EIT as observed in longitudinal orientation was absent in transverse. This is because of having π and σ polarised beam the population alignment was not uniform. Contrary, to transverse orientation in this case no such asymmetry is observed. This is because of two reasons. First, uniform distribution of population. Second, absence of double Λ system.

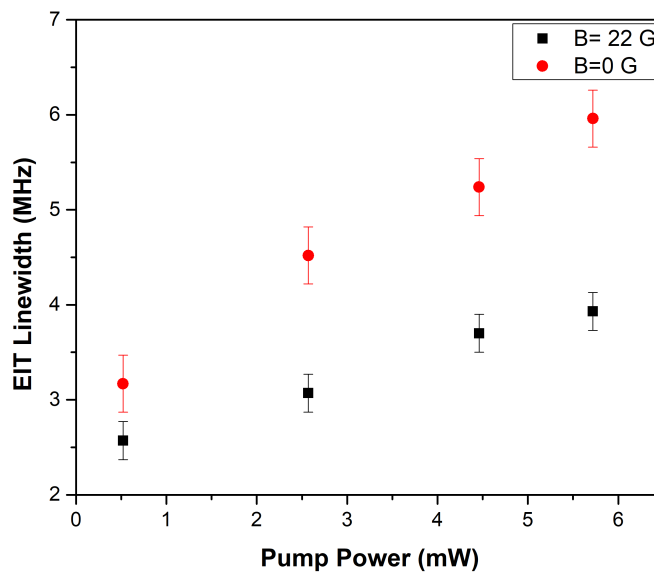


FIGURE 4.20: EIT linewidth for different values of pump power. The plot shows how EIT linewidth increases with pump power magnetic field zero and 22 G.

As shown in figure 4.20, we monitor the linewidth of the central peak as a function of pump power. For this, we took two sets of data i.e. at 0 G and 22 G. in both the sets, linewidth increases with the increase in the power as expected. By varying the power from 0.5 mW to 6 mW the linewidth of the peak at 0 G increases by a factor of 3. Whereas at 22 G the variation is by a factor of approximately 1.5. The amplitude also varies as we increase the magnetic field. The amplitude of each EIT peak decreases by $(30 \pm 5)\%$ as compared to EIT at 0 G. No substantial differences were formed between the three EIT peaks. As shown in figure 4.21, we also monitor

the separation in two EIT peaks. Similar to the transverse orientation, it varies linearly with the magnetic field and is found to be $2\Delta_B$.

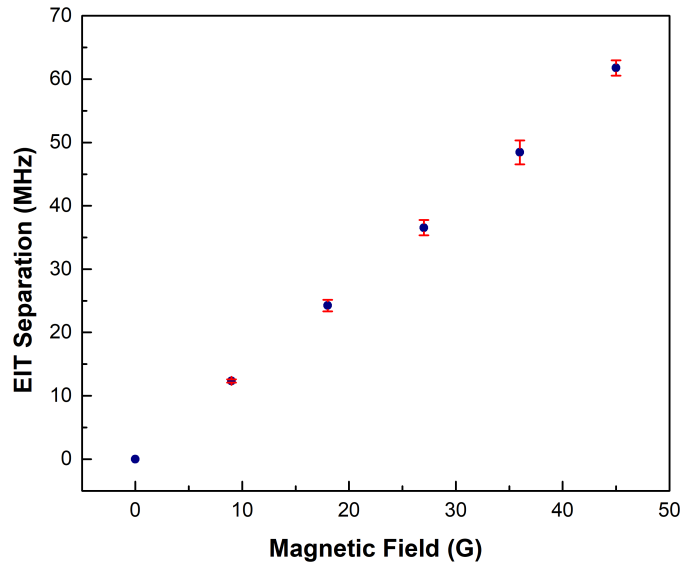


FIGURE 4.21: Dependence of separation between two consecutive EIT peaks on the magnetic field.

4.7 EIT in a degenerate two-level system

In the previous section, we investigated the process of EIT in a three-level system. As discussed in the three-level system, the coherence is induced by involving a laser beam. However, despite the extensive research on this system, simple systems are always in demand. Various coherence phenomena are well understood in a pure two-level system. And as discussed, by involving the magnetic field various complicated systems are realized. Similarly, by having a degenerate two-level system (DTLS) exposed to magnetic field different configurations coupled with a laser beam can be realized. DTLS in presence of a magnetic field gives rise to several superposed three-level systems and pure two-level systems. In this section, we have discussed the DTLS system in presence of the magnetic field and laser.

TABLE 4.7: EIT position corresponding to each Λ in DTLs

Sl. No.	Zeeman sublevels involved in Λ system			EIT Positions
	$F=1; m_F$	$F'=1; m_{F'}$	$F=1; m_F$	
i	+1	+1	0	$-\Delta_B$
ii	0	0	+1	$-\Delta_B$
iii	0	0	-1	$+\Delta_B$
iv	-1	-1	0	$+\Delta_B$

4.7.1 Effect of transverse magnetic field

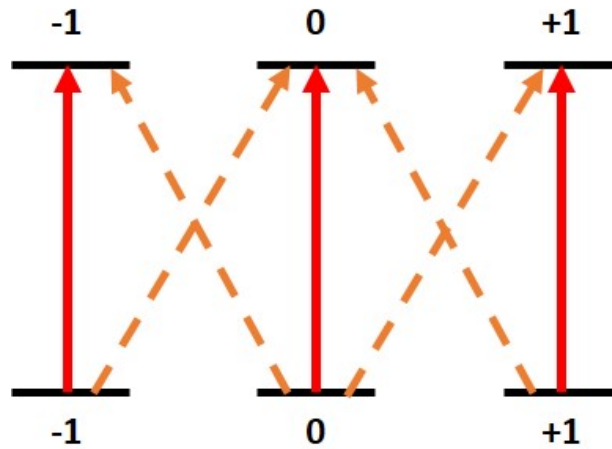


FIGURE 4.22: Level diagram illustrating degenerate two-level system (DTLS).

The two-level energy level structure is shown in figure 4.22. The transition $^5S_{1/2} (F_g=1) \rightarrow ^5P_{3/2} (F_e=1)$ of the ^{87}Rb D_2 line is selected as degenerate two-level system for investigation. The probe laser frequency is locked at $|F = 1\rangle \rightarrow |F' = 1\rangle$ transition and the pump laser is kept at scanning mode from the same ground level. The pump is π -polarised and the probe is σ -polarised in the atomic frame. As shown in the energy level structure (figure 4.22), four Λ systems are possible. As the system is closed, it is expected to have an EIT effect in probe transition. Figure 4.23 (a) shows the transmission spectra of a probe beam recorded for different value of magnetic field.

For this experiment, the pump and probe power is fixed at 1.5 mW and 0.06 mW respectively. At $B = 0$ G as expected we observe the EIT because of the polarization of the optical beam. As we increase the magnetic field the single EIT splits into two EITs because of the upliftment of

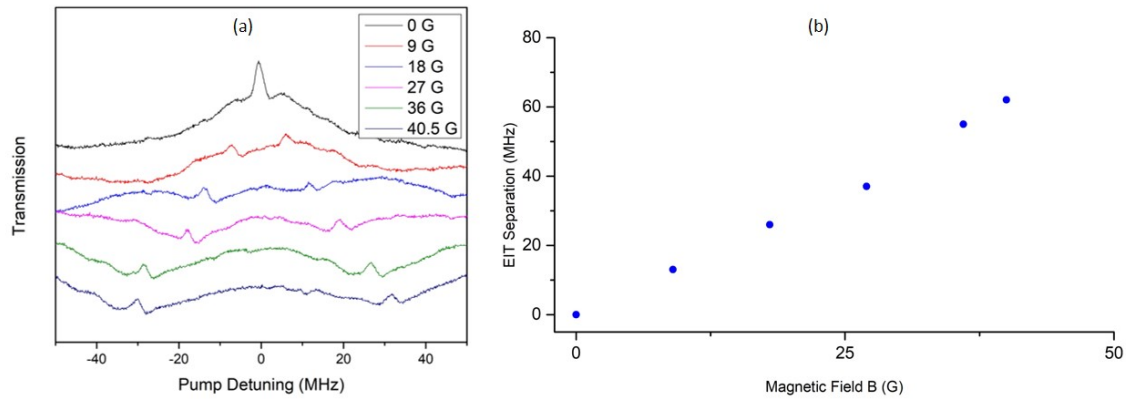


FIGURE 4.23: (a) Response of EIT spectrum to the applied magnetic field. (b) Linear dependence of separation between EIT peaks.

degeneracy. At $B \neq 0$ G, the coherence between Zeeman sublevels and laser beam results in two EIT peaks. The position of peaks is found to be in confirmation with the calculated value as shown in table 4.7. As the magnetic field is increased the EIT maxima shifts from zero detuning. The separation between the EIT maxima varies linearly as seen in figure 4.23 (b).

4.7.2 Effect of pump intensity

Keeping the probe fixed at 0.06 mW, we change pump intensity from 0.1 mW to 1.5 mW. The amplitude of EIT increases linearly with pump intensity. DTLS consists of multiple Zeeman sublevels belonging to two hyperfine states. There is no third hyperfine state which would otherwise act as a supplementary population reservoir. Due to the absence of a third hyperfine state in the DTLS, there is no probability of population realignment, also there is a very less probability of observing asymmetry in this system for the same reason. figure 4.24 shows very little change in EIT linewidth measured at FWHM. This is because, in a vapor cell, atoms with different velocities interact with laser frequency resulting shift in transparency peak. While averaging over all possible velocities, they fill in the transparency region for stationary atoms. Hence, the transparency region shrinks and becomes less sensitive to pump intensity [78]. It should be noted that to observe EIT in DTLS the probe and the pump laser have to be from $F=1$ ground level for the ^{87}Rb D_2 line, if it is locked from $F=2$ ground level, the conditions of another phenomenon known as EIA is fulfilled which is discussed in the next chapter.

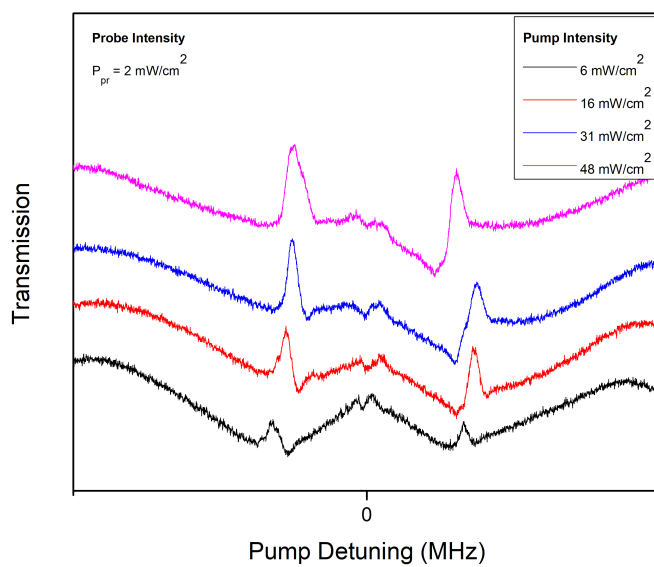


FIGURE 4.24: Effect of pump intensity EIT for a fixed value of the magnetic field.

Chapter 5

Electromagnetically Induced Absorption

5.1 Introduction

EIA is a coherent phenomenon characterized by enhancement of absorption in an atomic medium [127]. The enhanced absorption peak is of sub-Doppler width. It was predicted and demonstrated in two consecutive papers from A.M. Akulshin in 1998. In their first work [42], they involved a DTLS of atoms coupled by two co-propagating lasers fields, where they performed experiments for various sets of DTLS involving ground and excited hyperfine levels of ^{85}Rb . For the configuration $|F=2\rangle \rightarrow |F'=3\rangle$, they observed enhanced absorption having sub-Doppler width. They named it EIA. The presence of EIA was attributed to the coherence between the Zeeman sub-levels of the ground state hyperfine levels induced by the lasers. Apart from $|F=2\rangle \rightarrow |F'=3\rangle$, in all the other cases they observed EIT. Based on the observation they laid out the following criteria: For EIA, in a two-level system, the transition between the ground level F and excited level $F'=F+1$ is required. In the second work from the same group by A. Lezama *et al.* in [45], they have demonstrated experimentally and theoretically the enhancement in EIA by choosing the hyperfine states laying out the following criteria:

1. $F'=F+1$
2. transition should be closed

3. the ground state must be degenerate ($F \neq 0$)

The first condition ensures the absence of a dark state in the system resulting in the absorption in a two-level system. As all the previous work has demonstrated EIA in the DTLS system. Interestingly, the standard systems involving three levels configurations (Λ , V , and *Ladder*) used to explain the sub doppler phenomenon like EIT failed to explain the observed phenomenon. As discussed in the previous chapter, it is to be noted that observed sub-doppler absorption in a three-level system is present because of the off-resonant scattering like Raman scattering [128]. The presence of off-resonant scattering in three-level system was further explained by involving the close-lying states forming a double- Λ system (a four-level system). In [53], it has been explained how the presence of extra atomic states within allowed dipole transition of one of the states involved in the Λ system leads to spectral change. Depending on the number of states involved, the resultant spectrum changes from the transmission to absorption and back to the transmission. In all the previous works there was no mention of the types of the system present in DTLS which is responsible for the EIA. Taichenachev *et.al* in [128] showed that EIA occurs because of the spontaneous transfer of coherence. Rautian *et al.* in their work [129] introduced the concept of spontaneous transfer of coherence from the excited state to the ground state and demonstrated how this process changes nonlinear saturation spectroscopy. The transfer of coherence depends on many factors including the relative splitting of adjacent states. N-configuration is the basic system for the realization of transfer of coherence and can be easily realized in the DTLS system in the presence of the magnetic field and two orthogonally polarised lights.

Kim *et al.* in [130] observed EIA in an open system defying requirements (i) and (ii) predicted by Lezama *et al.*. Goren *et al.* in the series of work in [131, 132] had been successful in rationalising the above two arguments. They have concluded that there are two kinds of EIA in DTLS system formed by satisfying the criteria $F \rightarrow F' (=F+1)$: (i) due to transfer of coherence (TOC) when the DTLS system interacts with the pump and probe beam of different polarization i.e Zeeman sublevels of excited state and ground state will form the chain of several N-system, (ii) due to transfer of population (TOP) when DTLS system interacts with same polarized pump and probe by forming the chain of two-level system. Zigdon *et al.* in [133] showed that by uplifting the

degeneracy of any DTLS system (including open system) EIA can be observed due to TOC. In the same work, they showed when the pump is σ -polarised and the probe is π -polarised or vice-versa, EIA will be due to the coherence between nearest Zeeman sublevels. The maximum contribution, in this case, will be from the outermost Zeeman sublevels. For σ^+ pump and σ^- probe, EIA will be due to coherence from the next-nearest Zeeman sublevels. The dependence of EIA linewidth on the probe and pump power has also been studied by Molella *et al.* [134]. Ye *et al.* [135] reported a narrow dip of EIA superimposed on a transmission peak due to saturation of atomic population in Doppler broadened optical pumping window of Rb atomic vapor. They numerically showed that the observed EIA dip is due to four level N configurations. EIA has also been predicted theoretically due to incoherent collision but the dynamics are slightly different. Xihua *et al.* in [136] have theoretically observed that with the increase in the collisional decay rate EIT can be converted to EIA, provided that the probe power is not too weak. When the polarization of both laser fields is the same transfer of coherence is not possible. Therefore, EIA observed is due to the TOP. In such a case, the DTLS system reduces to a series of two-level systems. TOP is caused by spontaneous decay and collisional transfer between ground states. In an open system, EIA due to TOP requires that the effective decay rate to the reservoir from the ground state should be greater than that of the excited state [132, 137]. The simplest form of four level system is a N configuration consisting of four atomic states as shown in figure 5.1, two states each of ground and excited states, connected by a strong pump and a weak probe beam. It is an ideal N configuration where dipole transition is allowed between $|1\rangle$ and $|2\rangle$, $|3\rangle$ and $|4\rangle$, and $|1\rangle$ and $|4\rangle$. Two pump beams derived from the same laser source interacts with transitions $|1\rangle \rightarrow |2\rangle$ and $|3\rangle \rightarrow |4\rangle$. Weak probe beam interacts with transition $|1\rangle \rightarrow |4\rangle$. Coherence between two excited states and two ground states is connected by the pump beam and spontaneous decay. Ground state coherence, which in the case of three-level system would have been responsible for destructive interference, is now dependent on excited state coherence. The coherence mediated through spontaneous decay leads to enhancement of absorption. In recent experiments, the EIA is realized by involving four hyperfine states. For this three lasers are required, out of which two lasers of comparable intensity will act as a pump and one weak laser as a probe. When one of the pump beams is detuned by a few GHz from the atomic resonance it leads to broadening and

shifting of transmission peak [138]. However, when both the pump beams are resonant within the limits of hyperfine transition, the resultant spectrum is absorption. Therefore, any of the pump beams in N-configuration responsible for absorptive resonant must not be far detuned from resonant transition [139]. Contrary to that multiple N-configuration can be realized in DTLS. Multiple N configurations are readily made available in DTLS consisting of Zeeman sublevels by applying the appropriate pump and probe beam. As applied fields are resonant with the hyperfine transitions detuning of the coupling field connecting different Zeeman transitions is negligibly small. Therefore, they form a perfect N configuration rather than a distorted Λ or V system. Each N configuration formed by the nearest four Zeeman sublevels contributes to the spectral change at a position defined by detuning the laser field from the transition. Change in the amplitude of applied magnetic field changes existing coherence between the states which shall be discussed in the later sections. Our long-term objective of this experiment is to optimize the system for its usage in quantum memory. As demonstrated by Lezama *et al.* retrieval of a light pulse is not exclusively for the EIT medium. It can be realized in very general conditions including EIT and EIA. Attracted by simple configuration and minimum requirement of optics we wanted to explore the possibility of realizing the same in our system. Secondly, we aim at making a detailed study of the effects of magnetic field on EIA and try to understand which atomic Zeeman sublevels have the major contribution to the resultant spectral changes.

5.2 Four-level N system: Theoretical Description

As mentioned before for realizing a four-level N system three lasers are required. Contrary to that, in DTLS along with the magnetic field two lasers are required to form N level system. It is because, for the low magnetic field, the same laser can address two different ground and excited state pairs. For the probe, we can use another laser. To discuss EIA theoretically a simple four-level N-system is drawn in figure 5.1. Solid lines indicate transition induced by the pump beam and the dashed-dotted line indicates that of the probe. Angular frequency of pump and probe is denoted by ω_{pu} and ω_p respectively. In the given four-level N system, Zeeman states

$|1\rangle$ and $|3\rangle$ belong to a ground state hyperfine energy level and $|2\rangle$ and $|4\rangle$ belong to the excited state hyperfine level. Pump and probe detuning Δ_{c1} , Δ_{c2} and Δ_p defined as $(\omega_{12}-\omega_{pu})$, $(\omega_{34}-\omega_{pu})$ and $(\omega_{32}-\omega_p)$ respectively. In the above definition, ω_{12} , ω_{34} and ω_{32} are resonant frequency corresponding to transitions $|1\rangle \rightarrow |2\rangle$, $|3\rangle \rightarrow |4\rangle$ and $|3\rangle \rightarrow |2\rangle$ respectively.

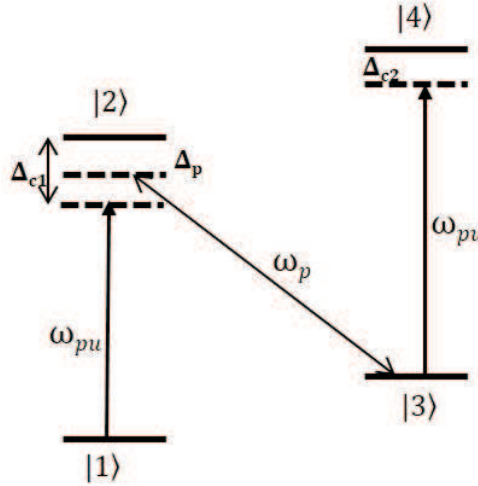


FIGURE 5.1: Energy level diagram of one of the four level N system formed by π polarised pump and σ^- polarised beam

The internal dynamics of four level atomic system is described by density matrix equation [128];

$$\frac{d\rho_{ij}}{dt} = -\frac{i}{\hbar}[H_I, \rho_{ij}] - \frac{1}{2}\{\Gamma, \rho\} + \Gamma \sum_{q=1,2} Q_q^\dagger \rho Q_q \quad (5.1)$$

where, $Q_1 = A|2\rangle\langle 1| + |4\rangle\langle 3|$, $Q_2 = B|2\rangle\langle 3|$ and A and B are real numbers such that $A^2 + B^2 = 1$. Γ is decay rate from excited state to the ground. The subscripts i and j range from 1 to 4 for four level system.

First term in right hand side of the equation-5.1 corresponds to interaction Hamiltonian, second term takes into account the decay rates and the last term corresponds to the transfer of coherence from excited states to the ground.

The interaction Hamiltonian of the system in matrix form is given by;

$$H_I = \begin{pmatrix} \Delta_{C1} & c_{12} \frac{\Omega_{c1}}{2} & 0 & 0 \\ c_{21} \frac{\Omega_{c1}^*}{2} & 0 & c_{23} \frac{\Omega_p}{2} & 0 \\ 0 & c_{32} \frac{\Omega_p^*}{2} & \Delta_P & c_{34} \frac{\Omega_{c2}}{2} \\ 0 & 0 & c_{43} \frac{\Omega_{c2}^*}{2} & \Delta_{C2} - \Delta_P \end{pmatrix}$$

The set of the coupled differential equation obtained for each N-system along with the population conservation equation, $\sum_{i=1}^4 \rho_{ii} = 1$ are solved under steady-state conditions. Theoretical probe spectrum is obtained by plotting $\text{Im } \rho_{32}$ as a function of pump detuning as shown in figure 5.2. The polarization of the pump and the probe in theoretical calculations have been taken into account by introducing Clebsch-Gordan coefficient in the interaction Hamiltonian. The effect of magnetic field on probe spectrum is taken into account through the pump (Δ_{C1} and Δ_{C2}) and probe (Δ_P) detuning. The position of the transmission spectrum is defined by $\delta = \Delta_{C1} + \Delta_{C2} + \Delta_P$ whereas that of the EIA with respect to transmission peak is defined by $\Delta_{C2} - \Delta_{C1}$. As shown in figure 5.2 in absence of the magnetic field, the EIA shift from the transmission line.

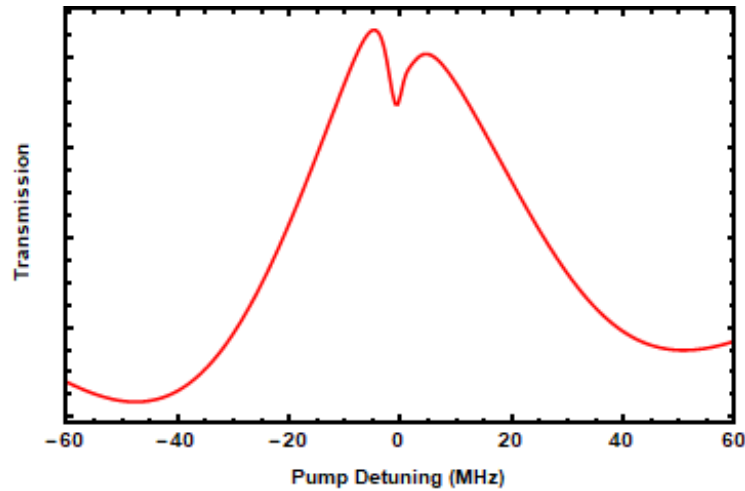


FIGURE 5.2: Theoretically obtained EIA curve with following parameters; $\Delta_{C1} = \Delta_{C2}$, $\frac{\Omega_C}{\Omega_P} = 10$, $\Gamma \equiv 6$ MHz, Clebsch-Gordan coefficients: $C_{12} = C_{21} = \sqrt{\frac{4}{15}}$, $C_{34} = C_{43} = \sqrt{\frac{3}{10}}$, $C_{23} = C_{32} = \sqrt{\frac{1}{6}}$

5.3 Probe response for DTLS system in presence of magnetic field

The observed saturation transmission profile of probe beam in DTLS system for the following two condition:

- Weak pump beam
- Exposed to magnetic field

can be understood by using the model proposed by Nakayama [140]. In saturation spectroscopy for the two-level system the presence of a strong pump beam (intensity higher as compared to saturation intensity) saturates the specific atomic transition line. As a result, the weak probe transmits without getting absorbed. Hence, on monitoring the probe beam we observed transmission.

In this work we have a DTLS system exposed to the magnetic field, the shifted Zeeman sublevels will form multiple transitions including three levels systems. For a system in which three or more level atomic systems are involved even a weak pump beam can affect the ground state coherence and optical pumping start playing a prominent role. Hence, based on the configuration (Lambda or Vee) either absorption or transmission would be observed. The model proposed takes into account a single optical pumping cycle without a saturation effect. As we are working on the low probe and pump power, the proposed approximation is valid in our experiment.

According to proposed model the susceptibility can be expressed as

$$\chi_{j,j}^i \propto \frac{\sum_{i,j} I_{j,j}^i \exp[-(\Delta\omega_{i,j}/2ku)^2]}{[(\Delta - kv) - i\gamma]} \quad (5.2)$$

where ω_i and ω_j are the pump and probe transition. Δ is the detuning from the resonance and defined as $\omega - \omega_{i,j}$. u is the most probable velocity and v is the velocity of atoms moving in the direction of propagating laser. The exponential part only have a relevance in the presence of

crossover [140] and is taken as unity in our case. The subscript and superscript associated with χ is the polarisation state of pump and probe respectively and will be denoted as 0 for linear polarisation, $-$ for σ^+ polarisation and $+$ for σ^- polarisation. γ is the linewidth which takes into account all type of broadening effects i.e. natural, transit time, power broadening and so on. The presence of two linearly polarised laser having polarisation plane perpendicular to each other will induce linear optical anisotropy. In this case the susceptibilities should exhibit symmetry and will be given by

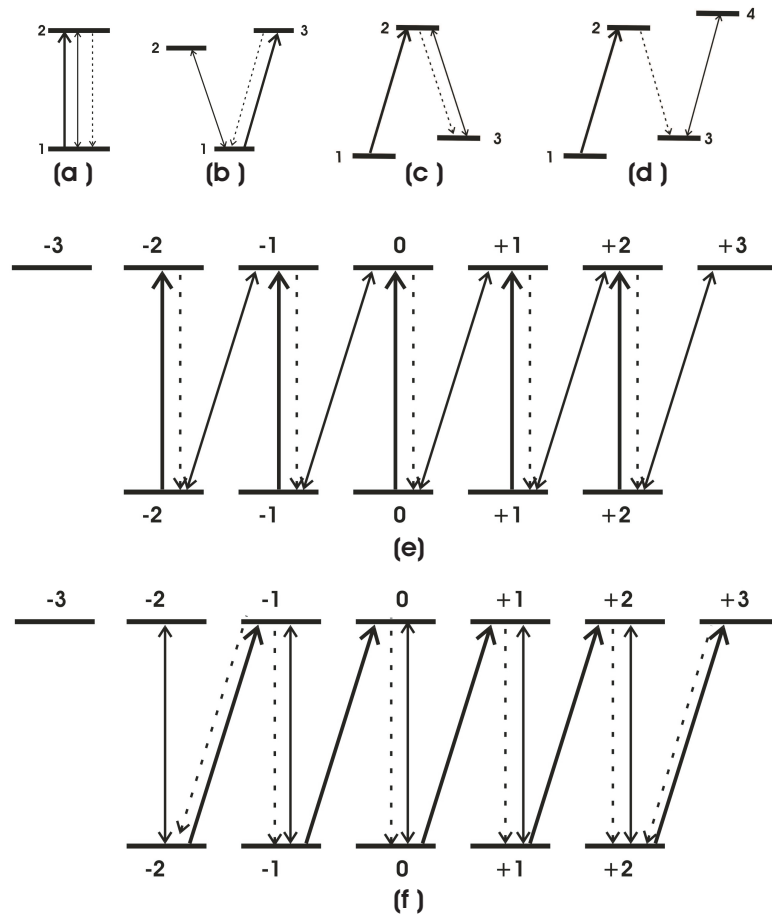


FIGURE 5.3: Four types of resonance: I-shaped two level (a), V-shaped three level (b), Λ -shaped three level (c) and N-shaped four level (d). Series of V-shaped three level resonances for π -polarized pump and σ -polarized probe (e). Series of Λ and V-shaped three level resonances for π -polarized pump and σ -polarized probe (f). Thick line indicates the pump transition, thin line for probe transition and dotted line indicates the spontaneous decay

$$\chi_{00,\pm\pm}^{(0,\pm)} \propto \sum_{i,j} \frac{I_{00,\pm\pm}^{(0,\pm)}}{[(\Delta - kv) - i\gamma]} \quad (5.3)$$

For the atoms interacting with the lasers in presence of magnetic field the resonances present can be classified into 4 classes (i) I-shaped principle resonance (figure 5.3(a)) (ii) V- shaped three level resonance (figure 5.3(b)) (iii) Λ -shape three level resonance (figure 5.3(c)) and (iv) N-shaped four level resonance (figure 5.3(d)). The relative magnitude $I_{00,\pm\pm}^{(0,\pm)}$ for each of the resonance present is given by

$$I_{00,\pm\pm}^{(0,\pm)} = |\mu_{pu}|^2 |\mu_p|^2 \left(-\delta_{i,sp} + \frac{|\mu_{sp}|^2}{\Gamma} \right) \quad (5.4)$$

where $|\mu_{pu}|^2$ and $|\mu_p|^2$ are the transition probabilities corresponding to pump and probe beam. $|\mu_{sp}|^2/\Gamma$ is the branching ratio of the upper excited state. The values of all these are obtained from figure 5.11. $\delta_{i,sp}$ indicates the depopulation of ground state by pump beam and is taken as unit for I-shaped and V-shaped resonances and 0 for λ and N-shaped resonance. The absorption coefficient would be proportional to imaginary part of the calculated χ . For fixed polarisation of pump and probe χ should be summed together for all possible Zeeman transition and saturation signal, $I \propto \text{Im}[\sum \chi]$. For simulation $|\mu_{pu}|^2$ and $|\mu_p|^2$ were multiplied by there respective Rabi frequency Ω_{pu} and Ω_p and then integrated over all the velocity class.

For π polarised pump and σ^+ probe all possible transitions are shown in figure 5.3(e). From the figure, it can be seen that each ground state Zeeman sublevel is connected to the two upper Zeeman sublevels via pump and probe beam forming a 5 V-shaped resonance. Due to symmetry, the same number of V-shaped resonances will be obtained for the σ^+ probe. The obtained transmission spectra calculated using equation-1 for three different magnetic fields 20 G, 30 G, and 40 G are shown in the first column of figure 5.4. In this case, we observe two well-resolved transmission peaks. As we increase the magnetic field, the separation increases. The separation follows the shift induced by the applied magnetic field. The same pattern follows in the experiment as discussed in the latter section.

Similarly for the case where σ^+ polarised beam is the pump and π polarised is the probe all the transitions are shown in figure 5.3(f). With σ^- polarised beam as pump we will have symmetry. Contrary to the previous case the transitions involving the $m_F = -1, 0, 1$ will form λ system by having two ground Zeeman sublevels connected to single upper Zeeman sublevels and the

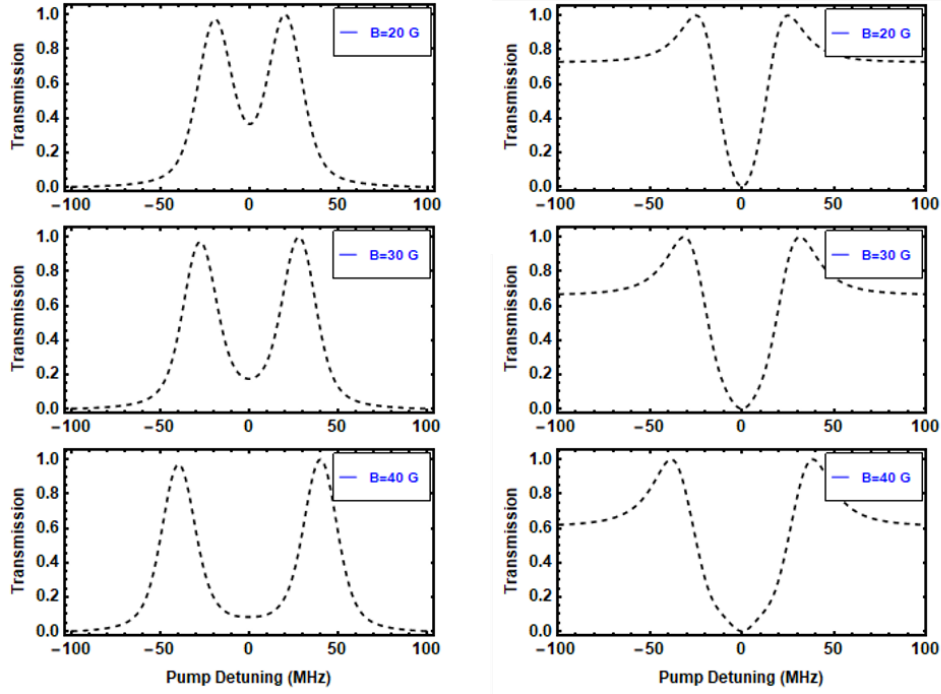


FIGURE 5.4: Theoretical probe transmission spectra with following parameters: $\frac{\Omega_C}{\Omega_P} = 10$, Overall detuning factor $\delta \leq 10$ MHz, Spontaneous decay rate $\Gamma \equiv 6$ MHz. First Column: π -polarized pump with magnetic field 20 G, 30 G and 40 G. Second Column: σ -polarized pump with magnetic field 20 G, 30 G and 40 G.

transitions involving $m_F = +2$ ground states will form V-shaped resonance. For the magnetic field of 20 G, 30 G, and 40 G the simulated spectra are shown in the second column of figure 5.4. Contrary to the previous case, in this case, we observe broad absorption at the center along with two transmission peaks at the wings.

5.4 Experiment: Observation and Discussion

5.4.1 Layout of Experiment

The optical setup for the demonstration of EIA is shown in figure 5.5(a). The probe and coupling field are co-propagating passing through the vapor cell whose temperature is maintained at 40°C. The pump and probe beam are derived from two independent laser sources both of which are 780 nm external cavity diode lasers discussed in chapter 2. The probe beam is locked to the desired transition following the procedure discussed in section 2.7 of chapter 2. The pump beam is kept

in the scanning mode. The measured intensity of the pump is 20 mW/cm^2 and that of the probe is 0.9 mW/cm^2 . The intensities calculated are for the power measurement done in front of the vapor cell before the interaction of the beam with the atomic vapor. The intensities of both the laser beams are kept fixed unless explicitly mentioned in the later texts.

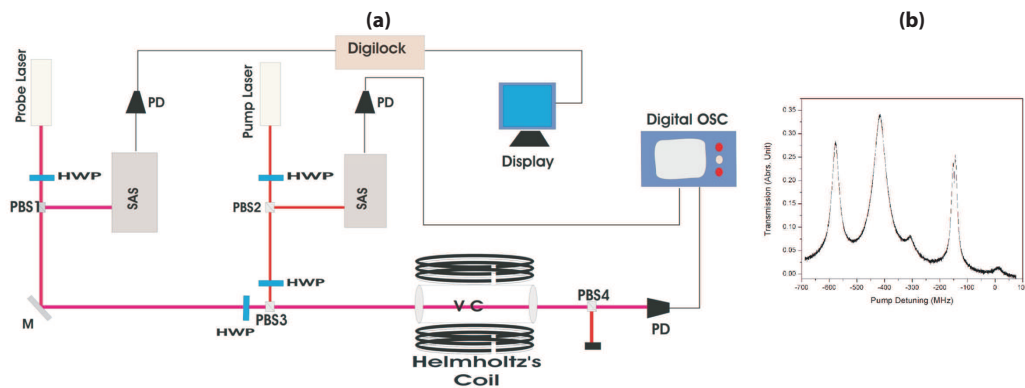


FIGURE 5.5: Experimental setup for observation of EIA and the effect of magnetic field. PBS-Polarizing beam splitter; HWP-Half wave plate; PD-photodiode; VC-vapor cell; SAS-Saturated Absorption Spectroscopy setup.

5.4.2 Zero Magnetic Field

The transmission spectrum obtained at $B = 0 \text{ G}$ and probe frequency locked at $|F=2\rangle \rightarrow |F'=3\rangle$ is shown in figure 5.5(b). The three Doppler broadened transmission peaks observed at pump detuning of -424 MHz , -267 MHz and 0 MHz are because of the velocity selective optical pumping of atoms with velocity component 330 m/s , 208 m/s , and 0 m/s respectively [141]. The transmission peak center at 0 MHz is accompanied by EIA at the center of the peak.

For comparison, we also recorded the spectrum for other two allowed transition i.e, $|F=2\rangle \rightarrow |F'=2\rangle$ and $|F=2\rangle \rightarrow |F'=1\rangle$. The recorded spectra are shown in figure 5.5 (b). As compare to $|F=2\rangle \rightarrow |F'=3\rangle$, the spectrum recorded for other two lock points ($|F=2\rangle \rightarrow |F'=2\rangle$ and $|F=2\rangle \rightarrow |F'=1\rangle$) shifts by 267 MHz and 424 MHz respectively (not shown in the figure). For all the lock points EIA width was found to be the same but variations were observed in the amplitude. Although the evaluated percentage absorption is the same and found to be approximately 45% . Percentage absorption,

defined by $\frac{A}{T} \times 100$, where A is the amplitude of EIA and T is that of transmission as shown in the inset of figure 5.6. The amplitude recorded for EIA is maximum for $|F=2\rangle \rightarrow |F'=3\rangle$ and minimum for $|F=2\rangle \rightarrow |F'=1\rangle$. The variation in amplitude is due to the following two reasons: First, $|F=2\rangle \rightarrow |F'=3\rangle$ transition being closed the loss of population to the uncoupled state will be negligible. Whereas, $|F=2\rangle \rightarrow |F'=2\rangle$ and $|F=2\rangle \rightarrow |F'=1\rangle$ being open transition the above mentioned loss would be more. Secondly, the transition strength also plays a significant role. The

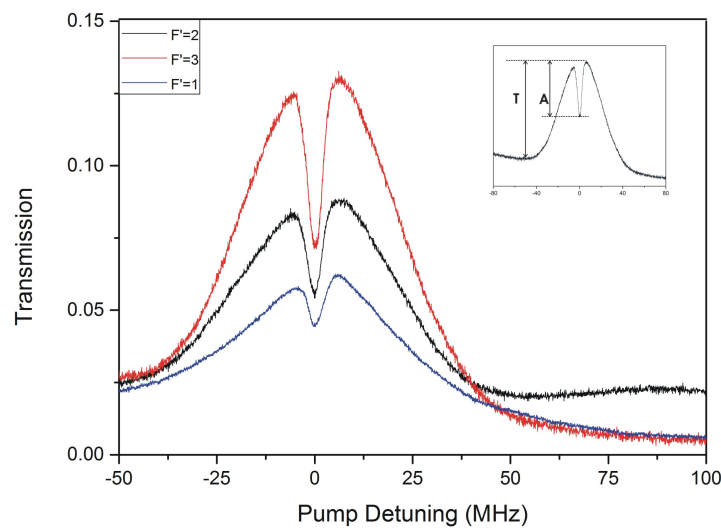


FIGURE 5.6: EIA for different lock points. Applied magnetic field $B = 0$ G. For each of the spectra recorded, the pump detuning axis is calibrated with respect to the lock point.

transition strength of $|F=2\rangle \rightarrow |F'=3\rangle$ is maximum and minimum for $|F=2\rangle \rightarrow |F'=1\rangle$. The overall transmission also follows the same pattern. As a result, the variation observed will be proportional to the EIA amplitude. Both of these variations ensure the percentage absorption remains the same for all lock points. But the percentage absorption depends on the pump power. For this we have recorded the transmission at different pump power for the lock point of $|F=2\rangle \rightarrow |F'=3\rangle$ and evaluated the percentage absorption as shown in figure 5.7 (a). As expected the percentage absorption increases with the increase in the pump power. And the similar trend was observed for the other lock point. The linewidth of EIA obtained, in this case, was ≈ 4.5 MHz which is subnatural (< 6 MHz). Usually, the linewidth varies with laser power. As shown in figure 5.7 (b), with the increase in laser power no significant changes are seen. Apart from power broadening the linewidth of EIA also depends on several other phenomena viz. Doppler effect, coherence

effect, etc. In this experiment, having DTLS system the laser is scanned around near to $|F' = 3\rangle$ state. As a result, the linewidth induced due to the Doppler effect gets limited. For the DTLS system, the change in the EIA linewidth with increasing pump power is negligibly small as shown in figure 5.7(b).

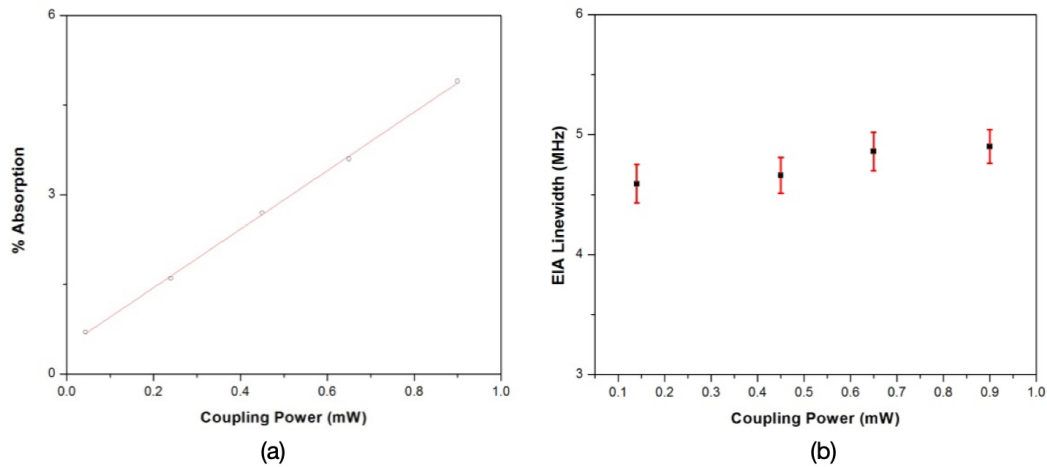


FIGURE 5.7: EIA properties for zero magnetic field.(a) Percentage absorption. (b) EIA linewidth vs pump power.

5.4.3 Non-zero magnetic field

We have carried out our experiment using ^{87}Rb D_2 line. As mentioned before in the presence of an external magnetic field, the hyperfine degeneracy uplift into magnetic sublevels. As a result, several transitions in the DTLS system get coupled to the pump and probe transition. For π polarised pump and σ polarised probe, $|F = 2\rangle \rightarrow |F' = 3\rangle$ splits into five pump and ten probe transitions, $|F = 2\rangle \rightarrow |F' = 2\rangle$ in five pump transitions and eight probe transition and $|F = 2\rangle \rightarrow |F' = 1\rangle$ into three pump and six probe transitions illustrated in A_1 , A_2 and A_3 respectively of figure 5.8. For σ^\pm polarised pump and π polarised probe, $|F = 2\rangle \rightarrow |F' = 3\rangle$ splits into ten pump and five probe transitions, $|F = 2\rangle \rightarrow |F' = 2\rangle$ in eight pump transitions and five probe transition and $|F = 2\rangle \rightarrow |F' = 1\rangle$ into six pump and three probe transitions illustrated in B_1 , B_2 and B_3 respectively of figure 5.8.

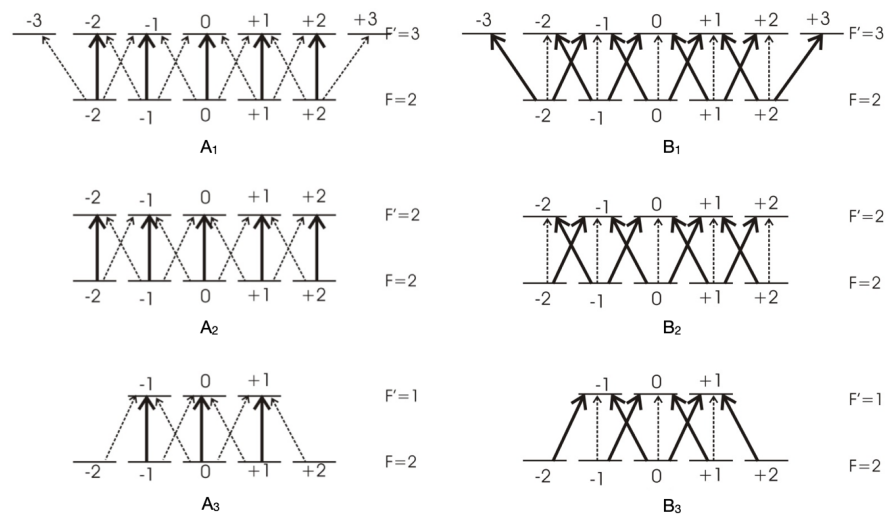


FIGURE 5.8: Level diagram illustrating all possible Zeeman transitions in presence of the transverse magnetic field. A₁, A₂ and A₃ represent Zeeman transitions corresponding to $|F = 2\rangle \rightarrow |F' = 3\rangle$, $|F = 2\rangle \rightarrow |F' = 2\rangle$ and $|F = 2\rangle \rightarrow |F' = 1\rangle$ respectively for π polarised pump field and B₁, B₂ and B₃ corresponding to σ polarised pump.

The dynamics of atomic population distribution depend on the polarisation of the driving field. In the case of σ^\pm polarised light atomic population is transferred to the state with the largest corresponding angular momentum. If we consider $|F = 2\rangle \rightarrow |F' = 3\rangle$ cyclic transition of ^{87}Rb , σ^+ field will transfer all the atomic population into $|F = 2, m_F = +2\rangle \rightarrow |F' = 3, m_{F'} = +3\rangle$ and σ^- field will transfer all the atomic population into $|F = 2, m_F = -2\rangle \rightarrow |F' = 3, m_{F'} = -3\rangle$ transition. The simultaneous presence of σ^+ and σ^- pump field leads to redistribution of the population instead of accumulating at the cyclic transition. Our study shall be limited to steady-state conditions. Population distribution is well affected and conditioned by transition strength and branching ratio between the states shown in (a) and (b) of figure 5.9. When the driving field is a π polarised light, atoms tend to accumulate near $m_F = 0$ [122]. Later the discussion of experimental results shows that population distribution is an important aspect in determining the positioning of EIA.

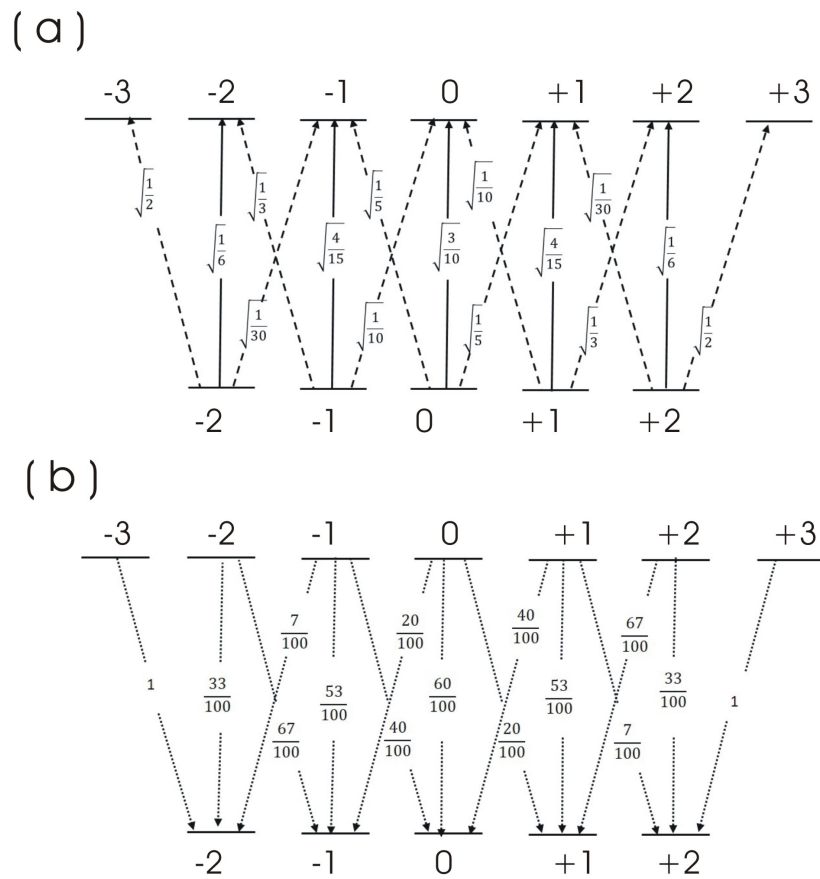


FIGURE 5.9: (a) Transition strength and (b) branching ratio - between different Zeeman sublevels corresponding hyperfine transition $F=2 \rightarrow F'=3$ to illustrate dynamics of the population distribution process.

π -polarized pump and σ -polarized probe field

The observed probe transmission for different magnetic fields is shown in figure 5.10. For $B = 0$ G, as expected a subnatural EIA dip is been observed at the center of the broad transmission peak. By increasing the magnetic field, the transmission peak broadens and the EIA peak splits into two. Split in the EIA peak is a well-studied phenomenon in the presence of a magnetic field (removal of hyperfine degeneracy). Till 10 G we observe two well-resolved EIA peaks superimposed on broad transmission. When the magnetic field reaches 20 G broad transmission splits into two well-resolved peaks separated by 38 MHz. Both transmission peaks have EIA dip superimposed on them partially detuned from the respective line center. On further increase in the

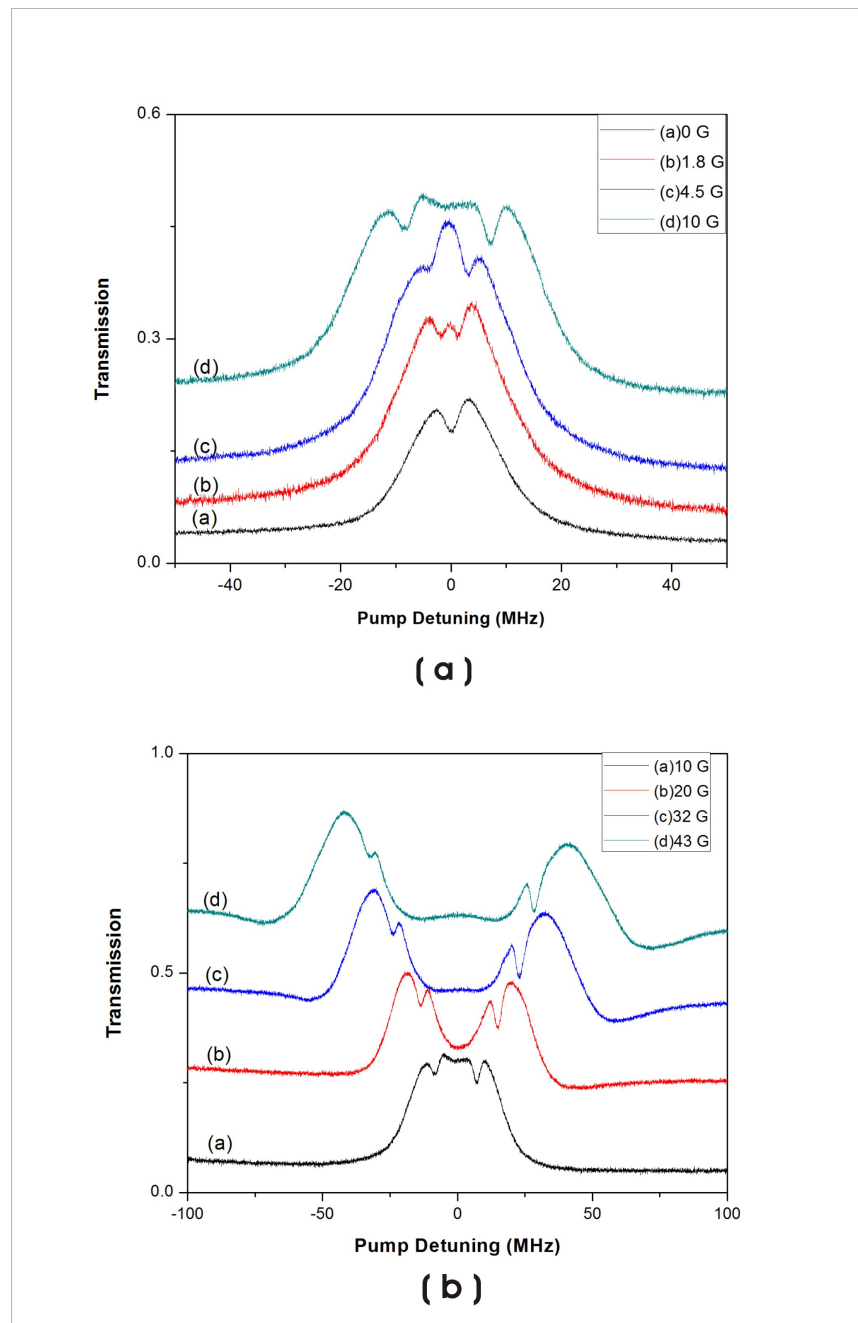


FIGURE 5.10: Experimentally observed probe transmission for different values of the magnetic field with π -polarized pump beam; (a) weak magnetic field, (b) strong magnetic field. The spectrum recorded for the fixed pump and probe intensity of 20 mW/cm^2 and 0.9 mW/cm^2 respectively.

magnetic field, two distinct spectral changes are seen. One, the separation between transmission peaks increases with magnetic field, and second EIA shifts towards zero pump detuning from the transmission peak.

In presence of the external magnetic field, atoms interacting with π -polarized pump and σ^\pm -polarized probe, a total of 8 N-type system is possible as shown in figure 5.11. Observation of two well-resolved transmission peaks with EIA dip suggests the presence of two distinct N-type systems out of an expected eight. This is attributed to the alignment of the population in ground state Zeeman sublevels and can be explained as follows: At 0 G, ground state Zeeman sublevel $m_F = 0$ would be maximally populated. As the magnetic field is applied the available population is redistributed over all the ground state Zeeman sublevels. The redistribution is decided by the polarization of the laser interacting with atoms. The energy level diagram for all possible transitions between Zeeman sublevels corresponding to $F = 2 \rightarrow F' = 3$ transition is shown in figure 5.11. As per the selection rule, in the presence of π -polarized strong pump beam, optical pumping of the atoms from $m_F = 0$ to $m_{F'} = 0$ will be favored. According to the branching ratio atoms pumped to $m_{F'}=0$ will decay back to $m_F=-1,0,+1$ with the probability of 20%, 60%, and 20% respectively. The probability of pumping the atoms back to $m_F = 0$ in presence of a weak σ^\pm -polarized probe beam would be minimum. 40% of the atoms pumped to $m_F = +1, -1$ would be revert back to $m_F = 0$ via $m_{F'} = +1, -1$ through spontaneous decay and 60 percent would be carried forward to higher magnetic sublevels. 67 % of the atoms pumped to $m_F = -2, +2$ would also populate $m_F = -1, +1$. By following the combined action of pumping and spontaneous decay the population will redistribute in $m_F = -2, -1, 0, +1, +2$ with $m_F = -1, +1$ being more populated as compared to $m_F = 0$ and $m_F = \pm 2$. This redistribution of the population will eventually give two well-resolved N-type systems involving the ground state coherence of $m_F = +1, +2$ and $m_F = -1, -2$ respectively as suggested by Zigdon *et al.* [142]. Although all N-type systems formed will have a contribution but being connected to cyclic transition $m_F = \pm 2 \rightarrow m_{F'} = \pm 3$, EIA due to ground state coherence of outermost Zeeman sublevels will have dominance. The N-system formed by the coherence of inner ground state Zeeman sublevels involving $m_F = 0, \pm 1$ will have more degree of openness as compared to the outer Zeeman sublevels and will have negligible effect. In these study we have discussed results

corresponding to hyperfine transition $|F = 2, m_F = +2\rangle \rightarrow |F' = 3, m_{F'} = +3\rangle$. Given the situation of the experiment, other transitions show similar results. Also, we have neglected the effect of the earth's magnetic field as it is extremely weak compared to the applied magnetic field.

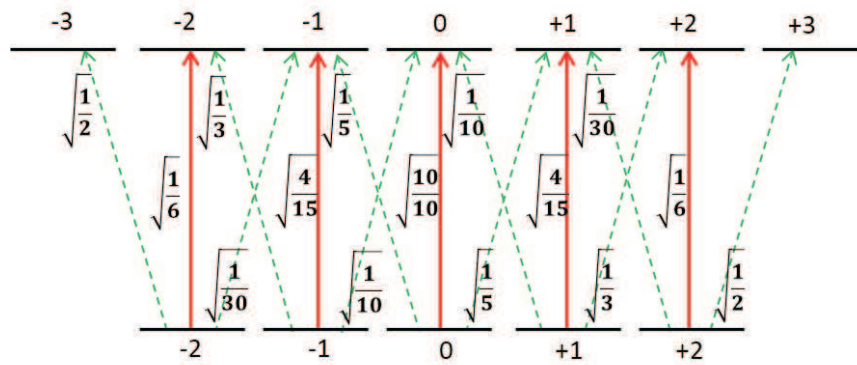


FIGURE 5.11: Energy level diagram showing all the possible Zeeman transitions with corresponding transition strength for π (solid red) and σ^\pm (dashed green) polarised beam.

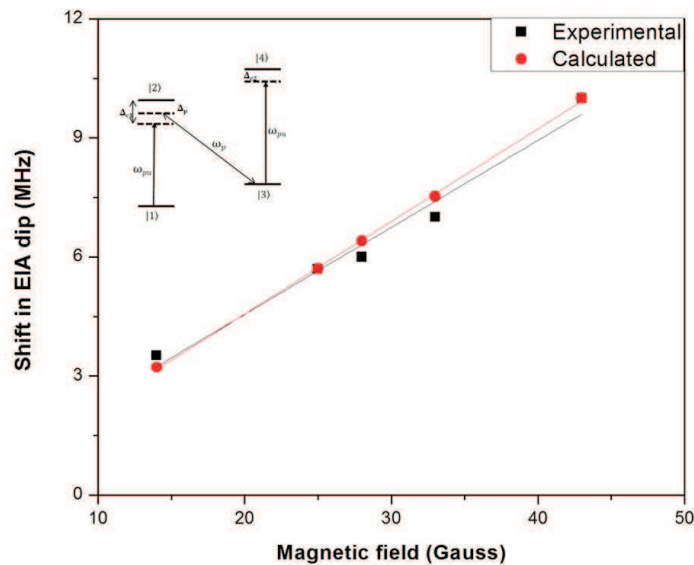


FIGURE 5.12: EIA shift from transmission as a function of applied magnetic field. In inset non-degenerate N-type system formed by π -polarized pump and σ^- -polarized probe. Δ_{C1} and Δ_{C2} are pump detuning and Δ_P is the probe detuning.

The shift observed in position of EIA with respect to the transmission peak is governed by three photon resonance [53]. In the case of co-propagating laser interacting with N-type system the shift, $\delta = \Delta_{C1} + \Delta_{C2} + \Delta_P$ where Δ_{C1} and Δ_{C2} are the detuning of pump and Δ_P for probe as

shown in inset of figure 5.12. The energy levels labeled as $|1\rangle$, $|3\rangle$ are for ground state and $|2\rangle$, $|4\rangle$ are for excited state. For simplicity, by assuming $\Delta_P = 0$ the shift observed will be equal to $\Delta_e - \Delta_g$, where $\Delta_g = (g_F \mu_B \mathbf{B}) / (2\pi \hbar)$ and $\Delta_e = (g_{F'} \mu_B \mathbf{B}) / (2\pi \hbar)$ are the Zeeman splitting for the ground state and excited state respectively [122] for neighbouring Zeeman sublevels. At 43 G, the calculated shift of EIA is found to be 10 MHz which is in agreement with the observed shift. The shift varies linearly with the magnetic field as shown in figure 5.12.

σ^\pm -polarized pump and π polarized probe field

To further investigate the effect of the applied magnetic field we change the orientation of the magnetic field. This leads to a change in the polarisation of the pump and probe field in the atomic frame of reference. Since light atom interaction, a resulting atomic transition is a polarization dependent the resultant spectrum is expected to change. Here, the magnetic field is oriented parallel to the electric field vector of the probe field making probe field π polarised and pump field σ^\pm .

The spectra recorded for the different magnetic fields are shown in figure 5.13. For weaker magnetic fields up to 10 G, the transmission profile observed is similar to the results discussed in Section 5.4.3. With the increase in the magnetic field, we observe EIA dip resolve into two. When measured at 13.5 G two EIA peaks are positioned at pump detuning of -7 MHz and +7 MHz and an absorption dip centered at zero pump detuning which gets enhanced with increase in the magnetic field. Since Zeeman splitting for the weak magnetic field are within the natural linewidth and any modifications because of the change in polarization will not be resolved. With further increase in the magnetic field, we observe a gradual decrease in transmission at the wings and an increase in the amplitude and broadness of absorption along with the shift of EIA peaks in the overall probe spectrum.

The basic difference in the observed spectrum for both the cases (when the pump is π polarized, the other when σ polarized) is due to the difference in possible population distribution. Optical pumping in the presence of a magnetic field with σ^+ -polarized pump and π -polarized probe for $F = 2 \rightarrow F' = 3$ is been studied and modeled using Bloch equations assuming a degenerate

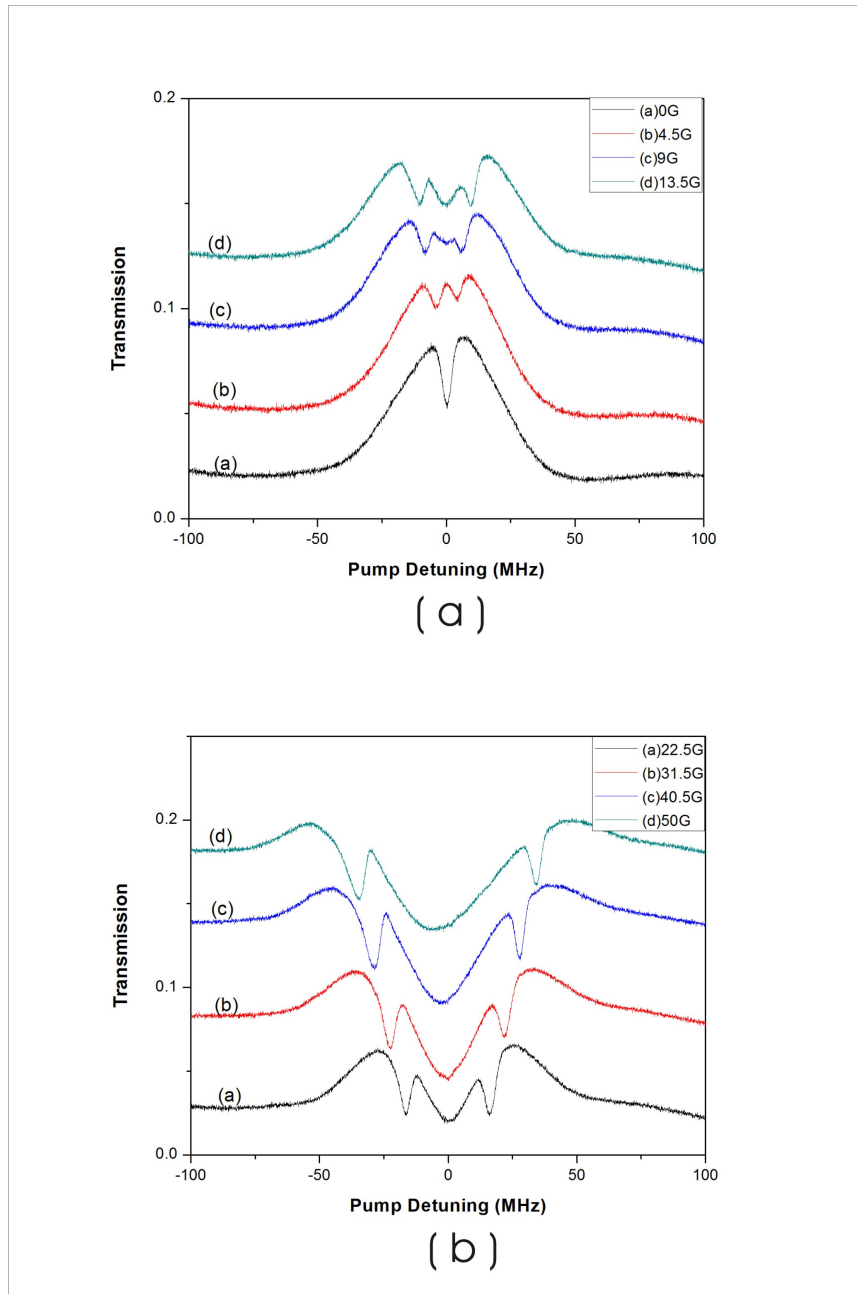


FIGURE 5.13: Experimentally observed probe transmission for different values of the magnetic field with π -polarized pump beam; (a) weak magnetic field, (b) strong magnetic field. The spectrum recorded for the fixed pump and probe intensity of 20 mW/cm^2 and 0.9 mW/cm^2 respectively.

two-level system by Zigdon *et al.* in [133] wherein it is suggested that the population will be swept to $m_F = 2$ state and all population will be concentrated in the N-type system at extreme right at the higher magnetic field. This is also evident from the transition strength and branching ratio of all possible transitions between Zeeman sublevels shown in figure 5.11. In our case, the simultaneous presence of σ^- polarization in the pump will act as re pumper and revert the population and populate $m_F = +1$, $m_F = 0$, and $m_F = -1$ Zeeman sublevels. The overall probe absorption will have a participation of $m_F = +1 \rightarrow m_{F'} = +1$ and $m_F = -1 \rightarrow m_{F'} = -1$ transitions along with $m_F = 0 \rightarrow m_{F'} = 0$ transition. Hence, broadness will increase with the increase in the magnetic field due to Zeeman splitting. A significant population available in $m_F = |2|$ for the probe to absorb will not allow the transmission to fully disappear. That is why we see the presence of weak transmission peaks at pump detuning of -37 MHz and +37 MHz at 40 G.

Effect of Intensity

Intensity plays an important role in defining the dynamics of the coherent interaction of light with atoms. The observed spectrum shows changes with the intensity of the pump field. For a fixed magnetic field of 40 G, the spectrum obtained for different pump intensities is shown in figure 5.14. By lowering the intensity, a gradual change of absorption to transmission at zero pump detuning can be seen. As pump intensity is lowered probability of repumping atoms back from $m_F = -2$ to $m_F = +2$ and vice versa becomes weak. Thus population available for absorption by π -polarised probe is diminished. However, this phenomenon is not observed in the case of π polarised pump. The population distribution, in this case, remains unchanged with intensity once the steady state is reached. At low pump field intensity, the Rabi frequency of pump and probe will become equal and the system will behave as a pure DTLs system, having one broad transmission in the observed probe spectra with EIA sitting at the line center. (not seen in our experiment)

The separation between EIA peaks with the magnetic field is found to be the same as the case discussed in section 5.4.3 which indicates that the main contribution of the same N-type systems

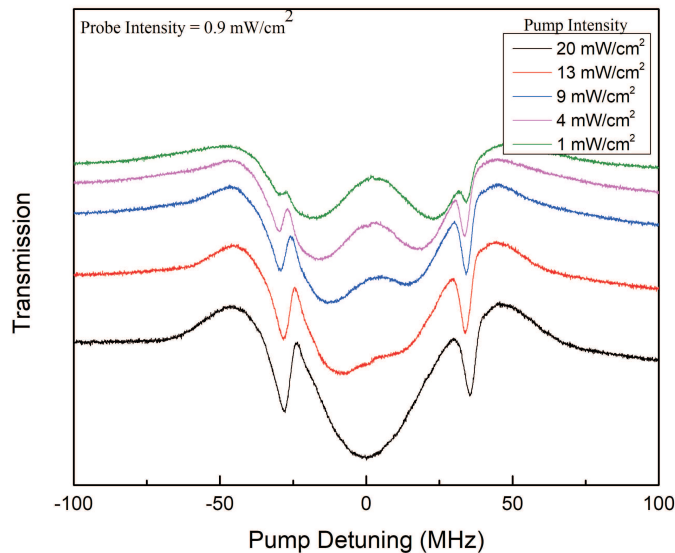


FIGURE 5.14: Transmission spectra were recorded for different values of pump intensity at a fixed transverse magnetic field of 40 G as a function of pump detuning. The spectrum recorded is for σ^\pm -polarized pump and π -polarized probe.

i.e N-type systems involving $m_F = |1\rangle, |2\rangle$ and $m_{F'} = |1\rangle, |2\rangle$ in the formation of EIA as suggested theoretically by Goren *et al.* in [131]. Contrary to the previous case, in this scheme, the EIA lineshape is symmetrical and broad. Both differences can be attributed to the simultaneous presence of σ^\pm -polarized pump. The simultaneous presence of both will have two effects (i) One of them will act as a repump for the N-system formed by others and will make the EIA line shape symmetrical [143] (ii) Both will facilitate two pumping channels from the same ground state and hence the degree of coherence will decrease and will broaden the EIA linewidth.

By lowering the intensity of the pump at a fixed magnetic field of 40 G as shown in figure 5.14 we observe a reduction in the amplitude of EIA. This is because as mentioned above pump becomes comparable to the probe the system will behave as a pure DTLS system and having two EIA peaks will not be favored. In figure 5.15, the variation in the linewidth of EIA with magnetic field is shown for π -polarized and σ^\pm -polarized pump. For π -polarized pump within the examined magnetic field the variation in linewidth is found to be within 1 MHz and for σ^\pm -polarized the variation is 2 MHz. It can also be seen that for all the examined magnetic

field linewidth of EIA observed for σ^\pm -polarized pump is approximately two times broader as compared to the π -polarized pump.

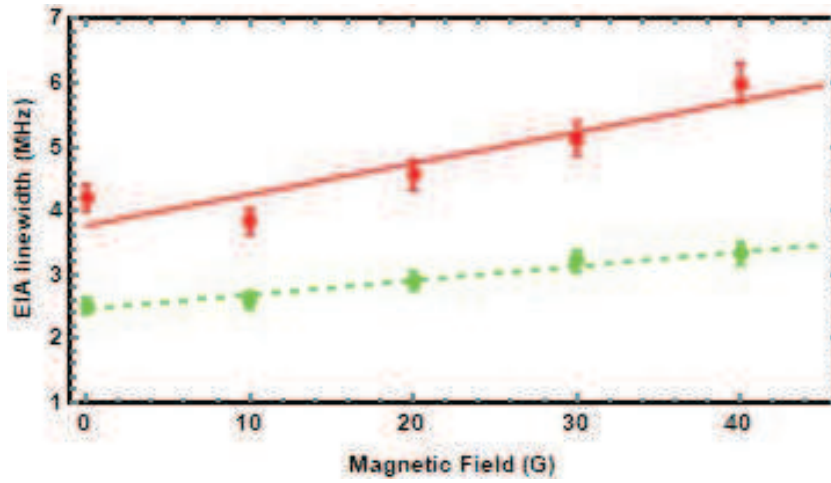


FIGURE 5.15: Measured EIA linewidth as a function for magnetic field for π -polarized pump (dash line) and for σ -polarized (solid line).

The effect of magnetic field on probe spectrum is taken into account through pump (Δ_{C1} and Δ_{C2}) and probe (Δ_P) detuning. The position of transmission spectrum is defined by $\delta = \Delta_{C1} + \Delta_{C2} + \Delta_P$ whereas that of EIA with respect to transmission peak is defined by $\Delta_{C2} - \Delta_{C1}$. The numerical calculation has been done for $v=0$. For all three probe transmission spectra shown in figure 5.16, $\Omega_p = 3MHz$ and $\Omega_{pu} = 5 \times \Omega_p$ and $\Gamma = 0.5 \times \Gamma_{sp}$, where $\Gamma_{sp} = 2\pi \times 6MHz$.

Figure 5.16 shows experimental (solid) and theoretical (dashed) probe transmission spectra with EIA dip sitting on it for three different magnetic field - (a) 20 G, (b) 30 G and (c) 40 G. The experimental transmission spectra for π -polarized pump and σ -polarized probe is found to be in good agreement with the theoretical spectra. Since, the doppler averging is neglected for theoretical spectra the EIA linewidth obtained is broader as compare to the experimental curve. The EIA observed in left and right of zero pump detuning are not symmetrical as compare to the theoretical curve. This can be attributed to the polarisation cleansing of the beam used in experiment

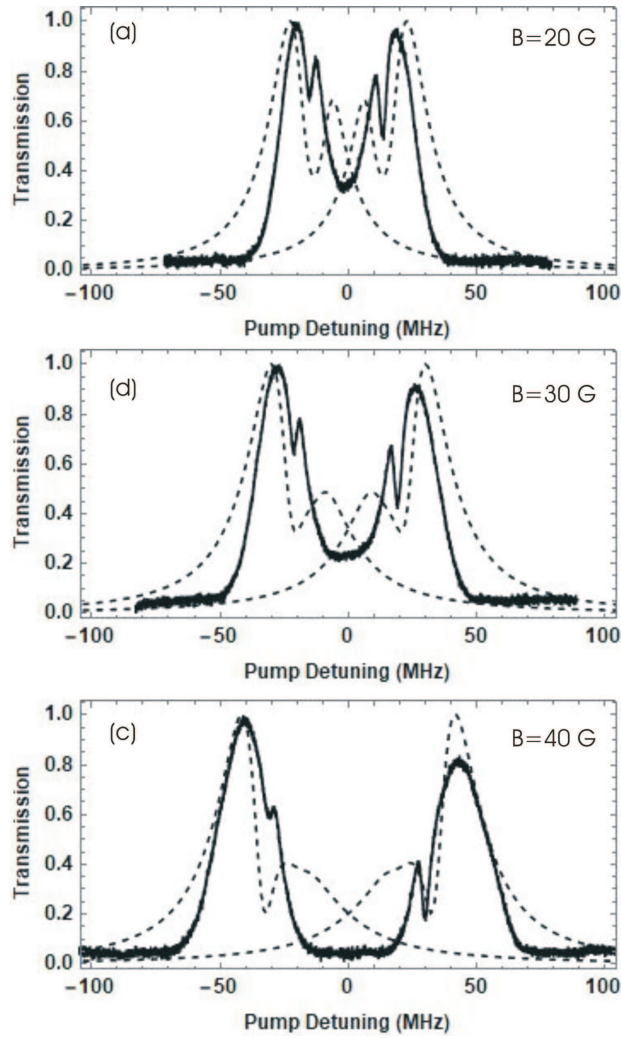


FIGURE 5.16: Theoretical (dashed) and experimental (solid) probe transmission spectra with EIA dip as a function of pump detuning for applied magnetic field of 20 G (a) , 30 G (b) and 40 G(c) .

5.4.4 Lande-g Factor

The value of Lande-g factor can be theoretically calculated using following analytical relation [122];

$$\begin{aligned}
 g_F &= g_J \frac{F(F+1) - I(I+1) + J(J+1)}{2F(F+1)} \\
 &+ g_I \frac{F(F+1) + I(I+1) - J(J+1)}{2F(F+1)}
 \end{aligned} \tag{5.5}$$

where F is the total angular atomic momentum quantum number defined by $F = J + I$. For ^{87}Rb , the numerical value of nuclear spin I is $\frac{3}{2}$ and that of total electronic angular momentum

quantum number J for lower $5^2S_{1/2}$ state is $\frac{1}{2}$ and for upper $5^2P_{3/2}$ state $\frac{3}{2}$ [122]. The theoretical value calculated using equation 5.5 is found to be 0.50 for the lower state and 0.66 for the upper state indicated by the straight line in figure 5.17 (b) and (c) respectively. The Lande-g factor of lower hyperfine level can be obtained experimentally by using the relation $g_{F'} = \frac{\hbar\Delta}{2\mu_B B}$, where Δ is measured peak-to-peak separation of EIA. The measured value of Δ at the different magnetic

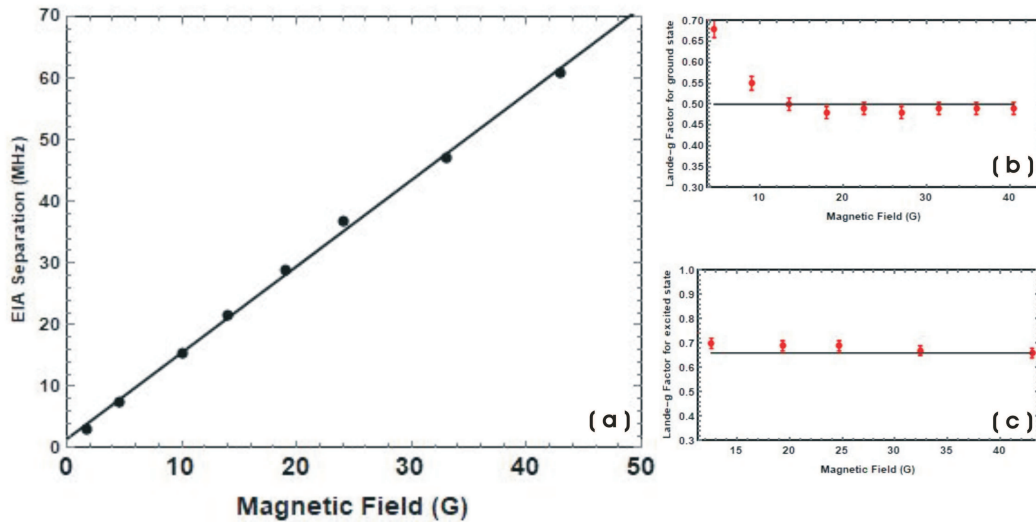


FIGURE 5.17: Measured EIA separation as a function of the magnetic field. The Lande-g factor for hyperfine ground states belonging to $5^2S_{1/2}$ (b). The Lande-g factor for hyperfine excited states belonging to $5^2P_{3/2}$ (c). In (b) and (c) solid line indicates theoretical g_F and $g_{F'}$ respectively

fields is shown in figure 5.17(a) and the observed variation is found to be linear with the magnetic field. The measured g_F value for different magnetic fields is shown in figure 5.17(b) and the average value obtained is 0.51 and found to agree with the theoretical value. For obtaining Lande-g factor for upper hyperfine states the separation between the transmission peak obtained with π polarized pump can be utilized by using the same relation as above and substituting Δ with the measured separation between the transmission peaks. This procedure is not possible at a lower magnetic field because transmission peaks are not resolved and the separation cannot be measured. For 10 G and above the transmission peaks get resolved and the separation can be measured. The experimentally observed $g_{F'}$ value for different magnetic fields is shown in figure 5.17(c). The average value is found to be 0.68 which is in theoretical agreement.

Chapter 6

Conclusion and outlook

EIT and EIA are important results of quantum coherence and interference between nearby states. EIT is a three-level phenomenon whereas EIA requires at least a four-level configuration. The interference between two states leads to dark states under certain circumstances. This leads to EIT which has been studied in detail for decades. We have extended this study to investigate the change in the spectrum and its characteristics in presence of the external magnetic field. We have applied the field in two possible directions - transverse and longitudinal. The polarization of the laser field in the atomic frame of reference depends on the direction of the magnetic. Therefore observed results exhibit change with change in direction of the applied magnetic field.

In chapter 1, we have discussed how laser interacts with two-level and three-level atomic system. For a two-level system, we have numerically discussed how the probability amplitude of each atomic states evolves in time. We have also discussed how the amplitude depends on laser detuning. For a three level system, we have numerically solved the density matrix equations and have discussed the condition for EIT.

In chapter 2, we have discussed the experimental setup in detail. The original elliptical profile of the laser beam has been circularised using an anamorphic prism pair. For locking of laser at a particular frequency, the SAS technique is used as a reference.

In chapter 3, the VSOP phenomenon is experimentally observed for different transitions of the $^{87}\text{Rb } D_2$ line. We have also discussed the effects of pump intensity and have optimised the condition at which EIT would be observed.

In chapter 4, we discussed in detail the effects of magnetic field on EIT. For the transverse magnetic field, irrespective of possible Λ configurations, we observe four EIT peaks. The positioning of each peak is defined by two-photon detuning. The separation between two consecutive peaks is observed to be twice the separation between Zeeman sublevels and increases linearly with the magnetic field. The amplitude of EIT peaks diminishes at first and gradually recovers, though not to the full strength, due to coherent population trapping by closely lying Zeeman states. With an increase in the magnetic field, the population initially trapped is released due to the decoherence effect. Apart from the change in position and amplitude, an increase in the applied magnetic field above 18 G leads to asymmetry in EIT peaks which increases with pump power. For higher magnetic fields and low pump and probe fields, asymmetry in the EIT profile becomes prominent. This is because the Zeeman sublevels from neighboring hyperfine states start participating. This observation is well explained with the theoretical description of the double- Λ system where two configurations with common ground states compete for dark and bright states. The values of impurity I_D given in Table 4.5 defines the degree of asymmetry in the spectrum. The overall process also depends largely on scattering rate and transition strength. Asymmetry can be controlled in two basic ways. One way is to control probe power and enhance the on-resonant process. The other more effective way is by using an anti-relaxation coated cell where the number of atoms participating in the off-resonant process can be drastically reduced.

The effect of longitudinal magnetic field on EIT is discussed in section 4.6. The EIT peak splits into three when the magnetic field is applied in the longitudinal direction. Unlike the EIT spectrum in presence of a transverse magnetic field, peaks in the longitudinal magnetic field are better resolved and symmetric. The linewidth of the EIT peaks reduces approximately by a factor of 2 when the applied magnetic field is increased from 0 G to 20 G. Unlike in the transverse magnetic field, no asymmetry is observed in the case of the longitudinal magnetic field. The reason is attributed to the uniform distribution of population and the absence of a double- Λ system.

The power broadening of the EIT linewidth shows dependence on the magnetic field. For 0G, linewidth increases by a factor of 3 whereas, for 22G it varies by a factor of approximately 1.5.

EIT can also be observed in a degenerate two-level system in presence of a magnetic field as discussed in section 4.7. The applied magnetic field makes it possible for Zeeman sublevels to form multiple Λ systems. The EIT peak observed, in this case, is an enhanced transmission peak sitting on top of the saturated transmission peak. The power broadening is negligible, however, the amplitude increases with pump power.

Chapter 5 is dedicated to discuss in detail all the aspects of EIA and its characteristic changes in presence of magnetic field. EIA is due to four level N configuration formed by Zeeman sublevels. The presence of coherence between two upper excited states leads to transfer of coherence to the ground state coherence, leading to absorption of probe field instead of a transmission. Therefore, TOC is the basic requirement for EIA. The nature of the observed EIA spectrum depends upon the polarisation of the pump field. For π -polarised pump, saturated transmission splits into two well-resolved transmission peaks, each carrying an EIA dip. However, in the case of σ polarised pump field, we observe enhanced absorption at the frequency center. The basic difference in the observed spectrum for both the cases (when the pump is π polarized, the other when σ polarized) is due to the difference in possible population distribution. With the increase in the magnetic field, the position of the EIA dip changes with respect to the frequency center of the transmission peak. The shift is defined by $\delta = \Delta_{C1} + \Delta_{C2} + \Delta_P$, where Δ_{C1} and Δ_{C2} are detuning of pump and Δ_P is that of probe. The position of EIA dips, therefore, depends upon the detuning value of the pump and the probe field in a given N system. The measured value of peak-to-peak separation between EIA peaks can be used to calculate the value of the Lande-g factor of the atomic medium as illustrated in section 5.4.4. The value obtained for ^{87}Rb used in our experiment is in good agreement with the calculated value. ’

This recent study of EIT in presence of a magnetic field as shown in this thesis can be further extended to understanding the dependence of other parameters on this phenomenon. Controlling the density of the atoms interacting with the laser field can further help in probing many other atomic systems. This can be possible by using a cell with an anti-relaxation coating or buffer

gas-filled cell. Also, this can pave a possible way for distinguishing the off-resonant and on-resonant velocity classes of atoms. It would also be interesting to verify the proposed four-level model with other atoms such as Cesium or Sodium. Controlling the direction of the magnetic field with respect to the electric field of the laser fields can also help in further understanding the observed asymmetrical lineshape. Also, controlling the number of off-resonant and on-resonant velocity classes of atoms by using an additional laser can be an interesting topic of research. The additional laser can form some other schemes such as an N-type system or a tripod system. In addition, changing the beam profile from a Gaussian mode to a non-Gaussian mode can be a fascinating topic of research in presence of a magnetic field. This can provide a method for tuning the effect of the nearby hyperfine levels on the resonant EIT phenomena. The measurement of the probe dispersion in addition to absorption measurement both in the hyperfine or Zeeman levels can also find potential applications in the field of quantum magnetometry or quantum memory in atomic vapor.

Appendix A

Appendix

Rubidium-87 D_2 Line Data

Our experiment is carried out in ^{87}Rb D_2 line which consists of two ground and four excited hyperfine states. This Appendix contains tables listing physical and optical properties of ^{87}Rb . It also notes transition strength factor between hyperfine states (Table A.3) as well as between magnetic sublevels (Table: A.4 - A.9).

Total atomic angular momentum F of the hyperfine state is given by $F=J+I$, where J and I are total electron momentum and nuclear angular momentum respectively. It can take value $|J-I| \leq F \leq |J+I|$.

In the experiments carried out in our study, we have used static magnetic field to lift the degeneracy of the hyperfine states. The separation between two consecutive magnetic states is given by

$$\Delta E = \mu_B g_F m_F B \quad (\text{A.1})$$

where,

$$g_F = \frac{F(F+1) - I(I+1) + J(J+1)}{2F(F+1)} \quad (\text{A.2})$$

TABLE A.1: Physical properties

Physical properties	Symbol	Numerical Values
Atomic Number	Z	37
Total Nucleons	Z+N	87
Relative Natural Abundance	η	27.83
Nucleon Lifetime	τ_n	4.88×10^{10} yr
Atomic Mass	m	1.4431×10^{-25}
Nuclear Spin	I	$\frac{3}{2}$

TABLE A.2: Optical Properties

Optical properties	Symbol	Numerical Values
Frequency	ω_0	$2\pi \times 384.230$ THz
Transition Energy	$\hbar\omega_0$	1.589049 eV
Wavelength	λ	780 nm
Wave Number	$\frac{k_n}{2\pi}$	12816.54 cm ⁻¹
Lifetime	τ	26.234 ns
Decay Rate	Γ	38.117×10^{-6} s ⁻¹
Natural Line Width		$2\pi \times 6.066$ MHz

TABLE A.3: Relative hyperfine transition strength factors for D_2 line

Transition		Transition Strength Factor
$ F = 2\rangle \rightarrow F' = 3\rangle$	S_{23}	7/10
$ F = 2\rangle \rightarrow F' = 2\rangle$	S_{22}	1/4
$ F = 2\rangle \rightarrow F' = 1\rangle$	S_{21}	1/20
$ F = 1\rangle \rightarrow F' = 2\rangle$	S_{12}	5/12
$ F = 1\rangle \rightarrow F' = 1\rangle$	S_{11}	5/12
$ F = 1\rangle \rightarrow F' = 0\rangle$	S_{10}	1/6

TABLE A.4: Hyperfine Dipole Matrix element for σ^+ transition ($F = 2, m_F \rightarrow F', m_{F'} = m_F + 1$)

	$m_F=-2$	$m_F=-1$	$m_F=0$	$m_F=+1$	$m_F=+2$
$F' = 3$	$\sqrt{1/30}$	$\sqrt{1/10}$	$\sqrt{1/5}$	$\sqrt{1/3}$	$\sqrt{1/2}$
$F' = 2$	$\sqrt{1/12}$	$\sqrt{1/8}$	$\sqrt{1/8}$	$\sqrt{1/2}$	
$F' = 1$	$\sqrt{1/20}$	$\sqrt{1/40}$	$\sqrt{1/120}$		

TABLE A.5: Hyperfine Dipole Matrix element for π transition ($F = 2, m_F \rightarrow F', m_{F'} = m_F$)

	$m_F=-2$	$m_F=-1$	$m_F=0$	$m_F=+1$	$m_F=+2$
$F' = 3$	$-\sqrt{1/6}$	$-\sqrt{4/15}$	$-\sqrt{3/10}$	$-\sqrt{4/15}$	$-\sqrt{1/6}$
$F' = 2$	$-\sqrt{1/6}$	$-\sqrt{1/24}$		$\sqrt{1/24}$	$\sqrt{1/6}$
$F' = 1$		$\sqrt{1/40}$	$\sqrt{1/30}$	$\sqrt{1/40}$	

TABLE A.6: Hyperfine Dipole Matrix element for σ^- transition ($F = 2, m_F \rightarrow F', m_{F'} = m_F - 1$)

	$\mathbf{m}_F=-2$	$\mathbf{m}_F=-1$	$\mathbf{m}_F=0$	$\mathbf{m}_F=+1$	$\mathbf{m}_F=+2$
$F' = 3$	$\sqrt{1/2}$	$\sqrt{1/3}$	$\sqrt{1/5}$	$\sqrt{1/10}$	$\sqrt{1/30}$
$F' = 2$		$-\sqrt{1/12}$	$-\sqrt{1/8}$	$-\sqrt{1/8}$	$\sqrt{1/12}$
$F' = 1$			$\sqrt{1/120}$	$\sqrt{1/40}$	$\sqrt{1/120}$

TABLE A.7: Hyperfine Dipole Matrix element for σ^+ transition ($F = 1, m_F \rightarrow F', m_{F'} = m_F + 1$)

	$\mathbf{m}_F=-1$	$\mathbf{m}_F=0$	$\mathbf{m}_F=+1$
$F' = 2$	$\sqrt{1/24}$	$\sqrt{1/8}$	$\sqrt{1/4}$
$F' = 1$	$\sqrt{5/24}$	$\sqrt{5/24}$	
$F' = 1$	$\sqrt{1/6}$		

TABLE A.8: Hyperfine Dipole Matrix element for π transition ($F = 1, m_F \rightarrow F', m_{F'} = m_F$)

	$\mathbf{m}_F=-1$	$\mathbf{m}_F=0$	$\mathbf{m}_F=+1$
$F' = 2$	$-\sqrt{1/8}$	$\sqrt{1/6}$	$-\sqrt{1/8}$
$F' = 1$	$-\sqrt{5/24}$	0	$\sqrt{5/24}$
$F' = 1$		$\sqrt{1/6}$	

TABLE A.9: Hyperfine Dipole Matrix element for σ^- transition ($F = 1, m_F \rightarrow F', m_{F'} = m_F - 1$)

	$\mathbf{m}_F=-1$	$\mathbf{m}_F=0$	$\mathbf{m}_F=+1$
$F' = 2$	$\sqrt{1/4}$	$\sqrt{1/8}$	$\sqrt{1/24}$
$F' = 1$		$-\sqrt{5/24}$	$-\sqrt{5/24}$
$F' = 1$			$\sqrt{1/6}$

Bibliography

- [1] John Weiner, Ping-Tong Ho, and Kay C Dee. *Light-matter interaction: fundamentals and applications*, volume 1. Wiley Online Library, 2003.
- [2] Tao E Li, Hsing-Ta Chen, and Joseph E Subotnik. Comparison of different classical, semiclassical, and quantum treatments of light–matter interactions: Understanding energy conservation. *Journal of Chemical Theory and Computation*, 15(3):1957–1973, 2019.
- [3] PW Werle, P Mazzinghi, F D’Amato, M De Rosa, K Maurer, and F Slemr. Signal processing and calibration procedures for in situ diode-laser absorption spectroscopy. *Spectrochimica Acta Part A: Molecular and Biomolecular Spectroscopy*, 60(8-9):1685–1705, 2004.
- [4] HI Schiff, GI Mackay, and J Bechara. The use of tunable diode laser absorption spectroscopy for atmospheric measurements. *Research on chemical intermediates*, 20:525–556, 1994.
- [5] AW Mantz. A review of the applications of tunable diode laser spectroscopy at high sensitivity. *Microchemical journal*, 50(3):351–364, 1994.
- [6] Ayan Banerjee and Vasant Natarajan. Saturated-absorption spectroscopy: eliminating crossover resonances by use of copropagating beams. *Optics letters*, 28(20):1912–1914, 2003.
- [7] Paul Siddons, Charles S Adams, Chang Ge, and Ifan G Hughes. Absolute absorption on rubidium d lines: comparison between theory and experiment. *Journal of Physics B: Atomic, Molecular and Optical Physics*, 41(15):155004, 2008.

-
- [8] Wolfgang Demtröder. *Laser spectroscopy*, volume 2. Springer, 1982.
- [9] Daryl W Preston. Doppler-free saturated absorption: Laser spectroscopy. *American Journal of Physics*, 64(11):1432–1436, 1996.
- [10] Samuel A Meek, Arthur Hipke, Guy Guelachvili, Theodor W Hänsch, and Nathalie Picqué. Doppler-free fourier transform spectroscopy. *Optics Letters*, 43(1):162–165, 2018.
- [11] S Dangel and R Holzner. Semiclassical theory for the interaction dynamics of laser light and sodium atoms including the hyperfine structure. *Physical Review A*, 56(5):3937, 1997.
- [12] JWR Tabosa and DV Petrov. Optical pumping of orbital angular momentum of light in cold cesium atoms. *Physical review letters*, 83(24):4967, 1999.
- [13] Thomas M Spinka. *Nonlinear optical processes and the nearest neighbor distribution in rubidium vapor*. University of Illinois at Urbana-Champaign, 2010.
- [14] KB MacAdam, A Steinbach, and Carl Wieman. A narrow-band tunable diode laser system with grating feedback, and a saturated absorption spectrometer for cs and rb. *American Journal of Physics*, 60(12):1098–1111, 1992.
- [15] Hui Yan, Kai-Yu Liao, Jian-Feng Li, Yan-Xiong Du, Zhi-Ming Zhang, and Shi-Liang Zhu. Bichromatic electromagnetically induced transparency in hot atomic vapors. *Physical Review A*, 87(5):055401, 2013.
- [16] Shanchao Zhang, Shuyu Zhou, Michael MT Loy, George Ke Lun Wong, and Shengwang Du. Optical storage with electromagnetically induced transparency in a dense cold atomic ensemble. *Optics letters*, 36(23):4530–4532, 2011.
- [17] Charles S Adams, Jonathan D Pritchard, and James P Shaffer. Rydberg atom quantum technologies. *Journal of Physics B: Atomic, Molecular and Optical Physics*, 53(1):012002, 2019.
- [18] Mark Saffman. Quantum computing with atomic qubits and rydberg interactions: progress and challenges. *Journal of Physics B: Atomic, Molecular and Optical Physics*, 49(20):202001, 2016.

- [19] H el ene Perrin. Ultra cold atoms and bose-einstein condensation for quantum metrology. *The European Physical Journal Special Topics*, 172(1):37–55, 2009.
- [20] Dmitry Budker and Michael Romalis. Optical magnetometry. *Nature physics*, 3(4):227–234, 2007.
- [21] Christian L Degen, Friedemann Reinhard, and Paola Cappellaro. Quantum sensing. *Reviews of modern physics*, 89(3):035002, 2017.
- [22] F Yu Wu, S Ezekiel, M Ducloy, and BR Mollow. Observation of amplification in a strongly driven two-level atomic system at optical frequencies. *Physical Review Letters*, 38(19):1077, 1977.
- [23] A Lipsich, S Barreiro, AM Akulshin, and A Lezama. Absorption spectra of driven degenerate two-level atomic systems. *Physical Review A*, 61(5):053803, 2000.
- [24] RE Slusher and HM Gibbs. Self-induced transparency in atomic rubidium. *Physical Review A*, 5(4):1634, 1972.
- [25] Wesley W Erickson. *Electromagnetically Induced Transparency*. PhD thesis, Reed College, 2012.
- [26] BJ Dalton, R McDuff, and PL Knight. Coherent population trapping. *Optica Acta: International Journal of Optics*, 32(1):61–70, 1985.
- [27] G Orriols et al. Nonabsorption resonances by nonlinear coherent effects in a three-level system. *Nuovo Cimento B, Serie 11*, 53:1–24, 1979.
- [28] Ennio Arimondo. Relaxation processes in coherent-population trapping. *Physical Review A*, 54(3):2216, 1996.
- [29] O Schmidt, R Wynands, Z Hussein, and D Meschede. Steep dispersion and group velocity below $c/3000$ in coherent population trapping. *Physical Review A*, 53(1):R27, 1996.
- [30] J Mompert and R Corbalan. Lasing without inversion. *Journal of Optics B: Quantum and Semiclassical Optics*, 2(3):R7, 2000.

- [31] Marlan O Scully, Shi-Yao Zhu, and Athanasios Gavrielides. Degenerate quantum-beat laser: Lasing without inversion and inversion without lasing. *Physical review letters*, 62(24):2813, 1989.
- [32] Yifu Zhu. Lasing without inversion in a closed three-level system. *Physical Review A*, 45(9):R6149, 1992.
- [33] Yong-qing Li and Min Xiao. Enhancement of nondegenerate four-wave mixing based on electromagnetically induced transparency in rubidium atoms. *Optics letters*, 21(14):1064–1066, 1996.
- [34] Ryan M Camacho, Praveen K Vudiyasetu, and John C Howell. Four-wave-mixing stopped light in hot atomic rubidium vapour. *Nature Photonics*, 3(2):103–106, 2009.
- [35] CF McCormick, Vincent Boyer, Ennio Arimondo, and PD Lett. Strong relative intensity squeezing by four-wave mixing in rubidium vapor. *Optics letters*, 32(2):178–180, 2007.
- [36] Girish S Agarwal and Sumei Huang. Electromagnetically induced transparency in mechanical effects of light. *Physical Review A*, 81(4):041803, 2010.
- [37] Stephen E Harris, JE Field, and A Imamoglu. Nonlinear optical processes using electromagnetically induced transparency. *Physical Review Letters*, 64(10):1107, 1990.
- [38] Michael Fleischhauer, Atac Imamoglu, and Jonathan P Marangos. Electromagnetically induced transparency: Optics in coherent media. *Reviews of modern physics*, 77(2):633, 2005.
- [39] Ying Gu, Lei Wang, Kai Wang, Cheng Yang, and Qihuang Gong. Coherent population trapping and electromagnetically induced transparency in a five-level m-type atom. *Journal of Physics B: Atomic, Molecular and Optical Physics*, 39(3):463, 2005.
- [40] Kyoungdae Kim, M Kwon, HD Park, HS Moon, HS Rawat, K An, and JB Kim. Electromagnetically induced absorption spectra depending on intensities and detunings of the coupling field in cs vapour. *Journal of Physics B: Atomic, Molecular and Optical Physics*, 34(23):4801, 2001.

- [41] H Failache, P Valente, G Ban, V Lorent, and A Lezama. Inhibition of electromagnetically induced absorption due to excited-state decoherence in rb vapor. *Physical Review A*, 67(4):043810, 2003.
- [42] AM Akulshin, S Barreiro, and A Lezama. Electromagnetically induced absorption and transparency due to resonant two-field excitation of quasidegenerate levels in rb vapor. *Physical Review A*, 57(4):2996, 1998.
- [43] DV Brazhnikov, AV Taichenachev, AM Tumaikin, and VI Yudin. Electromagnetically-induced-absorption resonance with high contrast and narrow width in the hanle configuration. *Laser Physics Letters*, 11(12):125702, 2014.
- [44] W Ace Furman. *Electromagnetically induced transparency: The zeeman method*. PhD thesis, Reed College, 2016.
- [45] A Lezama, S Barreiro, and AM Akulshin. Electromagnetically induced absorption. *Physical Review A*, 59(6):4732, 1999.
- [46] Soo Kyoung Kim, Han Seb Moon, Kyoungdae Kim, and Jung Bog Kim. Observation of electromagnetically induced absorption in open systems regardless of angular momentum. *Physical Review A*, 68(6):063813, 2003.
- [47] In-Ho Bae and Han Seb Moon. Continuous control of light group velocity from subluminal to superluminal propagation with a standing-wave coupling field in a rb vapor cell. *Physical Review A*, 83(5):053806, 2011.
- [48] GS Agarwal, Tarak Nath Dey, and Sunish Menon. Knob for changing light propagation from subluminal to superluminal. *Physical Review A*, 64(5):053809, 2001.
- [49] Martin Mücke, Eden Figueroa, Joerg Bochmann, Carolin Hahn, Karim Murr, Stephan Ritter, Celso J Villas-Boas, and Gerhard Rempe. Electromagnetically induced transparency with single atoms in a cavity. *Nature*, 465(7299):755–758, 2010.
- [50] MD Lukin and Ataç Imamoğlu. Controlling photons using electromagnetically induced transparency. *Nature*, 413(6853):273–276, 2001.

- [51] A Nicolas, L Veissier, L Giner, E Giacobino, D Maxein, and J Laurat. A quantum memory for orbital angular momentum photonic qubits. *Nature Photonics*, 8(3):234–238, 2014.
- [52] K-J Boller, A Imamoglu, and Stephen E Harris. Observation of electromagnetically induced transparency. *Physical Review Letters*, 66(20):2593, 1991.
- [53] Kanhaiya Pandey. Role of different types of subsystems in a doubly driven λ system in ^{87}Rb . *Physical Review A*, 87(4):043838, 2013.
- [54] Lene Vestergaard Hau, Stephen E Harris, Zachary Dutton, and Cyrus H Behroozi. Light speed reduction to 17 metres per second in an ultracold atomic gas. *Nature*, 397(6720):594–598, 1999.
- [55] Michael M Kash, Vladimir A Sautenkov, Alexander S Zibrov, Leo Hollberg, George R Welch, Mikhail D Lukin, Yuri Rostovtsev, Edward S Fry, and Marlan O Scully. Ultraslow group velocity and enhanced nonlinear optical effects in a coherently driven hot atomic gas. *Physical Review Letters*, 82(26):5229, 1999.
- [56] Kevin Cox, Valery I Yudin, Alexey V Taichenachev, Irina Novikova, and Eugeni E Mikhailov. Measurements of the magnetic field vector using multiple electromagnetically induced transparency resonances in ^{87}Rb vapor. *Physical Review A*, 83(1):015801, 2011.
- [57] VI Yudin, AV Taichenachev, YO Dudin, VL Velichansky, AS Zibrov, and SA Zibrov. Vector magnetometry based on electromagnetically induced transparency in linearly polarized light. *Physical Review A*, 82(3):033807, 2010.
- [58] Jason Clarke, Hongxin Chen, and William A van Wijngaarden. Electromagnetically induced transparency and optical switching in a rubidium cascade system. *Applied Optics*, 40(12):2047–2051, 2001.
- [59] Meng-Jung Lee, Yi-Hsin Chen, I-Chung Wang, and A Yu Ite. Eit-based all-optical switching and cross-phase modulation under the influence of four-wave mixing. *Optics express*, 20(10):11057–11063, 2012.

- [60] Mostafa Sahrai, Habib Tajalli, Kishore T Kapale, and M Suhail Zubairy. Tunable phase control for subluminal to superluminal light propagation. *Physical Review A*, 70(2):023813, 2004.
- [61] Sapam Ranjita Chanu, Kanhaiya Pandey, and Vasant Natarajan. Conversion between electromagnetically induced transparency and absorption in a three-level lambda system. *EPL (Europhysics Letters)*, 98(4):44009, 2012.
- [62] Thai Doan Thanh, Nguyen Tuan Anh, Nguyen Thi Thu Hien, Hoang Minh Dong, Nguyen Xuan Hao, Dinh Xuan Khoa, and Nguyen Huy Bang. Subluminal and superluminal light pulse propagation under external magnetic field in a vee-type three-level atomic medium. *Photonics Letters of Poland*, 13(1):4–6, 2021.
- [63] Syed Muhammad Arif, Bakht Amin Bacha, Umer Wahid, Muhammad Haneef, and Arif Ullah. Tunable subluminal to superluminal propagation via spatio-temporal solitons by application of laguerre fields intensities. *Physics Letters A*, 388:127041, 2021.
- [64] Paul Siddons, Charles S Adams, and Ifan G Hughes. Optical control of faraday rotation in hot rb vapor. *Physical review A*, 81(4):043838, 2010.
- [65] Gang Wang, Yu-Sheng Wang, Emily Kay Huang, Weilun Hung, Kai-Lin Chao, Ping-Yeh Wu, Yi-Hsin Chen, and Ite A Yu. Ultranarrow-bandwidth filter based on a thermal eit medium. *Scientific Reports*, 8(1):1–7, 2018.
- [66] Yun Xiao, Xu-Bo Zou, Wei Jiang, You-Ling Chen, and Guang-Can Guo. Analog to multiple electromagnetically induced transparency in all-optical drop-filter systems. *Physical Review A*, 75(6):063833, 2007.
- [67] Hua Lu, Xueming Liu, Guoxi Wang, and Dong Mao. Tunable high-channel-count band-pass plasmonic filters based on an analogue of electromagnetically induced transparency. *Nanotechnology*, 23(44):444003, 2012.

- [68] Zhiming Tao, Mengzhi Chen, Zifa Zhou, Biaoliang Ye, Jianhua Zeng, and Hepeng Zheng. Isotope ^{87}Rb Faraday filter with a single transmission peak resonant with atomic transition at 780 nm. *Optics Express*, 27(9):13142–13149, 2019.
- [69] Claude Cohen-Tannoudji, Jacques Dupont-Roc, and Gilbert Grynberg. *Atom-photon interactions: basic processes and applications*. John Wiley & Sons, 1998.
- [70] Peter W Milonni and Joseph H Eberly. *Laser physics*. John Wiley & Sons, 2010.
- [71] Michel Pinard, CG Aminoff, and Franck Laloë. Velocity-selective optical pumping and Doppler-free spectroscopy. *Physical Review A*, 19(6):2366, 1979.
- [72] Carl Gustav Aminoff and M Pinard. Velocity selective optical pumping. *Journal de Physique*, 43(2):263–277, 1982.
- [73] Carl Gustav Aminoff, Juha Javanainen, and Matti Kaivola. Collision effects in velocity-selective optical pumping of sodium. *Physical Review A*, 28(2):722, 1983.
- [74] Alessandro Cere, Valentina Parigi, Marta Abad, Florian Wolfgramm, Ana Predojević, and Morgan W Mitchell. Narrowband tunable filter based on velocity-selective optical pumping in an atomic vapor. *Optics Letters*, 34(7):1012–1014, 2009.
- [75] JE Bjorkholm, PF Liao, and A Wokaun. Distortion of on-resonance two-photon spectroscopic line shapes caused by velocity-selective optical pumping. *Physical Review A*, 26(5):2643, 1982.
- [76] Hong Cheng, Han-Mu Wang, Shan-Shan Zhang, Pei-Pei Xin, Jun Luo, and Hong-Ping Liu. Electromagnetically induced transparency of ^{87}Rb in a buffer gas cell with magnetic field. *Journal of Physics B: Atomic, Molecular and Optical Physics*, 50(9):095401, 2017.
- [77] Shrabana Chakrabarti, Amitkiran Pradhan, Biswajit Ray, and Pradip N Ghosh. Velocity selective optical pumping effects and electromagnetically induced transparency for d_2 transitions in rubidium. *Journal of Physics B: Atomic, Molecular and Optical Physics*, 38(23):4321, 2005.

- [78] SM Iftiqar, GR Karve, and Vasant Natarajan. Subnatural linewidth for probe absorption in an electromagnetically-induced-transparency medium due to doppler averaging. *Physical Review A*, 77(6):063807, 2008.
- [79] Hafeez Ur Rehman, Heung-Ryoul Noh, and Jin-Tae Kim. Velocity selective optical pumping effects on 85rb atoms from various coupling beam polarization configurations. *Optics Communications*, 402:567–571, 2017.
- [80] Sung Jong Park, Hyuck Cho, Ho Seong Lee, and Jong Dae Park. Velocity-selective-optical-pumping spectroscopy of the 87 rb d 2 line by using two copropagating laser beams. *Journal of the Korean Physical Society*, 33(3):281–287, 1998.
- [81] Hong Cheng, Shan-Shan Zhang, Pei-Pei Xin, Yuan Cheng, and Hong-Ping Liu. Theoretical simulation of 87rb absorption spectrum in a thermal cell. *Chinese Physics B*, 25(11):114203, 2016.
- [82] David J Fulton, Sara Shepherd, Richard R Moseley, Bruce D Sinclair, and Malcolm H Dunn. Continuous-wave electromagnetically induced transparency: A comparison of ν , λ , and cascade systems. *Physical Review A*, 52(3):2302, 1995.
- [83] AD Sargsyan, GT Hakhumyan, and DH Sarkisyan. Use of sub-doppler optical resonances for measurement of weak magnetic fields by means of extremely thin rubidium vapor cell. *Journal of Contemporary Physics (Armenian Academy of Sciences)*, 47:64–72, 2012.
- [84] BS Mathur, H Tang, and W Happer. Light shifts in the alkali atoms. *Physical Review*, 171(1):11, 1968.
- [85] Xiaoyan Liu, Xu Zhao, Zhen Xu, and Zhengfeng Hu. Light-shift comparison of electromagnetically induced transparency and coherent population trapping in continuous-wave and ramsey spectroscopies. *JOSA B*, 38(4):1270–1275, 2021.
- [86] S Wielandy and Alexander L Gaeta. Investigation of electromagnetically induced transparency in the strong probe regime. *Physical Review A*, 58(3):2500, 1998.

- [87] Angelos Lazoudis, Teodora Kirova, EH Ahmed, Peng Qi, John Huennekens, and AM Lyyra. Electromagnetically induced transparency in an open v-type molecular system. *Physical Review A*, 83(6):063419, 2011.
- [88] F Goldfarb, J Ghosh, M David, J Ruggiero, T Chanelière, J-L Le Gouët, H Gilles, R Ghosh, and F Bretenaker. Observation of ultra-narrow electromagnetically induced transparency and slow light using purely electronic spins in a hot atomic vapor. *Europhysics Letters*, 82(5):54002, 2008.
- [89] CY Ye and AS Zibrov. Width of the electromagnetically induced transparency resonance in atomic vapor. *Physical Review A*, 65(2):023806, 2002.
- [90] A Imamoğlu and Stephen E Harris. Lasers without inversion: interference of dressed lifetime-broadened states. *Optics letters*, 14(24):1344–1346, 1989.
- [91] Jonathan P Marangos. Electromagnetically induced transparency. *Journal of Modern Optics*, 45(3):471–503, 1998.
- [92] A Kasapi, Maneesh Jain, GY Yin, and Stephen E Harris. Electromagnetically induced transparency: propagation dynamics. *Physical review letters*, 74(13):2447, 1995.
- [93] MD Lukin and Ataç Imamoğlu. Controlling photons using electromagnetically induced transparency. *Nature*, 413(6853):273–276, 2001.
- [94] Joyee Ghosh, R Ghosh, F Goldfarb, J-L Le Gouët, and F Bretenaker. Analysis of electromagnetically induced transparency and slow light in a hot vapor of atoms undergoing collisions. *Physical Review A*, 80(2):023817, 2009.
- [95] Zong-Syun He, Jyh-Hung Tsai, Yung-Yung Chang, Chi-Chuan Liao, and Chin-Chun Tsai. Ladder-type electromagnetically induced transparency with optical pumping effect. *Physical Review A*, 87(3):033402, 2013.
- [96] Ying Wu and Xiaoxue Yang. Electromagnetically induced transparency in v-, λ -, and cascade-type schemes beyond steady-state analysis. *Physical Review A*, 71(5):053806, 2005.

- [97] Aleksandar J Krmpot, Marina M Mijailović, Bratimir M Panić, Dragan V Lukić, Aleksander G Kovačević, Dejan V Pantelić, and Branislav M Jelenković. Sub-doppler absorption narrowing in atomic vapor at two intense laser fields. *Optics Express*, 13(5): 1448–1456, 2005.
- [98] PRS Carvalho, Luís EE de Araujo, and JWR Tabosa. Angular dependence of an electromagnetically induced transparency resonance in a doppler-broadened atomic vapor. *Physical Review A*, 70(6):063818, 2004.
- [99] Mangesh Bhattarai, Vineet Bharti, Vasant Natarajan, Armen Sargsyan, and David Sarkisyan. Study of EIT resonances in an anti-relaxation coated Rb vapor cell. *Physics Letters A*, 383(1):91–96, 2019.
- [100] MD Lukin, M Fleischhauer, AS Zibrov, HG Robinson, VL Velichansky, Leo Hollberg, and MO Scully. Spectroscopy in dense coherent media: line narrowing and interference effects. *Physical review letters*, 79(16):2959, 1997.
- [101] D McGloin, MH Dunn, and DJ Fulton. Polarization effects in electromagnetically induced transparency. *Physical Review A*, 62(5):053802, 2000.
- [102] SM Iftiqar and Vasant Natarajan. Line narrowing of electromagnetically induced transparency in Rb with a longitudinal magnetic field. *Physical Review A*, 79(1):013808, 2009.
- [103] Charu Mishra, A Chakraborty, A Srivastava, SK Tiwari, SP Ram, VB Tiwari, and SR Mishra. Electromagnetically induced transparency in λ -systems of ⁸⁷Rb atom in magnetic field. *Journal of Modern Optics*, 65(20):2269–2277, 2018.
- [104] Xiao-Gang Wei, Jin-Hui Wu, Gui-Xia Sun, Zhuang Shao, Zhi-Hui Kang, Yun Jiang, and Jin-Yue Gao. Splitting of an electromagnetically induced transparency window of rubidium atoms in a static magnetic field. *Physical Review A*, 72(2):023806, 2005.
- [105] Yong-qing Li and Min Xiao. Electromagnetically induced transparency in a three-level λ -type system in rubidium atoms. *Physical Review A*, 51(4):R2703, 1995.

- [106] Hong Yuan Ling, Yong-Qing Li, and Min Xiao. Coherent population trapping and electromagnetically induced transparency in multi-zeeman-sublevel atoms. *Physical Review A*, 53(2):1014, 1996.
- [107] A Sargsyan, D Sarkisyan, Y Pashayan-Leroy, C Leroy, S Cartaleva, AD Wilson-Gordon, and M Auzinsh. Electromagnetically induced transparency resonances inverted in magnetic field. *Journal of Experimental and Theoretical Physics*, 121(6):966–975, 2015.
- [108] Sumanta Khan, Molahalli Panidhara Kumar, Vineet Bharti, and Vasant Natarajan. Coherent population trapping (cpt) versus electromagnetically induced transparency (eit). *The European Physical Journal D*, 71(2):1–9, 2017.
- [109] OS Mishina, M Scherman, P Lombardi, J Ortalo, D Felinto, AS Sheremet, A Bramati, DV Kupriyanov, J Laurat, and E Giacobino. Electromagnetically induced transparency in an inhomogeneously broadened λ transition with multiple excited levels. *Physical Review A*, 83(5):053809, 2011.
- [110] Zhuo Ren Chen and Xue Mei Su. Asymmetrical spectra due to atomic coherence of neighboring excited levels. *The European Physical Journal D*, 67(7):1–7, 2013.
- [111] Vineet Bharti and Ajay Wasan. Influence of multiple excited states on optical properties of an-type doppler-broadened system for the d2 line of alkali atoms. *Journal of Physics B: Atomic, Molecular and Optical Physics*, 46(12):125501, 2013.
- [112] Indra Hang Subba, Ranjit Kumar Singh, Nayan Sharma, Souvik Chatterjee, and Ajay Tripathi. Understanding asymmetry in electromagnetically induced transparency for 87rb in strong transverse magnetic field. *The European Physical Journal D*, 74(7):1–9, 2020.
- [113] Saesun Kim and Alberto M Marino. Effect of closely-spaced excited states on electromagnetically induced transparency. *OSA Continuum*, 4(12):3184–3203, 2021.
- [114] Michael Erhard and Hanspeter Helm. Buffer-gas effects on dark resonances: Theory and experiment. *Physical Review A*, 63(4):043813, 2001.

- [115] Michael Fleischhauer. Correlation of high-frequency phase fluctuations in electromagnetically induced transparency. *Physical review letters*, 72(7):989, 1994.
- [116] EA Korsunsky, Norbert Leinfellner, Arno Huss, S Balushev, and Laurentius Windholz. Phase-dependent electromagnetically induced transparency. *Physical Review A*, 59(3):2302, 1999.
- [117] Baodong Yang, Qiangbing Liang, Jun He, Tiancai Zhang, and Junmin Wang. Narrowlinewidth double-resonance optical pumping spectrum due to electromagnetically induced transparency in ladder-type inhomogeneously broadened media. *Physical Review A*, 81(4):043803, 2010.
- [118] Gordana Školnik, Nataša Vujičić, and Ticijana Ban. Optical pumping of the zeeman components in the rubidium vapor. *Optics Communications*, 282(7):1326–1334, 2009.
- [119] Arno Huss, Roland Lammegger, Laurentius Windholz, Emilia Alipieva, Sanka Gateva, Lubomir Petrov, Elena Taskova, and Georgy Todorov. Polarization-dependent sensitivity of level-crossing, coherent-population-trapping resonances to stray magnetic fields. *JOSA B*, 23(9):1729–1736, 2006.
- [120] Zeeshan Ali Safdar Jadoon, Heung-Ryoul Noh, and Jin-Tae Kim. Effects of neighboring transitions on the mechanisms of electromagnetically induced absorption and transparency in an open degenerate multilevel system. *Scientific Reports*, 12(1):1–9, 2022.
- [121] Y Nafcha, M Rosenbluh, P Tremblay, and C Jacques. Coherence-induced population redistribution in optical pumping. *Physical Review A*, 52(4):3216, 1995.
- [122] Daniel A Steck. Rubidium 87 d line data, 2001.
- [123] T Lauprêtre, J Ruggiero, R Ghosh, F Bretenaker, and F Goldfarb. Observation of electromagnetically induced transparency and slow light in the dark state-bright state basis. *Optics Express*, 17(22):19444–19450, 2009.
- [124] Jin Wang. Decoherence effects in an electromagnetically induced transparency and slow light experiment. *Physical Review A*, 81(3):033841, 2010.

- [125] Ranjit Kumar Singh, Nayan Sharma, Indra Hang Subba, Souvik Chatterjee, and Ajay Tripathi. Competition between off-resonant and on-resonant processes in electromagnetically induced transparency in presence of magnetic field. *Physics Letters A*, 416:127673, 2021.
- [126] M Auzinsh, A Berzins, R Ferber, F Gahbauer, L Kalvans, A Mozers, and A Spiss. Dependence of the shapes of nonzero-field level-crossing signals in rubidium atoms on the laser frequency and power density. *Physical Review A*, 87(3):033412, 2013.
- [127] CY Ye, AS Zibrov, YV Rostovtsev, and MO Scully. Electromagnetically induced absorption in quasi-degenerate two-level doppler broadened atomic system. *Journal of Modern Optics*, 50(15-17):2605–2613, 2003.
- [128] AV Taichenachev, AM Tumaikin, and VI Yudin. Electromagnetically induced absorption in a four-state system. *Physical Review A*, 61(1):011802, 1999.
- [129] SG Rautian. Spontaneous optical-coherence transfer and the nonlinear spectroscopy of gases. *Journal of Experimental and Theoretical Physics*, 88(1):6–15, 1999.
- [130] Soo Kyoung Kim, Han Seb Moon, Kyoungdae Kim, and Jung Bog Kim. Observation of electromagnetically induced absorption in open systems regardless of angular momentum. *Physical Review A*, 68(6):063813, 2003.
- [131] Chana Goren, Arlene D Wilson-Gordon, Michael Rosenbluh, and H Friedmann. Electromagnetically induced absorption due to transfer of coherence and to transfer of population. *Physical Review A*, 67(3):033807, 2003.
- [132] C Goren, AD Wilson-Gordon, M Rosenbluh, and H Friedmann. Atomic four-level systems. *Physical Review A*, 69(5):053818, 2004.
- [133] T Zigdon, AD Wilson-Gordon, and H Friedmann. Pump-probe spectroscopy in degenerate two-level atoms with arbitrarily strong fields. *Physical Review A*, 77(3):033836, 2008.
- [134] Luca Spani Molella, Rolf-Hermann Rinkleff, and Karsten Danzmann. Role of the coupling laser in electromagnetically induced absorption. *Physical Review A*, 72(4):041802, 2005.

- [135] CY Ye, AS Zibrov, YV Rostovtsev, and MO Scully. Electromagnetically induced absorption in quasi-degenerate two-level doppler broadened atomic system. *Journal of Modern Optics*, 50(15-17):2605–2613, 2003.
- [136] Xihua Yang, Jiteng Sheng, and Min Xiao. Electromagnetically induced absorption via incoherent collisions. *Physical Review A*, 84(4):043837, 2011.
- [137] Chana Goren, Arlene D Wilson-Gordon, Michael Rosenbluh, and H Friedmann. Electromagnetically induced absorption due to transfer of coherence and to transfer of population. *Physical Review A*, 67(3):033807, 2003.
- [138] MG Bason, AK Mohapatra, KJ Weatherill, and CS Adams. Narrow absorptive resonances in a four-level atomic system. *Journal of Physics B: Atomic, Molecular and Optical Physics*, 42(7):075503, 2009.
- [139] Khairul Islam, Dipankar Bhattacharyya, Arindam Ghosh, Debasish Biswas, and Amitava Bandyopadhyay. Study on probe field propagation in the presence of control and coupling fields through a four-level n-type atomic system. *Journal of Physics B: Atomic, Molecular and Optical Physics*, 50(21):215401, 2017.
- [140] Shigeru Nakayama. Theoretical analysis of rb and cs d2 lines in saturation spectroscopy with optical pumping. *Japanese Journal of Applied Physics*, 23(7R):879, 1984.
- [141] B Gross, N Papageorgiou, V Sautenkov, and A Weis. Velocity selective optical pumping and dark resonances in selective reflection spectroscopy. *Physical Review A*, 55(4):2973, 1997.
- [142] T Zigdon, AD Wilson-Gordon, and H Friedmann. Pump-probe spectroscopy in degenerate two-level atoms with arbitrarily strong fields. *Physical Review A*, 77(3):033836, 2008.
- [143] S Dey, N Aich, S Mitra, C Chaudhuri, PN Ghosh, and B Ray. A study of the repumping laser and external magnetic field effect on coherent absorption resonance in alkali vapour. *Chemical Physics Letters*, 627:107–115, 2015.